

The evolution of temperature and density structures of OB cluster-forming molecular clumps

Y. Lin^{1*}, F. Wyrowski¹, H. B. Liu², A. Izquierdo³, T. Csengeri⁴, S. Leurini⁵, and K. M. Menten¹

¹ Max Planck Institute for Radio Astronomy, Auf dem Hügel 69, 53121 Bonn
e-mail: ylin@mpi-fr-bonn.mpg.de

² Institute of Astronomy and Astrophysics, Academia Sinica, 11F of Astronomy-Mathematics Building, AS/NTU No.1, Sec. 4, Roosevelt Rd, Taipei 10617, Taiwan, ROC

³ European Southern Observatory, Karl-Schwarzschild-Str. 2, 85748 Garching bei München, Germany

⁴ OASU/LAB-UMR5804, CNRS, Université Bordeaux, allée Geoffroy Saint-Hilaire, 33615 Pessac, France

⁵ INAF – Osservatorio Astronomico di Cagliari, Via della Scienza 5, I-09047 Selargius (CA), Italy

December 3, 2021

ABSTRACT

Context. OB star clusters originate from parsec-scale massive molecular clumps, while individual stars may form out of $\lesssim 0.1$ pc scales dense cores. The thermal properties of the clump gas are key factors governing the fragmentation process, and are closely affected by gas dynamics and feedback of forming stars.

Aims. We aim to understand the evolution of temperature and density structures on the intermediate-scale ($\lesssim 0.1$ -1 pc) extended gas of massive clumps. This gas mass reservoir is critical for the formation of OB clusters due to their extended inflow activities and intense thermal feedback during and after the formation.

Methods. We performed ~ 0.1 pc resolution observations of multiple molecular line tracers (e.g., CH₃CCH, H₂CS, CH₃CN, CH₃OH) which cover a wide range of excitation conditions, towards a sample of eight massive clumps. The sample covers different stages of evolutions, and includes infrared-weak clumps and sources that are already hosting an HII region, spanning a wide luminosity-to-mass ratio (L/M) range from ~ 1 to ~ 100 (L_{\odot}/M_{\odot}). Based on various radiative transfer models, we constrain the gas temperature and density structures and establish an evolutionary picture, aided by a spatially-dependent virial analysis and abundance ratios of multiple species.

Results. We determine temperature profiles varying between 30-200 K over a continuous scale, from the center of the clumps out to 0.3-0.4 pc radii. The clumps' radial gas density profiles, described by radial power-laws with slopes between -0.6 and ~ -1.5 , are steeper for more evolved sources, as suggested by results based on both dust continuum, representing the bulk of the gas ($\sim 10^4$ cm⁻³), and CH₃OH lines probing the dense gas ($\gtrsim 10^6$ - 10^8 cm⁻³) regime. The density contrast between the dense gas and the bulk gas increases with evolution, and may be indicative of spatially and temporally varying star formation efficiencies. The radial profiles of the virial parameter show a global variation towards a sub-virial state as the clump evolves. The line-widths probed by multiple tracers decline with increasing radius around the central core region and increase in the outer envelope, with a slope shallower than the case of the supersonic turbulence ($\sigma_v \propto r^{0.5}$) and the subsonic Kolmogorov scaling ($\sigma_v \propto r^{0.33}$). In the context of evolutionary indicators for massive clumps, we also find that the abundance ratios of [CCH]/[CH₃OH] and [CH₃CN]/[CH₃OH] show correlations with clump L/M .

Key words. ISM: clouds – ISM: individual objects (G18.606-00.074, G19.882-00.534, G08.684-00.367, G31.412+00.307, G08.671-00.356, G13.658-00.599, G28.397+00.080, G10.624-00.380) – ISM: structure – surveys – stars: formation

1. Introduction

Massive star-forming clumps are progenitors of OB clusters (Williams et al. 2000, Motte et al. 2018). They have masses of typically $\gtrsim 1000 M_{\odot}$ over a spatial scale of ~ 1 pc. Fragmentation and accretion processes of OB star clusters are strongly influenced by the evolution of the kinematics, density and temperature structure of pc-scale gas clumps (Girichidis et al. 2011, Lee & Hennebelle 2019, Padoan et al. 2020), and vice versa (Krumholz et al. 2012, Offner et al. 2009, Hennebelle et al. 2020). Particularly, the stellar initial mass function (IMF) appears to be universal that varies weakly from one environment to another in the Milky Way, indicating that the formation of

the most massive stars is deterministic, favoring particular physical environments instead of randomly occurring in molecular clouds (Kroupa et al. 2013). This, together with dominant feedback caused by massive stars, may determine the evolutionary track of massive clumps. Accordingly, observational evidence can be collected by sampling a wide range of clumps at different evolutionary stages.

The process of gas collapse resulting in protostars has been studied for decades, among the first are the works by Larson (1969), Penston (1969) and Shu (1977). These are commonly referred to as ‘outside-in’ and ‘inside-out’ models, indicating the succession of the spherical collapse of isothermal clouds, which describe the gas flows (immediately) prior to and after development of a protostar (singularity), respectively. The density profiles of Larson (1969) and Penston (1969) exhibits a r^{-2} relation while the density profile of the inner free-falling and outer

* Member of the International Max-Planck Research School (IMPRS) for Astronomy and Astrophysics at the Universities of Bonn and Cologne.

static envelopes of Shu (1977) model follow $r^{-1.5}$ and r^{-2} , separately. On the other hand, when turbulent pressure is taken into account to explain the observed linewidth-size scaling relation, the logatropic (nonisothermal) gas follows, a flatter profile proportional to r^{-1} (e.g. McLaughlin & Pudritz 1997) in the outer region. Recently, the process of spherically symmetric cloud collapse has been revisited extensively: Coughlin (2017) present solutions for arbitrary initial density profiles, extending to non-self-similar regime; work by Murray & Chang (2015), Murray et al. (2017) considers turbulent energy generated from gravitational collapse and a highly dynamic system (as compared to hydrostatic equilibrium assumed by Shu (1977)). Furthermore, due to significant heating sources and high opacities associated with massive star-forming clouds, the assumption of isothermality might break down and a polytropic equation of state (EOS) needs to be introduced which quantifies the balance of gas cooling and heating and can incorporate turbulent pressure (Curry & McKee 2000). The polytropic index γ (with $T \propto \rho^{\gamma-1}$) has been shown to have a decisive effect on the dynamical evolution of molecular clouds (Passot & Vázquez-Semadeni 1998, Spaans & Silk 2000) and eventually on the IMF (e.g. Klessen et al. 2007, Jappsen et al. 2005). Moreover, recent works have demonstrated that a simple EOS assumption for the gas evolution might fail to explain the invariability of the peak of the IMF, while (proto)stellar radiative heating, a process that is not fully captured by the EOS, seems to play a crucial role in setting the characteristic mass scale (e.g. Bate 2009, Krumholz et al. 2011, Guszejnov et al. 2016, 2017). Given these theoretical developments, it is timely to measure with observations the detailed gas temperature and density distribution inside massive clumps.

Understanding how the mass of massive clumps is distributed over different density regimes is fundamental to understanding the evolution of the star formation rate (SFR) and star formation efficiency (SFE) on larger physical scales (e.g. Lee et al. 2015, Parmentier 2019). On cloud scales ($\gtrsim 10$ pc), the gas column density distribution follows a log-normal probability function (N-PDF) in a turbulent medium while it develops a power-law tail(s) as significant gravitational collapse commences in high density regimes (e.g. Klessen 2000, Kritsuk et al. 2011). The relevant scales are readily resolved in nearby star-forming clouds and OB cluster forming regions (e.g. Kainulainen et al. 2009, Lin et al. 2016, 2017). The power-law shape is suggested to originate from power-law density profiles (Federrath & Klessen 2013a, Myers 2015). Hence, measurements of clump density profiles can provide insights on how the dense gas of molecular clouds lead to the power-law excess of N-PDFs.

Most previous works on the density structure of massive clumps are based on single dish observations, of both continuum and molecular lines. Works discussing samples of sources include but are not limited to, e.g. van der Tak et al. (2000), Mueller et al. (2002), Beuther et al. (2002a), Hatchell & van der Tak 2003, Rolfs et al. (2011), Williams et al. (2005), Palau et al. (2014). With the advent of wide-band receivers, especially those equipping interferometers, spatially resolved multi-line observations have become efficient (e.g. Beuther et al. 2007, Li et al. 2019, Gieser et al. 2021), which are indispensable to measure the broad density and temperature ranges associated with massive star formation.

We have conducted a pilot survey of eight massive clumps with the Submillimeter Array (SMA) and the APEX telescope. For the target clump selection, we followed the criterion elaborated in Sect. 2.1. Main molecular lines of interest are listed in Table 3, which include multiple efficient thermometers and densitometers for massive clumps, as suggested by single dish

observations towards a statistically large sample (Giannetti et al. 2017, Leurini et al. 2004, 2007). We use various modeling methods to quantify the clump density and temperature structure using these lines. Throughout the paper, we follow the existing nomenclature in the literature (e.g., Williams et al. 2000, Zhang et al. 2009; Liu et al. 2012, Motte et al. 2018). In this way, massive molecular clumps refer to structures with sizes of ~ 0.5 -1 pc, massive molecular cores refer to the < 0.1 pc size structures embedded within a clump, and condensations refer to the distinct molecular substructures within a core. In Figure 1 we provide a schematic picture of different scales of a molecular cloud. The physical characteristics across the scales, as elaborated in the above, are marked for individual structures. We are interested in understanding the physical structure of massive clumps, which have a vast range of gas densities, and are the building blocks of the star-forming clouds; particularly they compose the high-density tail of the cloud N-PDF.

The paper is organised as follows: in Sect. 2 we describe the observations and data reduction. In Sect. 3, we describe the radiative transfer modeling procedure and elaborate on the analysis of both line and continuum observations, to derive the temperature, density, linewidth and virial parameter profiles, and abundances of multiple species. Sect. 3.1 gives a general outline of the radiative modeling methods and procedures we adopted. Sect. 3.3 provides an overview of the distribution of the molecular lines used as thermometers and densitometers in this paper. Sect. 3.4, Sect. 3.5, in addition to Appendix E, F focus on the radiative transfer modeling procedures and results of continuum and molecular lines. In Section 3.2 the properties of the sources extracted from SMA 1.2 mm continuum are presented. Analysis of some complementary lines is presented in Appendix D. In Section 4 we discuss the outcome of the modeling results, with a comparison between target sources and the physical implications. Finally in Section 5 we concluded on our findings.

2. Observations and data reduction

2.1. Source selection

The target sources are selected from APEX telescope Large Survey of the Galaxy (ATLASGAL) survey (Schuller et al. 2009) and are located at a distance of 4-6 kpc (Urquhart et al. 2018). They cover different evolutionary stages, suggested by different luminosity-to-mass ratios (Figure 2) and different signposts of star-formation activity (see further detail in Appendix A). For comparison, in Figure 2 we present the distribution of luminosity and mass for ATLASGAL sources that (1) are located at a distance within 4-8 kpc with a radius of < 2 pc (Urquhart et al. 2018), and (2) have masses and peak fluxes higher than $300 M_{\odot}$ and peak flux ~ 2 Jy/beam, respectively. The background contours illustrate the distribution of ATLASGAL sources in distance range of 4-8 kpc, with masses over $300 M_{\odot}$ and peak flux $\gtrsim 2$ Jy/beam with a radius of less than 2 pc.

In Fig. 2, we also include several evolutionary tracks: Gray dashed-dotted lines are the empirical evolutionary tracks for massive clumps with envelope masses of 80, 140, 350, 700, and $2000 M_{\odot}$ which will form a single protostar with varying accretion rates based on turbulent core model (McKee & Tan 2003), as derived in Molinari et al. (2008). green lines indicate tracks of massive clumps having constant accretion rates of $10^{-5} M_{\odot} \text{yr}^{-1}$ (dotted), $10^{-4} M_{\odot} \text{yr}^{-1}$ (dashed) and $10^{-3} M_{\odot} \text{yr}^{-1}$ (solid), for the most massive star in the cluster. The other stellar members follow an equal accretion stopping probability, with an accretion rate $\propto M^{1.5}$. The orange pluses mark the time epoch of 2×10^4

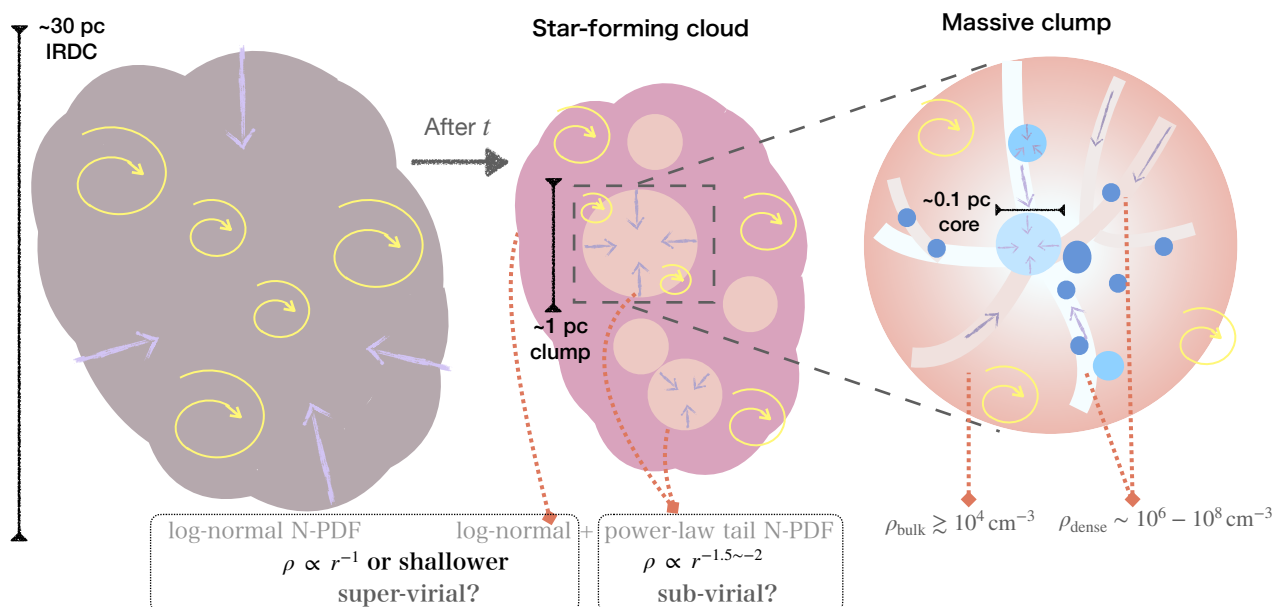


Fig. 1. Schematic picture of molecular cloud structure over spatial scales of >10 pc to ~ 0.1 pc: from cloud to core scale. A molecular cloud starts contraction from an initial stage that appears to be an infrared dark cloud (IRDC) and evolves into a star-forming one, embedding a number of molecular clumps. The massive clumps, of ~ 1 pc in size, are generally composed of filamentary structures and cores at different evolutionary stages. In all figures, yellow curved arrows represent turbulent motions and purple arrows indicate gravitational contraction or gas inflows (along filaments). In the rightmost figure, thick lines show filaments and blue ovals indicate cores of different masses; the color gradient of the clump indicate a density gradient of the bulk gas. The characteristics of different structures are linked to texts by dotted arrows.

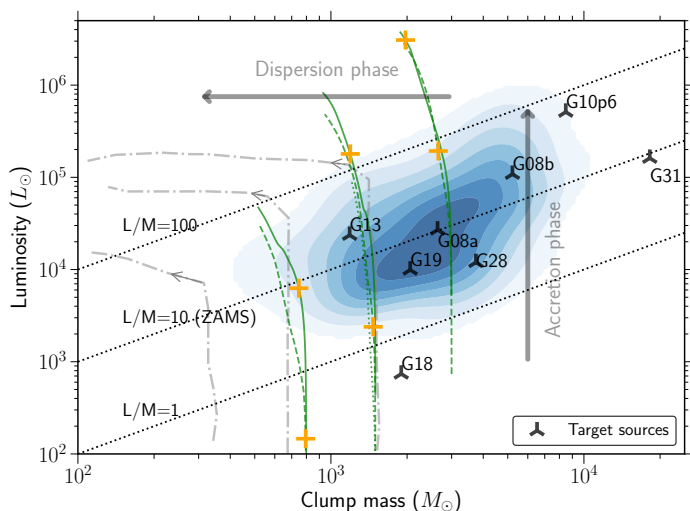


Fig. 2. The luminosity-mass diagram of target sources (three-branched triangle markers). The evolutionary tracks of massive clumps of different envelope masses and will from a cluster of stars with different accretion rates are shown in green lines (dotted and solid); gray lines (dash-dotted) with arrows are showing the evolutionary track of clumps of different envelope masses, but are assumed to form a single massive star (Molinari et al. 2008, for more details see Sect. 2.1.)

yr for each accretion track. The SFE is assumed to be 30% and the underlying stellar population follows canonical IMF (Kroupa et al. 1993). Accretion luminosities are estimated by interpolating massive protostar models in Hosokawa & Omukai (2009).

The lower mass limit of $300 M_{\odot}$ corresponds to the mass of a massive clump in which at least one $> 8 M_{\odot}$ star will form according to the normal IMF with an assumed star formation efficiency (SFE) of 30% (Kroupa et al. 1993, Sanhueza et al. 2017). The peak flux density of 2 Jy/beam with beam full-width

at half-maximum (FWHM) $\sim 20''$ at $870 \mu\text{m}$ from ATLASGAL survey, considering a distance of 6 kpc, implies a mass of $>100 M_{\odot}$ concentrated in the clump central ~ 0.5 pc region, assuming a dust temperature of 50 K and dust opacity of $1.8 \text{ cm}^2 \text{ g}^{-1}$ with a gas-to-dust ratio of 100. Thus, this selection criterion therefore yields a sample of eight massive clumps (Table 1) with moderate to high central concentration. We note that our target sample is representative of relatively more evolved sources with respect to those that fulfill the aforementioned criteria. These sources can be easily detected with 1 mm lines given their favorable excitation conditions, and we further complement the sample with an infrared dark source G18.

2.2. SMA observations

We performed SMA observations in the ~ 1 mm band towards seven clumps in the subcompact array configuration on 2017 June 11, and in the compact array configuration on 2017 August 28 (Project 2017A-S030, PI: Yuxin Lin), which covered baseline lengths of 9.5-45 meters and 16-77 meters, respectively. The selected target sources are summarized in Table 1. Detailed information about each target source from previous studies is summarized in Appendix A. We used the dual receivers mode supported with the SMA Wideband Astronomical ROACH2 Machine (SWARM) backend: The RxA receivers covered the frequency ranges of 188.4-196.7 GHz and 204.4-212.7 GHz in the lower and upper sidebands, respectively; the RxB receivers covered the frequency ranges of 238.5-246.8 GHz and 254.5-262.8 GHz, respectively. The intrinsic spectral channel width was 140 kHz. The molecular line transitions we covered are summarized in Table 3.

In addition, we retrieved archival SMA data towards the luminous ultra compact (UC) HII region G10.624-0.38, which remains deeply embedded in a $M_{\text{gas}} = 10^3$ - $10^4 M_{\odot}$ molecular clump and harbors a cluster of OB stars. These observations cov-

ered the CH₃OH $J=5-4$ and $J=7-6$ and the CH₃CN $J=19-18$ line multiplets. We refer to Baobab Liu et al. (2010), Liu et al. (2011), and Liu et al. (2012) for details of these observations.

We followed the standard SMA data calibration strategy. The application of system temperature (T_{sys}) information and the absolute flux, passband, and gain calibrations were carried out using the MIR IDL software package (Qi 2003). The absolute flux scalings were derived by comparing the visibility amplitudes of the gain calibrators with those of the absolute flux standard sources of the SMA, which were Callisto and Neptune for the subcompact and compact array observations, respectively. After calibration, we performed zeroth-order fitting of continuum levels from line-free channels and the joint weighted imaging adopting robust weighting of all continuum data were performed using the MIRIAD software package (Sault et al. 1995). The resultant synthesised beam is typically 4.''5 at 241 GHz. The sensitivity (3σ) of continuum observation is ~ 0.04 Jy beam⁻¹ and of lines ~ 0.5 K. For clump G18, we do not obtain robust detection of the thermometer lines of CH₃CCH, H₂CS and CH₃CN (Table 3) with this achieved line sensitivity. We used the previously published result from IRAM 30m telescope observations of 3 mm CH₃CCH and CH₃CN lines (Giannetti et al. 2017) instead.

2.3. APEX observations

Single-dish observations at 1 mm towards our target sources were performed with the MPIfR principal investigator (PI) instrument PI230 on the the Atacama Pathfinder Experiment 12-meter submillimeter telescope (APEX, Güsten et al. 2006), between March to September 2017 and July 2018 (Project M-099.F-9513A-2017, PI: Yuxin Lin). The PI230 receiver is a dual polarisation sideband separating heterodyne system with a total of 32 GHz bandwidth working at 230 GHz, and can cover the spectral range of 200-270 GHz. We conducted observations with two spectral setups, covering frequency ranges of 202.2-210.0 GHz, 218.0-225.8 GHz and 239.2-247.0 GHz, 255.0-262.8 GHz, respectively. For each target source a region of 3'×3' centered at the source position was mapped in the On-The-Fly (OTF) mode with both setups.

During the observations, the typical precipitable water vapor (PWV) was ~ 1.5 to 2.5 mm. The pointing was determined by continuum observations on Saturn when available, or CO $J=2-1$ observations on bright nearby evolved stars (e.g. RAFGL2135, R-Dor). The pointing accuracy was found to be within 3''. Focus was checked on Saturn every 2-4 hours. The main beam efficiency (η_{mb}) for the PI230 instrument varies over the observing period, with a range of $\sim 63\% - 72\%$ ¹. The calibration uncertainty is typically within 20%, estimated based on the flux measurement of the pointing sources.

Basic data reductions were done with the GILDAS software package², including flagging of bad spectra, baseline subtraction, unit conversion (T_{A}^* to T_{mb}), and building spectral cubes. Final spectral cubes are re-sampled to 0.5 km/s spectral resolution for all lines.

2.4. SMA-APEX combination and imaging

For our primary target lines covered by both SMA and APEX, which have extended emission, namely CH₃CCH $J=12-11$, CH₃OH $J=5-4$, C₂H $J=3-2$, H¹³CO⁺ $J=3-2$, CS $J=5-4$, C³⁴S $J=5-4$ and SO $J=4_5-3_4$, we combined the two dataset in the

Fourier domain (uv -domain) with MIRIAD. This combination is essentially imaging together the pseudo-visibilitys generated from single-dish observations and interferometer measurements, so that the short-spacing information including zero baseline which is obtained with single dish can be complemented to interferometry data; the method is commonly referred to as joint deconvolution or joint reconstruction method (Kurono et al. 2009, Koda et al. 2011).

In the combination procedure, we first deconvolved the APEX data from the single-dish Gaussian beam (FWHM $\sim 30''$) and then multiplied the resultant image with the primary beam of the SMA observations. The obtained image is then used to generate a single-dish uv model, i.e. the pseudo-visibilitys, by randomly sampling a visibility distribution to match that of the single-dish beam pattern. The zero spacing visibility is additionally sampled and added to the produced pseudo-visibilitys. Finally, the pseudo- and interferometric visibilitys are imaged together to produce the combined image. In the final imaging step, we apply a Gaussian tapering function of FWHM $\sim 2''$ to increase the detectability of extended emission. In the end we adopt a final step to linearly combine the product of this standard joint deconvolution method with the single-dish image in the Fourier domain, using `immerge` in the MIRIAD package. This step is necessary and found to be preserving the single-dish overall fluxes better than using solely the joint deconvolution method, due to the fact that the deconvolution method is not flux conserving; a similar procedure has been adopted in e.g. Monsch et al. (2018). The combined images have comparable total fluxes to the APEX data, within a difference of 15%.

For details on the proper weighting scheme in the joint deconvolution method and the impact of sensitivities of single-dish and interferometry data, we refer to Kurono et al. (2009).

2.5. Ancillary data: mid-/far-infrared and submm-continuum data from multiple single-dish telescopes

We used the single-dish mid- and far-infrared, and submm continuum data to constrain the bulk gas structures and construct the SEDs (Figure 4).

Besides the 870 μm data from ATLASGAL survey (Schuller et al. 2009, Csengeri et al. 2016) obtained by APEX-LABOCA (Siringo et al. 2009), we also adopted 350 μm data obtained by CSO-SHARC2 or APEX-SABOCA instrument. The information of the observations and data reduction procedure are detailed in Lin et al. (2017) and Lin et al. (2019).

For sources without available 350 μm from ground-based telescope (of 10'' angular resolution), we used the available observations from James Clerk Maxwell Telescope (JCMT)³ Submillimetre Common-User Bolometer Array 2 (SCUBA2)

³ The James Clerk Maxwell Telescope is operated by the East Asian Observatory on behalf of The National Astronomical Observatory of Japan, Academia Sinica Institute of Astronomy and Astrophysics, the Korea Astronomy and Space Science Institute, the National Astronomical Observatories of China and the Chinese Academy of Sciences (Grant No. XDB09000000), with additional funding support from the Science and Technology Facilities Council of the United Kingdom and participating universities in the United Kingdom and Canada. The James Clerk Maxwell Telescope has historically been operated by the Joint Astronomy Centre on behalf of the Science and Technology Facilities Council of the United Kingdom, the National Research Council of Canada and the Netherlands Organization for Scientific Research. Additional funds for the construction of SCUBA-2 were provided by the Canada Foundation for Innovation.

¹ <http://www.apex-telescope.org/telescope/efficiency/>

² <http://www.iram.fr/IRAMFR/GILDAS>

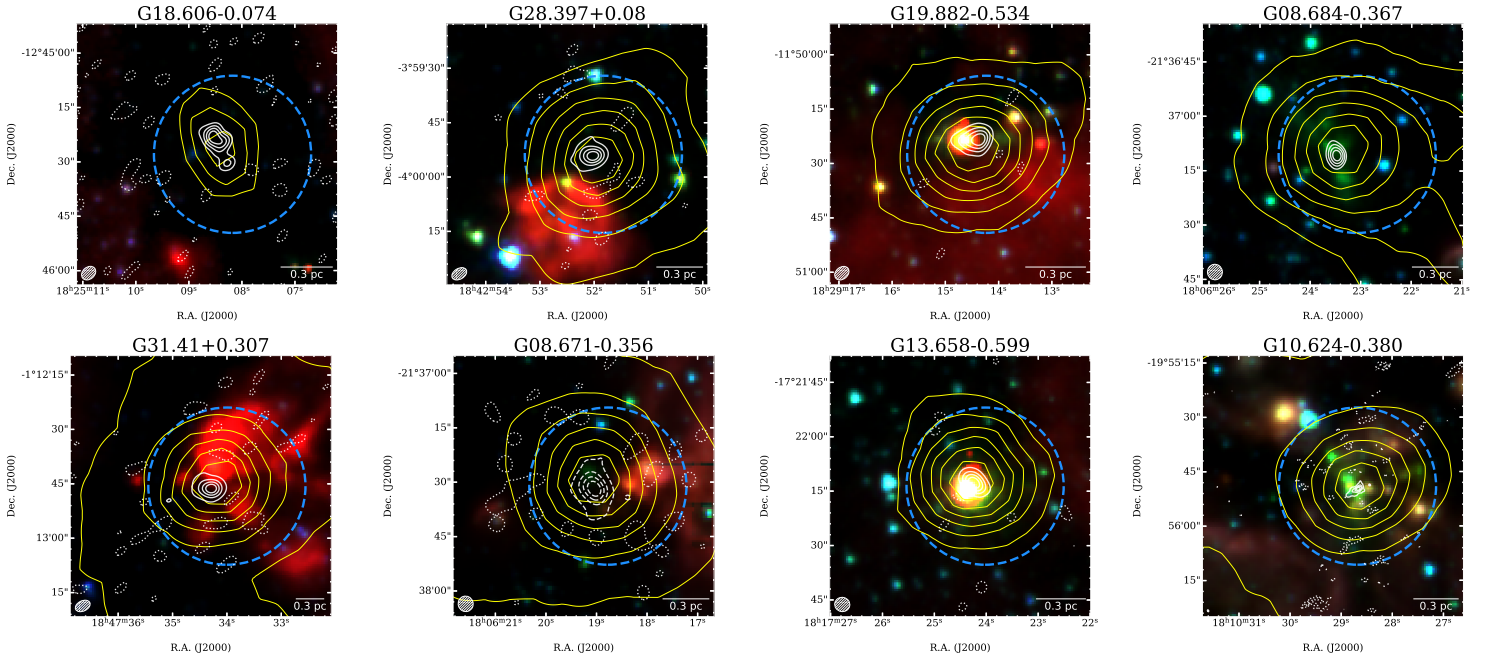


Fig. 3. *Spitzer* IRAC RGBs (R: 8.0 μm ; G: 4.5 μm B: 3.6 μm) maps of the target sources. Yellow contours show the ATLASGAL 870 μm emission from 1 Jy/beam to the peak flux for each source, using 7 levels with uniform spacing. White contours show SMA 1.2 mm emission from 3σ to the peak flux using 5 levels with uniform spacings. Negative flux levels of the 1.2 mm continuum are shown in contours of dotted lines, from -1σ to the minimum negative flux with 2 levels. The beam of the SMA continuum is shown in the lower left corner of each plot. The beam size of the archival data for source G10 is much smaller than other sources (Section 2.2). The primary beam size is shown in each plot as blue dashed circle.

Table 1. Target sources.

Source ^a	R.A. (J2000)	Decl. (J2000)	Distance ^b (kpc)	Gas mass ^c ($10^2 M_{\odot}$)	Luminosity ^c ($10^3 L_{\odot}$)	L/M (L_{\odot}/M_{\odot})	Category
G18.606–00.074 (G18)	18 ^h 25 ^m 08 ^s .27	–12°45′22 ^s .7	3.7	19	0.75	0.4	IR weak
G28.397+00.080 (G28)	18 ^h 42 ^m 52 ^s .08	–03°59′53 ^s .7	4.8	37	12	3.2	IR bright
G19.882–00.534 (G19)	18 ^h 29 ^m 14 ^s .19	–11°50′28 ^s .4	3.7	20	99	4.8	IR bright
G08.684–00.367 (G08a)	18 ^h 06 ^m 23 ^s .35	–21°37′05 ^s .2	4.8	27	27	10.2	IR weak
G31.412+00.307 (G31)	18 ^h 47 ^m 34 ^s .32	–01°12′45 ^s .5	7.9	182	161	9.0	HII
G08.671–00.356 (G08b)	18 ^h 06 ^m 19 ^s .23	–21°37′26 ^s .8	4.8	52	11	20.7	HII
G13.658–00.599 (G13)	18 ^h 17 ^m 23 ^s .46	–17°22′09 ^s .2	4.5	12	24	19.9	IR bright
G10.624–00.380 (G10)	18 ^h 10 ^m 28 ^s .638	–19°55′49 ^s .1	4.95	84	511	60	HII

a: The abbreviated source names are given in brackets.

b: The references for the source distances are: Green & McClure-Griffiths (2011) for G08a, G08b and G19; Sanna et al. (2014) for G10; Wien et al. (2015) for G13; Churchwell et al. (1990) for G31; Carey et al. (2000) for G28; Sridharan et al. (2005) for G18.

c: The gas mass and luminosity of the clump is taken from Urquhart et al. (2018), but scaled to the adopted distance of the clump.

(Dempsey et al. 2013, Chapin et al. 2013) at 450 μm from the online data archive.

We also retrieved the archival Herschel⁴ images at 70/160 μm and 250/350/500 μm from the Herschel Infrared Galactic Plane (Hi-GAL) survey (Molinari et al. 2010) taken by the PACS (Poglitsch et al. 2010) and SPIRE instrument (Griffin et al. 2010). For the mid-infrared data, we used the 24 μm images from the MIPS Galactic Plane Survey (MIPSGAL, Carey et al. 2009) taken by *Spitzer* telescope.

⁴ Herschel is an ESA space observatory with science instruments provided by European-led Principal Investigator consortia and with important participation from NASA.

3. Results and analysis

3.1. Outline of the modeling and analysis procedure

In this work, we aim to provide a description of the gas density and temperature of massive clumps by performing radiative transfer calculations of molecular lines and multi-wavelength dust continuum. In this section we introduce the workflow of the modeling, starting by basic definitions of molecular line excitation. The modeling steps (shown in Figure 4) are explained in more detail in Section 3.4–3.6 as well as in Appendix E to F. The results of the radiative transfer models are discussed in Section 4.

Massive clumps have average molecular hydrogen densities of typically $\sim 10^4 \text{ cm}^{-3}$ (Csengeri et al. 2014, Urquhart et al. 2018); the collisional partner participating in the de- and excitation of molecular lines considered in this paper is primarily

Table 2. Source properties from 1.2 mm SMA continuum.

Source	$S_{1.2\text{mm}}^a$ (Jy)	R_{eff}^b (pc)	\bar{T}_d^c (K)	M_{core} (M_{\odot})	$M_{\text{core}}^{\text{Abel}}$ (M_{\odot})	$\bar{\rho}_{\text{core}}^d$ (10^4 cm^{-3})
G18 ^e	0.13	0.10	36	24.0	22.1	6.0
	0.02	0.04	19	5.5	-	-
G28	0.69	0.12	49	93.5	103.7	19.5
G19	1.07	0.10	37	124.1	65.3	23.6
G08a	0.35	0.10	50	49.1	18.6	8.0
G31	5.12	0.17	94	943.8	914.0	61.0
G08b	1.91	0.16	56	223.2	188.1	15.0
G13	0.51	0.11	48	59.0	58.5	15.2
G10	1.85	0.04	132	102.0	67.8	210.0

a: Total flux above 5σ . For source G08b, G31 and G10, subtraction of free-free emission is considered (details in Appendix B).

b: Effective radius is defined as $\pi R_{\text{eff}}^2 = \text{Area}$, where Area stands for the emission region above 5σ for each 1.2 mm map, i.e., non-deconvolved averaged size.

c: Dust temperature is assumed to be equal to gas temperature $T(r)$ obtained and refined in Sec 3.4, and the average temperature \bar{T}_d is calculated by averaging over pixels that have continuum emission above 5σ .

d: Average density calculated from $M_{\text{core}}^{\text{Abel}}$ and R_{eff} .

e: for clump G18, the calculation for two cores are given. In the Abel inversion calculation which assumes spherical symmetry, only the central, more massive core is considered. So $M_{\text{core}}^{\text{Abel}}$ and $\bar{\rho}_{\text{core}}$ are omitted for the secondary core.

hydrogen gas. The critical density (n_{crit}) (Table 4) defines the way in which a molecule in an excited state decays to ground state. When the main collisional partner is hydrogen, it stands for the critical hydrogen density at which timescales of radiative decay and collisional de-excitation are comparable, i.e. the net radiative decay rate from level J to a certain lower level equals the rate of collisional de-population out of the upper level J , for a multilevel system (e.g., Wilson et al. 2013).

With gas densities close to and well above n_{crit} , the thermalisation of energy levels is achieved, such that the excitation temperature (T_{ex}) can approximate the gas kinetic temperature (T_{kin}), with the population of energy levels reaching Boltzmann prediction (local thermodynamic equilibrium, LTE). On the other hand, if gas densities are below n_{crit} (sub-thermal excitation), then the population of the upper energy level is sensitive to varying gas densities. Observations of multiple transitions with different n_{crit} can probe a range of gas densities, by showing rather different ratios of line intensities. In particular, if the energy levels associated with these transitions are of similar energy, then the dependence of line ratios on temperature is minimised, and so it does the degeneracy of the mutual effect of gas temperature and density in determining level populations. We take advantage of these radiative properties to use selected molecular transitions as ‘densitometers’ of our target sources.

In a simple view, massive star-forming clumps may be considered as multi-layered gas structures showing centrally peaked gas density profiles. This is a natural outcome under self-gravity. From the outermost layer to the innermost region, transitions of higher and higher n_{crit} are thermalised progressively. Using a combination of thermometers of different n_{crit} , based on LTE assumption, can constrain gas temperatures over continuous spatial scales (with respect to the clump center). Analogous to a ‘densitometer’, a ‘thermometer’ is defined here as a set of molecular lines of a certain species whose level population is only (or dom-

inantly) sensitive to gas temperature, which arise from energy levels spanning a wide energy range and are connected ideally only through collisions, provided e.g. by K-ladder lines of symmetric top molecules.

Considering the gas density regime of massive star-forming clumps, and based on previous single-dish experiments (Gianetti et al. 2017) we have identified CH_3CCH , H_2CS and CH_3CN lines at 1 mm band (listed in Table 3) as ideal tracers for measuring temperature profiles of massive clumps. These tracers have n_{crit} of several 10^4 , 10^5 and 10^6 cm^{-3} , respectively (Table 4). On the other hand, the combination of distinct n_{crit} triggers a filtering effect, such that with each thermometer, the region it probes is limited to the gas density regimes ranging around and above its n_{crit} . Contamination by fore- and background gas layers of lower density to the observed emission is therefore negligible. This means that the line-of-sight (averaging) effect is reduced to gas component of a limited density range.

In addition, optical depths (τ) are low when typical abundances and excitation conditions are considered for these molecules, which implies that line ratios probe the gas kinetic temperature at the inner location of the gas layer. With these properties in mind, we derive the rotational temperature (T_{rot}) maps under the LTE assumption using multiple thermometers in Section 3.4. Temperature measurement of the outer regions are obtained using the extended CH_3CCH and H_2CS emission, and combined with temperatures derived from CH_3CN which is confined to the central region of the clumps. This combination allows us to establish the full radial temperature profile of the clumps. We also use multi-wavelength single-dish dust emission (SD continuum, as in Figure 4) to derive dust temperature maps by building spectral energy distributions (SEDs) assuming single-component modified black-body emission (Lin et al. 2016, 2019). The dust temperatures at the outer layer of clumps, are used to complete the temperature profile at larger radii for the

Table 3. Molecular lines of interest covered by the SMA observations. Information is taken from CDMS database (Müller et al. 2001).

Transitions	Rest frequency (GHz)	E_{up} (K)	Transitions	Rest frequency (GHz)	E_{up} (K)
(RxA lower sideband)			(RxB lower sideband)		
C ³⁴ S 5-4	241.016	27.8	CH ₃ OH $v_t=1$ 5 _{-1,5} -4 _{-1,4} E	241.203	326.2
CS 5-4	244.935	35.3	CH ₃ OH $v_t=1$ 5 _{2,4} -4 _{2,3} A	241.192	333.4
(RxA upper sideband)			CH ₃ OH $v_t=1$ 5 _{2,3} -4 _{2,2} A	241.196	333.4
CH ₃ CCH 12 ₀ -11 ₀	205.081	64.0	CH ₃ OH $v_t=1$ 5 _{0,5} -4 _{0,4} E	241.206	333.5
CH ₃ CCH 12 ₁ -11 ₁	205.076	71.1	CH ₃ OH $v_t=1$ 5 _{3,3} -4 _{3,2} E	241.180	357.4
CH ₃ CCH 12 ₂ -11 ₂	205.065	92.5	CH ₃ OH $v_t=1$ 5 _{-3,2} -4 _{-3,1} E	241.180	357.4
CH ₃ CCH 12 ₃ -11 ₃	205.045	128.2	CH ₃ CN 13 ₀ -12 ₀	239.138	80.3
CH ₃ CCH 12 ₄ -11 ₄	205.018	178.2	CH ₃ CN 13 ₁ -12 ₁	239.133	87.5
H ₂ CS 6 _{0,6} -5 _{0,5}	205.99	35.6	CH ₃ CN 13 ₂ -12 ₂	239.119	108.9
H ₂ CS 6 _{2,5} -5 _{2,4}	206.05	87.3	CH ₃ CN 13 ₃ -12 ₃	239.096	144.6
H ₂ CS 6 _{2,4} -5 _{2,3}	206.16	87.3	CH ₃ CN 13 ₄ -12 ₄	239.064	194.6
H ₂ CS 6 _{3,4} -5 _{3,3}	206.05	153.0	CH ₃ CN 13 ₅ -12 ₅	239.023	258.9
H ₂ CS 6 _{3,3} -5 _{3,2}	206.05	153.0	CH ₃ CCH 14 ₀ -13 ₀	239.252	82.1
H ₂ CS 6 _{4,3} -5 _{4,2}	206.00	244.9	CH ₃ CCH 14 ₁ -13 ₁	239.248	93.3
H ₂ CS 6 _{4,2} -5 _{4,1}	206.00	244.8	CH ₃ CCH 14 ₂ -13 ₂	239.234	114.7
SO 4 ₅ -3 ₄	206.176	38.6	CH ₃ CCH 14 ₃ -13 ₃	239.211	150.3
SO ₂ 3 _{2,2} -2 _{1,1}	208.700	15.3	CH ₃ CCH 14 ₄ -13 ₄	239.179	200.3
(RxB lower sideband)			H ₂ CS 7 _{0,7} -6 _{0,6}	240.267	46.1
CH ₃ OH 5 _{0,5} -4 _{0,4} A	241.791	34.8	H ₂ CS 7 _{2,6} -6 _{2,5}	240.382	98.8
CH ₃ OH 5 _{1,5} -4 _{1,4} E	241.767	40.4	H ₂ CS 7 _{3,5} -6 _{3,4}	240.392	164.6
CH ₃ OH 5 _{0,5} -4 _{0,4} E	241.700	47.9	H ₂ CS 7 _{3,4} -6 _{3,3}	240.393	164.6
CH ₃ OH 5 _{-1,4} -4 _{-1,3} E	241.879	55.9	H ₂ CS 7 _{4,4} -6 _{4,3}	240.332	256.5
CH ₃ OH 5 _{-2,4} -4 _{-2,3} E	241.905	57.1	H ₂ CS 7 _{4,3} -6 _{4,2}	240.332	256.5
CH ₃ OH 5 _{2,3} -4 _{2,3} E	241.904	60.7	SO ₂ 14 _{0,14} -13 _{1,13}	244.254	93.9
CH ₃ OH 5 _{2,4} -4 _{2,3} A	241.842	72.5	(RxB upper sideband)		
CH ₃ OH 5 _{2,3} -4 _{2,2} A	241.887	72.5	C ₂ H $N=3-2$, $J=7/2-5/2$, $F=3-2$	262.01	25.1
CH ₃ OH 5 _{-3,3} -4 _{-3,2} E	241.844	82.5	C ₂ H $N=3-2$, $J=7/2-5/2$, $F=4-3$	262.00	25.1
CH ₃ OH 5 _{3,3} -4 _{3,2} A	241.833	84.7	C ₂ H $N=3-2$, $J=5/2-3/2$, $F=3-2$	262.06	25.1
CH ₃ OH 5 _{3,2} -4 _{3,1} A	241.833	84.7	C ₂ H $N=3-2$, $J=5/2-3/2$, $F=2-2$	262.08	25.2
CH ₃ OH 5 _{3,3} -4 _{3,2} E	241.852	97.5	C ₂ H $N=3-2$, $J=5/2-3/2$, $F=2-1$	262.07	25.2
CH ₃ OH 5 _{3,3} -4 _{3,2} A	241.807	115.2	CH ₃ CCH 15 ₀ -14 ₀	256.337	98.4
CH ₃ OH 5 _{4,1} -4 _{4,0} A	241.807	115.2	CH ₃ CCH 15 ₁ -14 ₁	256.331	105.6
CH ₃ OH 5 _{4,2} -4 _{4,1} E	241.813	122.7	CH ₃ CCH 15 ₂ -14 ₂	256.317	127.0
CH ₃ OH 5 _{-4,1} -4 _{-4,0} E	241.830	130.8	CH ₃ CCH 15 ₃ -14 ₃	256.292	162.7
			CH ₃ CCH 15 ₄ -14 ₄	256.258	212.6
			H ¹³ CO ⁺ 3-2	260.255	25.0
			SO 6 ₆ -5 ₅	258.256	56.5
			SO 7 ₆ -6 ₅	261.843	47.6

clumps. With the simple one-component LTE modeling and one-component dust SED construction, we derive the projected radial profile of the obtained multiple temperature maps as the radial profiles, denoted as $T(r)$. With this approximation, a natural difference caused by line-of-sight (LOS) projection effects may appear as a function of radius due to density-weighted emission. However, as previously mentioned, due to the density-filtering effect by combination of multiple thermometers, the difference between the two profiles is largely minimised. Moreover, the projected radial temperature profile used as radial temperature profile is further benchmarked and refined by SED construction from full radiative transfer modeling of dust based on a density profile adopted for the clump (Sect. 3.6, Appendix E), and further shown to be able to produce the observed CH₃CCH lines and their spatial variation by full line radiative transfer models (Appendix F).

To probe the gas density, we rely on CH₃OH line series in the 1 mm band as a densitometer. We adopt one-component non-LTE models to derive the hydrogen volume density ($n(\text{H}_2)$) maps and benchmark the results using full non-LTE radiative transfer modeling (Sect. 3.6, Appendix F). The highest and lowest n_{crit} of the adopted line series are listed in Table 4. Moreover, with measured radial temperature profiles, the degeneracy of temperature and density can be further reduced by introducing $T_{\text{kin}}(T(r))$ in the non-LTE modeling, to constrain solely $n(\text{H}_2)$. We adopt this strategy in Section 3.5 (see also Appendix C). In Section 3.5 we use the one-component non-LTE model of CH₃OH lines to constrain $n(\text{H}_2)$. As mentioned before, the excitation of molecular lines has a selective effect on gas densities. Since we are also interested in the bulk gas density structure of massive clumps, we complement the density distribution measure with single-dish multi-wavelength dust emission. We conduct full radiative transfer modeling of dust to fit with these data (Appendix E), again

Table 4. Critical density for transitions of interest.

Transitions	Critical density ^a (cm ⁻³)
CS 5-4	1.1×10 ⁶
CH ₃ CCH 12 ₀ -11 ₀	2.7×10 ⁴ ^b
H ₂ CS 6 _{0,6} -5 _{0,5}	2.6×10 ⁵
CH ₃ OH 5 _{1,5} -4 _{1,4}	6.8×10 ⁵
CH ₃ OH 5 _{4,5} -4 _{4,4}	6.2×10 ⁷
CH ₃ CN 13 ₀ -12 ₀	3.5×10 ⁶
CH ₃ CCH 14 ₀ -13 ₀	4.3×10 ⁴ ^b
H ₂ CS 7 _{0,7} -6 _{0,6}	4.3×10 ⁵
C ₂ H N = 3-2, J=7/2-5/2, F=4-3	4.1×10 ⁵
SO 4 ₅ -3 ₄	2.4×10 ⁵
SO 6 ₆ -5 ₅	6.4×10 ⁵
SO 7 ₆ -6 ₅	1.0×10 ⁶
H ¹³ CO ⁺ 3-2	1.1×10 ⁶
SO ₂ 14 _{0,14} -13 _{1,13}	3.9×10 ⁵
SO ₂ 3 _{2,2} -2 _{1,1}	1.7×10 ⁵
CH ₃ CCH 15 ₀ -14 ₀	5.3×10 ⁴ ^b

a: Calculated following definition in Shirley (2015) in the optically thin limit ($\tau \sim 0.1$) at 50 K, considering a multi-level energy system whenever necessary.

b: Calculated using collisional coefficients of CH₃CN.

incorporating the $T(r)$ initially measured from thermometers. To benchmark the one-component non-LTE models, as well as to understand the difference of gas density results between modeling of dust emission and simple non-LTE modeling of CH₃OH, we utilise non-LTE full radiative transfer calculation of lines in Appendix F, for CH₃OH and CH₃CCH lines. This also helps to examine the possibility of spatial abundance variations of these lines as an additional factor in affecting the distribution of line emission. In this effort, particularly, the full non-LTE modeling of CH₃CCH provides a sanity check on the measured radial temperature profile $T(r)$ from rotational temperature maps. The workflow of the whole procedure is graphically summarized in Figure 4.

3.2. SMA 1.2 mm continuum

The SMA 1.2 mm dust continuum images resolved two compact sources (separated by $\sim 7.''2$, ~ 0.15 pc) in G18, and resolved isolated compact sources in the rest of the samples (Figure 3). Hereafter we refer to these compact sources as core structures. Before any further analyses, we utilised the archival centimeter band data to subtract free-free contamination in G08b, G31, and G10, assuming optically thin emission (i.e., $S_{\nu}^{\text{free-free}} \propto \nu^{-0.1}$; for details see Appendix B). Then the core radius is defined as the area above 5σ emission contours of the 1.2 mm images. The core effective radius, peak flux and integrated flux are listed in Table 2.

We assumed that dust emission in all cores is optically thin at 1.2 mm. Based on the OH5 opacity model (i.e., $\kappa_{1.2\text{mm}} = 0.81 \text{ cm}^2\text{g}^{-1}$; Ossenkopf & Henning 1994), we converted the continuum intensity detected at $>5\sigma$ to dust mass surface density, which was subsequently converted to gas mass surface density by assuming that the gas-to-dust mass ratio is 100. In these mass estimates, we assumed that dust temperature is identical to the gas temperature $T(r)$ which we derived (and refined, Equation 3) (c.f. Section 3.4, 3.6 and Appendix E).

There is a subtlety in the way we applied $T(r)$, which is related to the assumption of the thermal and density structures of the cores. We compared two ways of applying $T(r)$. In the first, we defined a mean core gas temperature T_{core}^- by making averages of $T(r)$ within the core size. For each pixel, we then adopted a dust temperature which is equal to $\min\{T(r = \ell), T_{\text{core}}^-\}$ when deriving $n(\text{H}_2)$ where ℓ is the projected distance from the pixel to the 1.2 mm continuum peak (i.e., centers of the sources). This means that we use the smaller value of the two temperatures of the average core temperature and the radial temperature at the each pixel position, to estimate the gas mass probed by dust emission. This is a reasonable assumption since dust emission is sampling all the gas component along LOS and the average mass temperature is likely dominated by the outer, colder gas component. Given that the projected radius ℓ is always smaller than the radius r , this approach still tends to overestimate the dust temperatures at small projected radii although it is alleviated. This in turn results in an underestimate of $n(\text{H}_2)$.

In a second approach, we assumed that the cores are spherically symmetric and optically thin. We used Abel transformation to convert the observed azimuthally averaged intensity profile of 1.2 mm emission to gas density $\rho(r)$ (for more details see Roy et al. 2014), as

$$\rho(r) = -\frac{1}{\pi\kappa_{\nu}B_{\nu}[T(r)]} \int_r^{r_{\text{eff}}} \frac{dI_{\nu}}{db} \frac{db}{\sqrt{b^2 - r^2}}, \quad (1)$$

where r_{eff} is the core effective radius. We then integrated $\rho(r)$ over the line-of-sight to obtain another version of $n(\text{H}_2)$ map. The two versions of $n(\text{H}_2)$ maps agree within a factor of 1.5-2. The average dust/gas temperatures within the core, two sets of mass estimates M_{core} and $M_{\text{core}}^{\text{Abel}}$, and average core density are summarized in Table 2.

3.3. The distribution of the emission from CH₃CCH, H₂CS, CH₃CN, CH₃OH lines and 1.2 mm continuum

Figure 3 shows the 1.2 mm dust continuum images taken with the SMA. We resolved two compact sources (separated by $\sim 7.''2$, ~ 0.15 pc) in G18, and resolved isolated compact sources in the rest of the samples. Figure 5 shows the integrated intensity maps of CH₃CCH, H₂CS, and CH₃CN which are overlaid on the integrated intensity maps of CH₃OH. In general, the CH₃OH lines and the lower K ladders of CH₃CCH were resolved on 0.3-0.4 pc scales while the CH₃CN lines and higher K ladders of H₂CS were resolved on 0.1-0.2 pc scales. The results of our quantitative analyses are presented in the following subsections.

3.4. Deriving pixel-based gas rotational temperature maps with LTE modelling for multiple thermometers

3.4.1. Thermometers

CH₃CCH and CH₃CN are symmetric top molecules. Their K ladder populations at a certain J level are determined primarily through collisions. Therefore, they have been regarded as thermometers for molecular clouds (Kuiper et al. 1984, Bergin et al. 1994). Given their similar geometry and molecular weight, CH₃CCH and CH₃CN are often assumed to have the same collisional coefficients, while CH₃CN has higher dipole moments than CH₃CCH. Due to this, a molecular clump can exhibit brighter CH₃CN line emission than CH₃CCH even in the case that the excitation of the CH₃CN molecules is limited to small pockets of dense gas, e.g. confined to the hot core region.

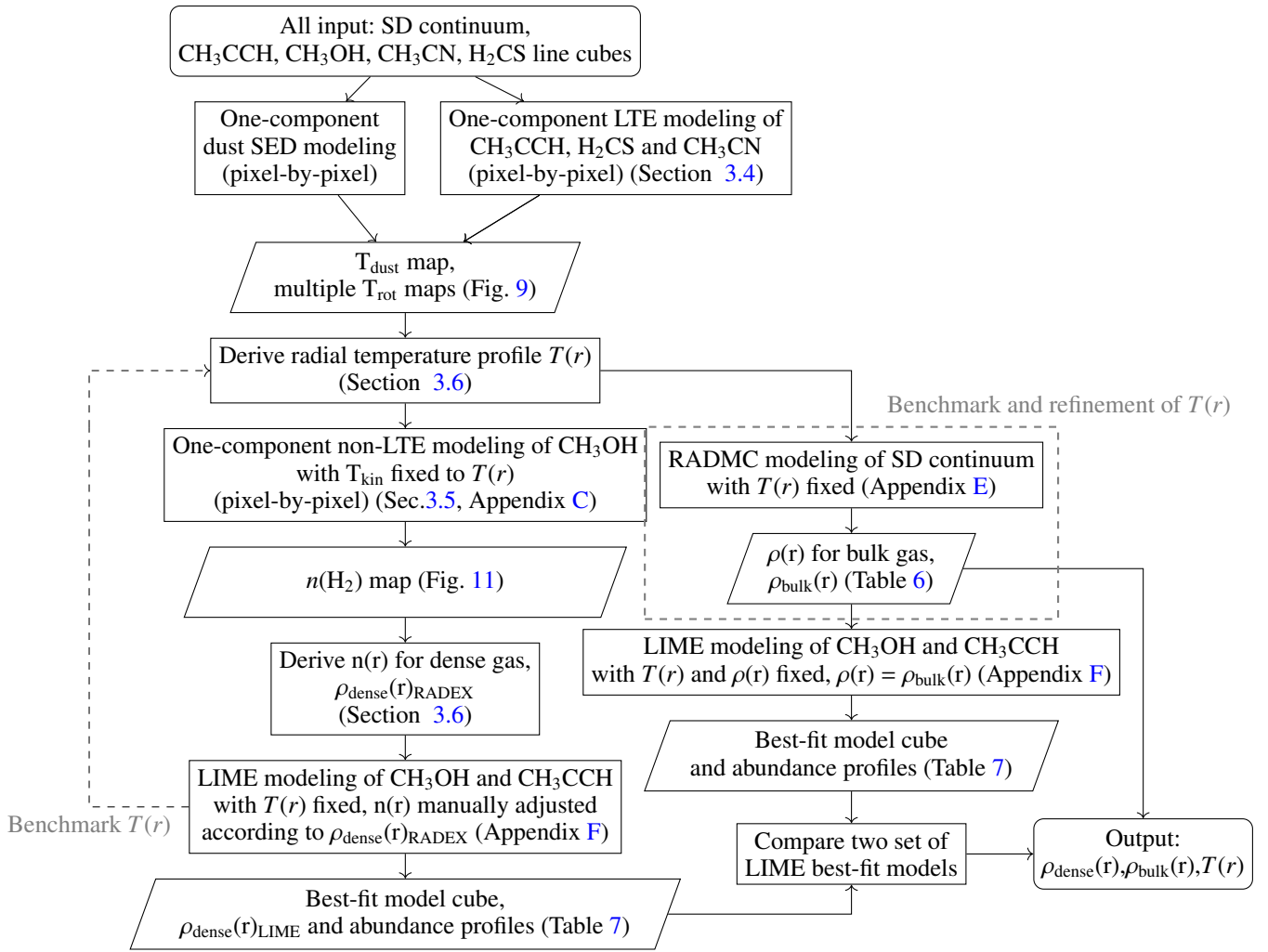


Fig. 4. Overall work flow showing the radiative transfer modeling procedure followed in this work.

The CH_3CN lines have been very commonly observed (Cummins et al. 1983, Sutton et al. 1986, Fayolle et al. 2015). They have been regarded as good tracers of hot molecular cores owing to the fact that they were mainly detected around significantly heated regions. On the other hand, CH_3CCH has been detected in spatially more extended, lower temperature regions (e.g. Bergin et al. 1994, Öberg et al. 2014) and is therefore particularly advantageous for probing sources in relatively early evolutionary stages (Molinari et al. 2016), prior to hot core formation. Giannetti et al. (2017) showed that among various thermometers, the kinetic temperature constrained by CH_3CCH is representative of bulk gas temperature of massive clumps.

The H_2CS molecule is a near-prolate rotor. Its transitions between levels at various K ladders are also excellent indicators of the gas kinetic temperature (Blake et al. 1994). As a sulfur-bearing species, the gas phase H_2CS abundance can be enhanced either by direct evaporation or by outflow/shock sputtering (e.g. Bachiller & Gutiérrez 1997, Minh et al. 2011). Previous observations have also revealed that the H_2CS emission originates from extended warm regions surrounding compact hot cores (e.g. Helmich & van Dishoeck 1997).

3.4.2. Modeling procedure

Using the XCLASS package (Möller et al. 2017), we have established a pixel-by-pixel Local Thermodynamic Equilib-

rium (LTE) model-fitting procedure for the observed CH_3CCH , H_2CS , CH_3CN , and $\text{CH}_3\text{OH } \nu_t = 1$ (for G10) lines which returns the best fit of source size, rotational temperature (T_{rot}), molecular column density (N_{mol}), line width (ΔV) and the source velocity (V_{source}). In this specific implementation, we fixed the source size to the synthesized beam size (i.e., assuming beam filling factor of 1) and optimized the rest of free parameters. The optimization procedure employed an initial global parameter search using the bees algorithm (Pham et al. 2006) which was followed by Levenberg-Marquardt iterations. Such a procedure helps to avoid trapping in local minima. We fit the $J = 15-14$ and $J = 14-13$ ladders of CH_3CCH together, and the $J = 12-11$ ladders separately, given that the former lines show less extended emission and appear to trace hotter gas. Examples of the fitted spectra are presented in Figure 7-8. Examples of the obtained rotational temperature maps are shown in Figs. 9. When deriving these rotational temperature maps, we use pixels where the third lowest energy transition in consideration has intensity larger than our 3σ detection limit. For the hot molecular core G31, besides the aforementioned few molecular species that we targeted, the fittings also considered several other species that can potentially make a prominent contribution in our spectra. They are shown in Figure 7 for G31 in different colors. For clump G18, we do not have robust detection of these thermometer lines from our SMA observations and we rely on previous IRAM 30m telescope observations (Giannetti et al. 2017) to describe the temperature pro-

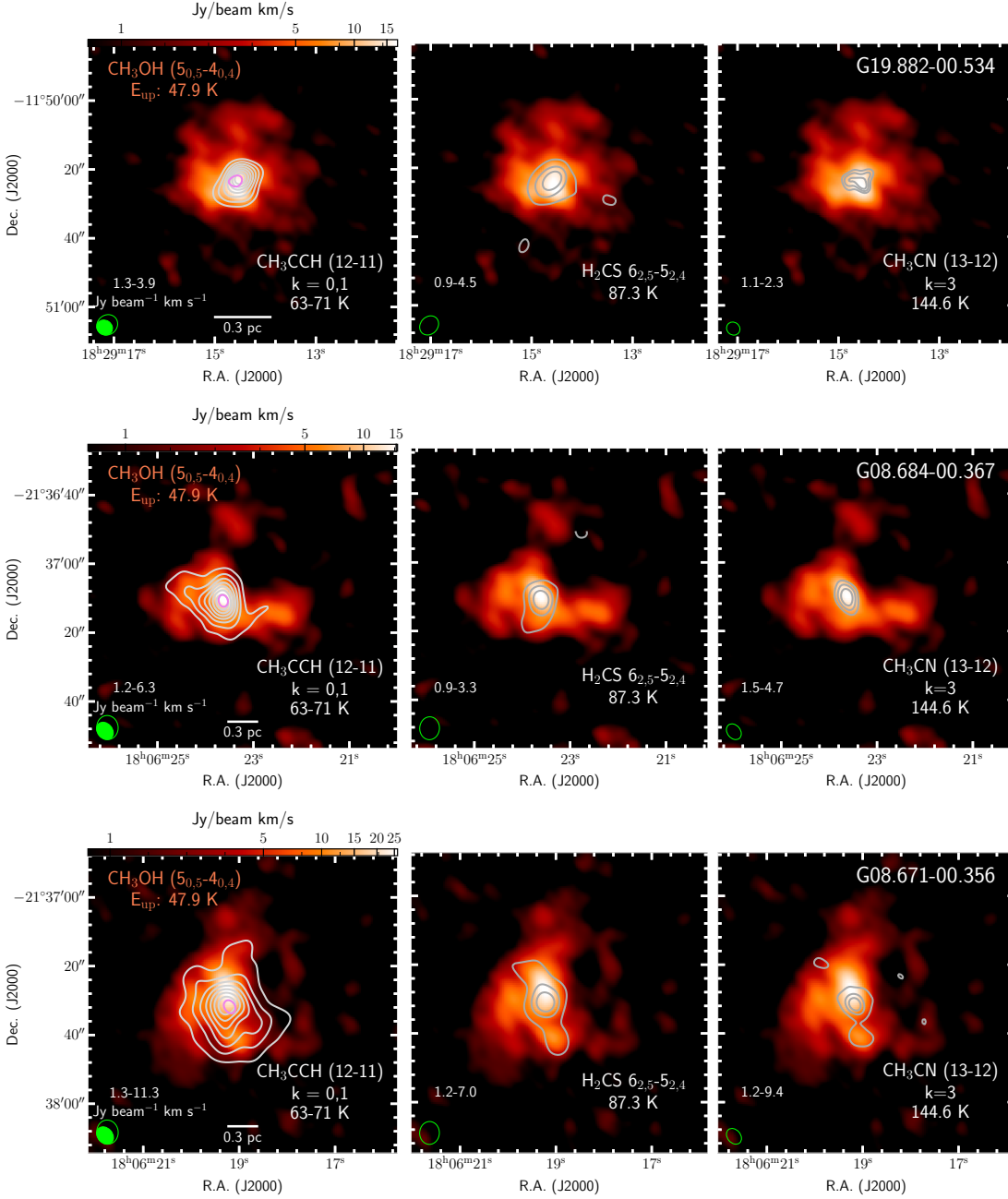


Fig. 5. Integrated intensity maps (gray contours) of CH_3CCH , H_2CS and CH_3CN toward sources G19, G08a and G08b. Integrated intensity of $\text{CH}_3\text{OH } 5_{0,5-4_{0,4}}$ ($[\nu_{\text{lsr}} - 3, \nu_{\text{lsr}} + 3]$ km/s) is shown in color scale. Gray contours show the intensity levels with uniform intervals from 5σ up to the peak flux, with the emission range ($\text{Jy beam}^{-1} \text{ km s}^{-1}$) indicated in the lower left corner of each panel. Magenta contour in the *left panel* shows the location of $0.8\times$ peak emission of the 1.2 mm SMA continuum image. The green ellipses indicate beams of corresponding molecular lines (void) and $\text{CH}_3\text{OH } 5_{0,5-4_{0,4}}$ line (filled).

file, with same thermometers but their lower transitions. These pointed observations from IRAM 30m telescope did not give information on relevant physical scales, rather, based on a fixed temperature profile ($T(r) \propto R^{0.4} L^{-0.25}$, Giannetti et al. 2017) the radius of a certain measured rotational temperature was deduced. Following the same workflow (Figure 4), these measurements are combined with one-component dust temperatures (Lin et al. 2019) in the outer region of the clump, to compose an initial temperature profile $T(r)$ to be refined later by SED comparison using RADMC-3D.

3.5. Deriving the pixel-based hydrogen volume density maps with non-LTE RADEX model

3.5.1. Methanol lines

Methanol (CH_3OH) is a slightly asymmetric top molecule. It has three types of symmetry, which are denoted as A, E1 and E2, respectively. The E1 and E2 states can be considered as doubly degenerate states of the E symmetry where the quantum number of the angular momentum along the symmetry axis of the CH_3 group (k) can take either positive and negative values. The torsional ground state $E\text{-CH}_3\text{OH } 5_{k,5} - 4_{k,4}$, $K = 0, \pm 1, \pm 2, \pm 3, \pm 4$

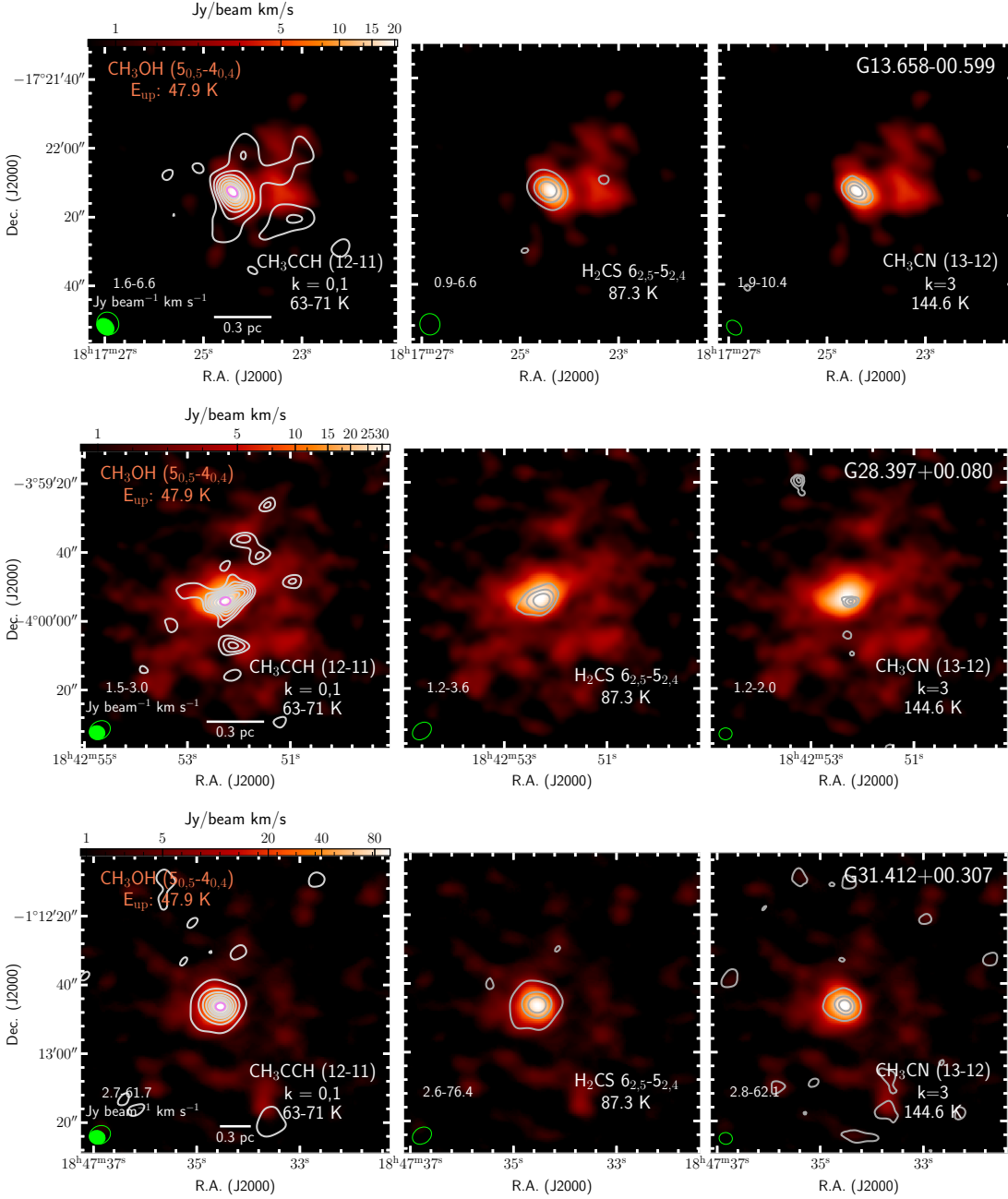


Fig. 6. Same as Fig. 5, but for target clump G13, G28 and G31.

($v_t = 0$) transitions were found to be a good densitometer for gas denser than 10^4 cm^{-3} (Leurini et al. 2004, 2007).

The excitation of these K ladders is usually observed to be sub-thermal. These $K = 0$ and $K = \pm 1$ ladders occupy a rather narrow range of upper level energies ($E_{\text{up}} \sim 40\text{-}55 \text{ K}$). At the same time, they cover a wide range of critical densities ($\sim 10^5$ to $\geq 10^7 \text{ cm}^{-3}$) (Table 4), which implies that the line ratios of two K components can be good density probes. The higher K components ($K \geq 3$, $E_{\text{up}} > 80 \text{ K}$) are generally excited in hot regions where the gas volume densities are close to or higher than the critical densities. Hence, ratios of the $K \geq 3$ components provide additionally constraints on kinetic temperature. Apart from the high abundance of CH_3OH , it is this property of the methanol energy system and the relatively low upper level energies of the $K < 3$ transitions that makes this line series sensitive to gas den-

sity for a broad range of physical conditions in molecular clouds (Leurini et al. 2004).

As illustrated in Figure 5, the CH_3OH emission appears clumpy and exhibits elongated structures, extending for up to 0.5 pc with respect to the continuum peak. The $K < 2$ transitions of $E\text{-CH}_3\text{OH}$ ($5\text{-}4$) ($v_t = 0$) are excited over an extended region, while the emission of the $K > 2$ lines are confined to the central region of the clumps.

3.5.2. Modeling procedure

We produced a series of large velocity gradient (LVG) RADEX models (van der Tak et al. 2007) to search for the best fits of $n(\text{H}_2)$, CH_3OH column density, $N(\text{CH}_3\text{OH-}E)/N(\text{CH}_3\text{OH-}A)$, and kinetic temperature (T_{kin}) to the observed CH_3OH ($J = 5\text{-}4$, $v_t = 0$) lines. We took the collisional rates from Rabli & Flower

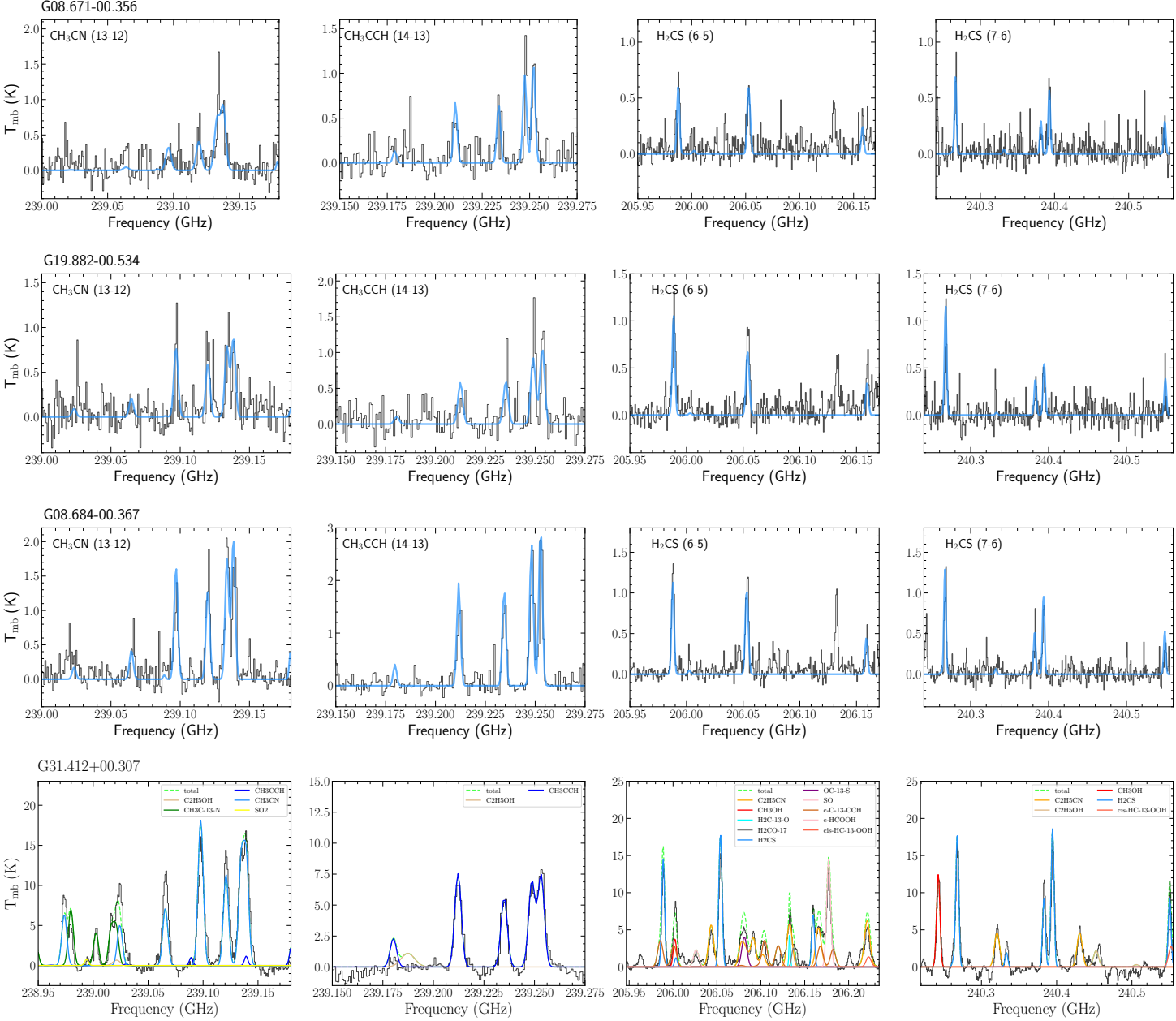


Fig. 7. Example spectra of thermometer lines $\text{CH}_3\text{CN } J=13-12$, $\text{CH}_3\text{CCH } J=14-13$, $\text{H}_2\text{CS } J=6-5$, $\text{H}_2\text{CS } J=7-6$ at the continuum peak of the target source; blue profiles show the XCLASS LTE fitting results. For source G31.412+0.307 which presents significant line blending from other species, the fittings also included those species/transitions that can potentially make prominent contributions to the spectrum.

(2010) which were evaluated for temperatures from 10 to 200 K. We adopt a Markov Chains Monte Carlo (MCMCs) method to derive the parameters and estimate the associated uncertainties, taking into consideration the upper limits for weakly detected line components. The details of the modeling procedure are elaborated in Appendix C where the formulas used for the likelihood function are given. In the fitting, for each pixel we enforce the posterior distribution of T_{kin} to be a narrow Gaussian distribution centred at $T(r)$ (more in Sect. 3.6) as measured in Section 3.4 from the multiple rotational temperature maps. Although the ratios between the lower K ladders of CH_3OH lines depend only weakly on the kinetic temperature, having a fixed term helps to avoid randomly converged parameters, which is useful to ensure that the resultant parameter maps are continuous. The obtained

$n(\text{H}_2)$ maps are shown in Figure 11. The CH_3OH column density maps are shown in Figure C.2.

3.6. Radial density and temperature profiles used in full radiative transfer models

We use the RADMC-3D code (Dullemond et al. 2012) in our full radiative transfer analyses (Figure 4; Sect. 3.1) for multi-wavelength dust continuum (Appendix E). We assumed that the gas density profile for the bulk gas ($\rho_{\text{bulk}}(r)$) is described by the following functional form:

$$\rho_{\text{bulk}}(r) = \begin{cases} \bar{\rho} \cdot \left(\frac{r}{r_c}\right)^q & (r \leq R_{\text{clump}}), \\ 0 & (r > R_{\text{clump}}), \end{cases} \quad (2)$$

Table 5. Parameters of CH₃OH derived radial density $\rho_{\text{dense}}(r)$ and multi-thermometer derived temperature profiles $T(r)$.

Source	$\rho_{0.1\text{pc}}$ $\times 10^6$ (cm ⁻³)	Power-law slope q_{dense}	R_{eff}^a (pc)	R_{max}^b (pc)	T_{in} (K)	r_{in} (pc)	T_{out} (K)	r_{out} (pc)
G18	2.9(0.2)	-0.26(0.07)	0.08	0.10	64.7(1.1)	0.016 ^e	19.2(0.1)	0.25(0.05)
G28	6.3(0.4)	-0.83(0.07)	0.20	0.30	96.1(1.2)	0.02	21.5(0.1)	0.80(0.10)
G19	5.3(0.3)	-0.61(0.05)	0.20	0.25	119.5(2.5)	0.008 ^e	21.2(0.1)	0.25(0.03)
G08a	10.3(1.2)	-1.33(0.12)	0.30	0.50	128.6(1.8)	0.008 ^e	22.4(0.1)	1.1(0.14)
G31 ^c	8660 (3000)	-3.22(0.37)	0.34	0.42	400.0 ^d	0.01 ^e	18.3(1.4)	0.27(0.03)
G08b	22.9(0.7)	-1.35(0.02)	0.34	0.50	135.0(1.4)	0.02	22.3(0.1)	0.80(0.08)
G13	9.1(1.8)	-1.67(0.20)	0.20	0.40	229.6(23.1)	0.004 ^e	17.0(1.5)	0.20(0.07)
G10	51.6(2.6)	-1.07(0.03)	0.28	0.42	172.4(4.8)	0.02	24.7(0.6)	0.90(0.31)

^a: Effective radius R_{eff} is defined as the $\pi R_{\text{eff}}^2 = A$, in which the A is the CH₃OH emission area where $n(\text{H}_2)$ can be reliably derived.

^b: The largest radius (distance to the center) of $n(\text{H}_2)$ map derived by CH₃OH; this is due to the irregular shape of the emission area.

^c: The density profile of source G31 is better described by a two-component power-law form consisting of a shallow slope in the inner region followed by a steep slope of $-5.22(0.045)$ in the outer region.

^d: Upper limit is set to 400 K in the fit.

^e: For sources G18, G19, G08a, G31 and G13, r_{in} is a re-adjusted parameter based on SED calculation and comparison presented in Figure 13 (temperature profile shown as blue lines in Figure 10).

Table 6. Best-fit parameters from RADMC-3D modelling of the dust continuum in 350/450 μm and 870 μm .

Source	$\bar{\rho}^a$ (10^3 cm ⁻³)	q^b	R_{clump} (pc)	$\rho_{0.1\text{pc}}^c$ (10^4 cm ⁻³)	M_{tot} ($10^3 M_{\odot}$)	L_{bol}^d ($10^4 L_{\odot}$)	$M_{\text{tot}} (< 0.5 \text{ pc})^e$ ($10^3 M_{\odot}$)
G18	14.8	-0.57	0.8	3.81	1.9	0.8	0.7
G28	12.3	-0.66	1.25	5.1	6.9	6.1	0.8
G19	7.8	-1.37	1.04	10.4	2.5	3.1	0.7
G08a	13.2	-1.19	1.00	12.3	3.8	3.5	1.1
G31	11.7	-1.22	2.18	29.9	35.3	57.0	2.6
G08b	3.6	-1.66	2.00	22.9	8.2	24.3	1.3
G13	9.5	-1.41	0.88	10.8	1.9	3.9	0.8
G10	7.8	-1.52	1.58	23.4	8.9	65.3	1.6

^a: Average density within clump radius of R_{clump} .

^b: Density power-law slope.

^c: Density at 0.1 pc.

^d: Bolometric luminosity calculated by using the SED profile shown in Figure 13 (blue lines for source G18, G19, G08a, G31 and G13).

^e: Total mass within 0.5 pc from clump center.

Table 7. Best-fit CH₃OH and CH₃CCH abundance results of LIME modeling based on density model from A: RADMC continuum modeling as listed in Table 6; B: manually-adjusted RADEX radial density profile as listed in Table 5.

Source	A							B						
	CH ₃ OH			CH ₃ CCH				CH ₃ OH			CH ₃ CCH			
	X_{out} ($\times 10^{-10}$)	T_{jump} (K)	f_{inc}^a	X_{out} ($\times 10^{-10}$)	T_{jump} (K)	f_{inc}	f_r^b	X_{out} ($\times 10^{-10}$)	T_{jump} (K)	f_{inc}	X_{out} ($\times 10^{-10}$)	T_{jump} (K)	f_{inc}	$f f_{\text{dens}}^c$
G28	10	30	10	10	30	10	3	1.5	80	150	0.018	30	200	0.13
G19	15	80	10	75	–	1	3	1.5	80	100	5	80	30	0.19
G08a	10	80	20	100	80	20	3	0.84	80	35	6	–	1	0.06
G31	2.5	80	10	20	80	10	50	4.0	120	8	12	120	2	0.09
G08b	10	80	5	100	–	1	5	0.6	80	40	5	80	70	0.05
G13	10	80	5	20	80	10	3	0.67	80	4	1.9	80	3	0.28
G10	10	80	5	–	–	–	7.5	0.54	40, 100	4, 75	–	–	–	0.05

Marker “–” denotes parameter invalid or not available.

a: f_{inc} represents increase factor of the abundance jump model (Equation 5).

b: Reduction factor applied to RADEX density results in the modeling (Equation 6).

c: Dense gas volume filling factor defined in Appendix F.

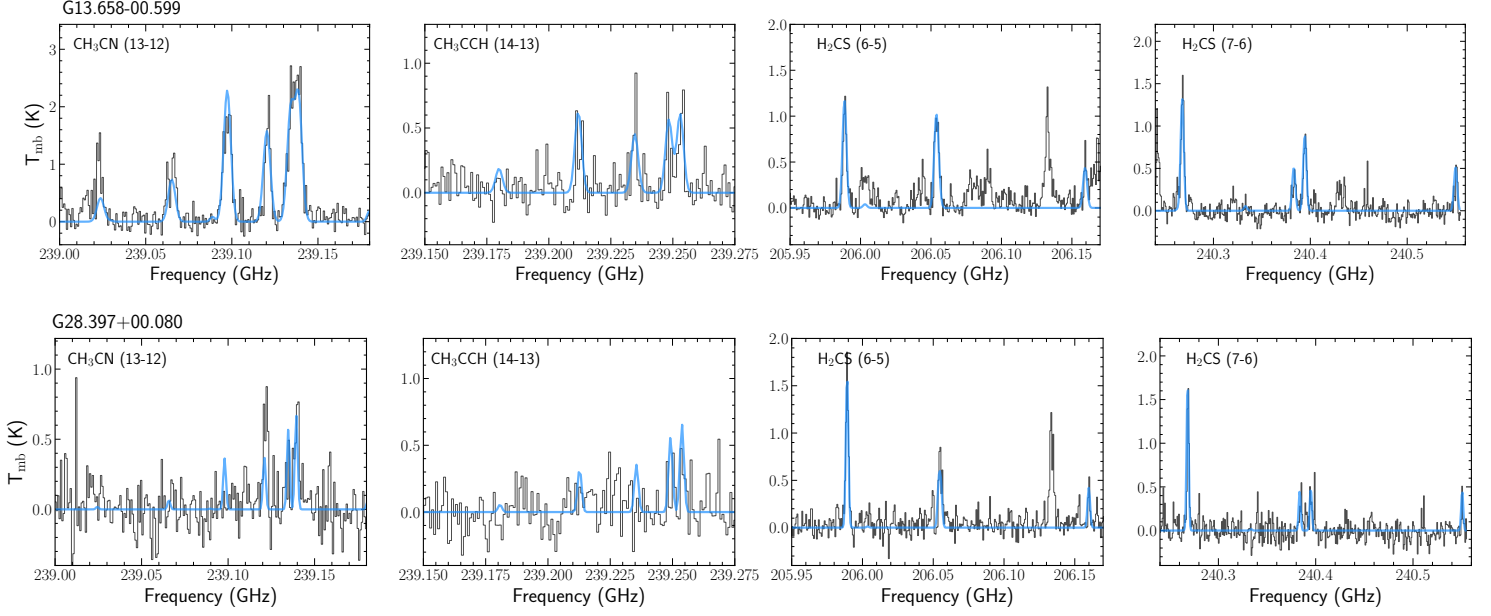


Fig. 8. Same as Figure 7, continued.

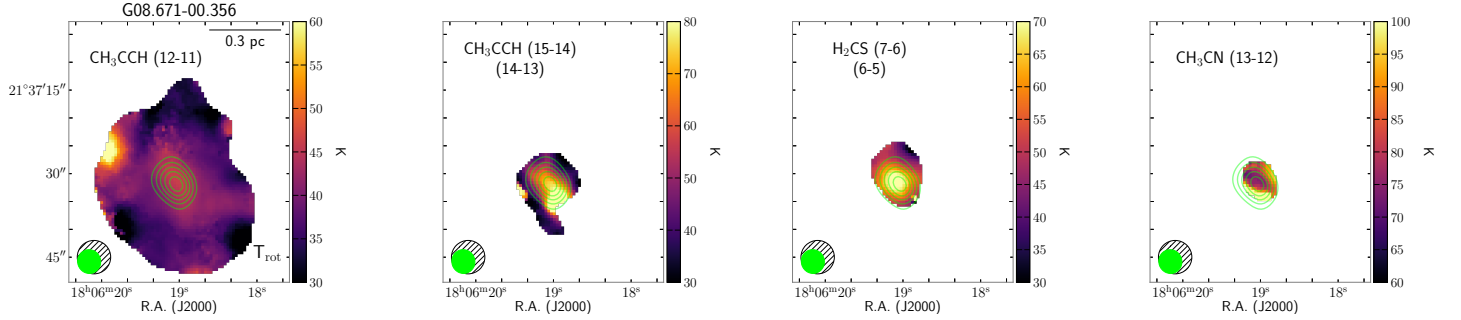


Fig. 9. Rotational temperature maps of source G08b derived from multiple thermometer lines using the XCLASS package (Section 3.4). Green contours indicate SMA 1.2 mm continuum levels from 0.3 to 0.9 \times peak flux (Table 2) by 5 levels of uniform interval. The beams of continuum and respective lines are shown in the lower left corner, as green and hatched ellipses.

where $\bar{\rho}$ is the mean hydrogen gas number density, and r_c is the radius where $\rho(r) = \bar{\rho}$, R_{clump} is the assumed outer radii of the clumps which were fixed to the FWHM measured from the ATLASGAL 870 μm maps (c.f., Contreras et al. 2013). When converting gas density to mass density, we assume that the mass per hydrogen molecule is $2.8 m_{\text{H}}$, where m_{H} is the hydrogen atom mass. We assumed that the gas-to-dust mass ratio is 100.

We parameterised the measured temperature profiles $T(r)$ by

$$T(r) = \omega T_{\text{in}} \left(\frac{r}{r_{\text{in}}} \right)^{-0.5} + (1 - \omega) T_{\text{out}}, \quad (3)$$

where $\omega = e^{-r/r_{\text{out}}}$ is an exponential tapering function characterized by outer radius r_{out} ; T_{in} and T_{out} are the characteristic temperatures at the radius r_{in} and at asymptotically large radii, respectively. In this equation, the first term describes radiative heating by the centrally embedded stars while the second term can be attributed to the ambient radiation fields of the massive clumps (Liu et al. 2019). The multiplicative factors ω and $(1 - \omega)$ prescribe the transition from one heating regime to the other.

Based on the multiple rotational temperature maps, we derived the (projected) radially averaged temperature profile and obtained best-fit parameters T_{in} , T_{out} and r_{out} , while r_{in} is initially kept as a fiducial value of 0.02 pc. Figures 12 and 13 show

the comparison between these multi-wavelength radial intensity profiles and the SEDs evaluated from best-fit RADMC-3D (Dullemond et al. 2012) models. Based on this comparison, we re-adjust the r_{in} of Equation 3 in the RADMC-3D modeling to obtain an SED profile consistent with the observed data points. $T(r)$ is then updated by the refined temperature profile. The parameters T_{in} , T_{out} , r_{in} and r_{out} that define $T(r)$ are listed in Table 5. With $T(r)$ defined, we fix the dust temperature profile in the multi-wavelength continuum modeling for the bulk gas and obtain $\rho_{\text{bulk}}(r)$; the best-fit parameters $\bar{\rho}$ and q as in Equation 2 are listed in Table 6.

From RADEX modeling of CH_3OH lines we constrain the radial density profiles for the dense gas, $\rho_{\text{dense}}(r)$, from the obtained $n(\text{H}_2)$ maps. Similarly, when deriving the $n(\text{H}_2)$ maps (Figure 11) we fix the gas kinetic temperature in the modeling to $T(r)$ for each pixel. We adopt a single power-law form as Equation 2 to characterize the dense gas density profiles, as

$$\rho_{\text{dense}}(r) = \rho_{0.1\text{pc}} \left(\frac{r}{0.1\text{pc}} \right)^{q_{\text{radex}}}, \quad (4)$$

where $\rho_{0.1\text{pc}}$ is the reference gas density at 0.1 pc. The description is valid up to a maximum scale of R_{max} , which is determined from the largest radius where $n(\text{H}_2)$ can be robustly estimated. These parameters are also listed in Table 5. Figure 14 shows the

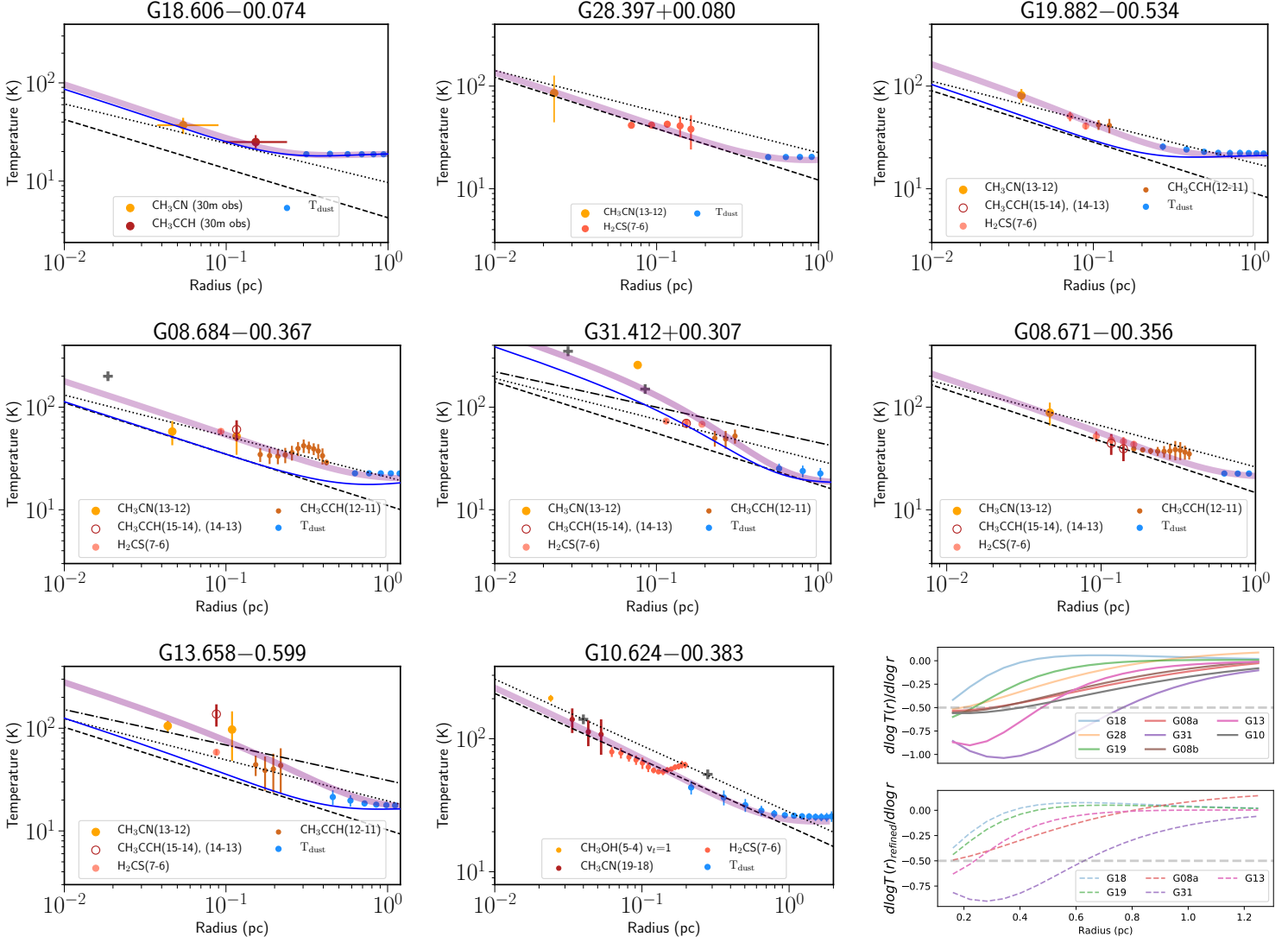


Fig. 10. Derived radial averaged temperature profiles of the target sources from multiple thermometers. Error bars are showing the standard deviations for each annular average. Dashed and dotted show a radial temperature profile that follows $\propto L^{0.25} r^{-0.5}$ ($\beta = 0$), $L^{0.2} r^{-0.4}$ ($\beta = 1$) respectively (more details see Sect. 3.6). For G13 and G31, an additional radial temperature profile of $\propto L^{0.17} r^{-0.34}$ ($\beta = 1.8$, Adams 1991) is shown (dashed dotted line). Whenever available, temperature measurement from higher angular resolution observations from previous work is included in the plots as gray crosses. Thick purple line indicates the fitted temperature profile $T(r)$ described in Section 3.6. Blue thin line indicates the refined temperature profile by varying r_{in} in $T(r)$ (Equation 3) to fit with dust SED (refined $T(r)$, Appendix E). Plot in the bottom right panel shows the first derivative, $d \log T / d \log R$, for all the sources, calculated from the fitted profile $T(r)$ and refined $T(r)$ (for 5 sources), in the upper and lower panel, respectively.

comparison between the model fits and the observed radial profiles.

We then conduct full radiative transfer modeling with LIME (Brinch & Hogerheijde 2010) to benchmark and refine these results. In the LIME modeling of CH_3OH and CH_3CCH lines, we first adopted the bulk gas density profile $\rho_{\text{bulk}}(r)$ constrained from single-dish dust continuum modeling, and $T(r)$ with assumed abundance profiles to find the best-fit models. We parameterized the molecular abundance profiles ($X_{\text{mol}}(r)$) as:

$$X_{\text{mol}}(r) = \begin{cases} X_{\text{out}} & (T(r) < T_{\text{jump}}) \\ X_{\text{in}} \equiv f_{\text{inc}} X_{\text{out}} & (T(r) > T_{\text{jump}}), \end{cases} \quad (5)$$

where T_{jump} is a threshold temperature chosen to be either 30 or 80 K, X_{out} is the abundance at outer radii, and f_{inc} is an increment factor to characterize the abundance enhancement in inner regions of higher temperature. This form is driven by previ-

ous chemical models of CH_3OH and CH_3CCH , in which prominent abundance enhancement is seen around the two T_{jump} temperatures (see also Appendix F). The best-fit parameters T_{jump} , X_{out} and f_{inc} for this model (hereafter model A) are listed in Table 7 (column A). For all sources, we find that with the assumed density profile of $\rho_{\text{bulk}}(r)$ the models cannot reproduce the observed high ratios between the higher and lower K components of CH_3OH lines, as shown in Figure 15 (presenting the comparisons between modelled results and observations towards clump G08a and G08b), which points to, as also indicated from the RADEX modeling results, a much higher gas density regime from which these CH_3OH higher K components originate. Therefore, we complemented the LIME models with density profiles of the dense gas component $\rho_{\text{dense}}(r)$ as in Equation

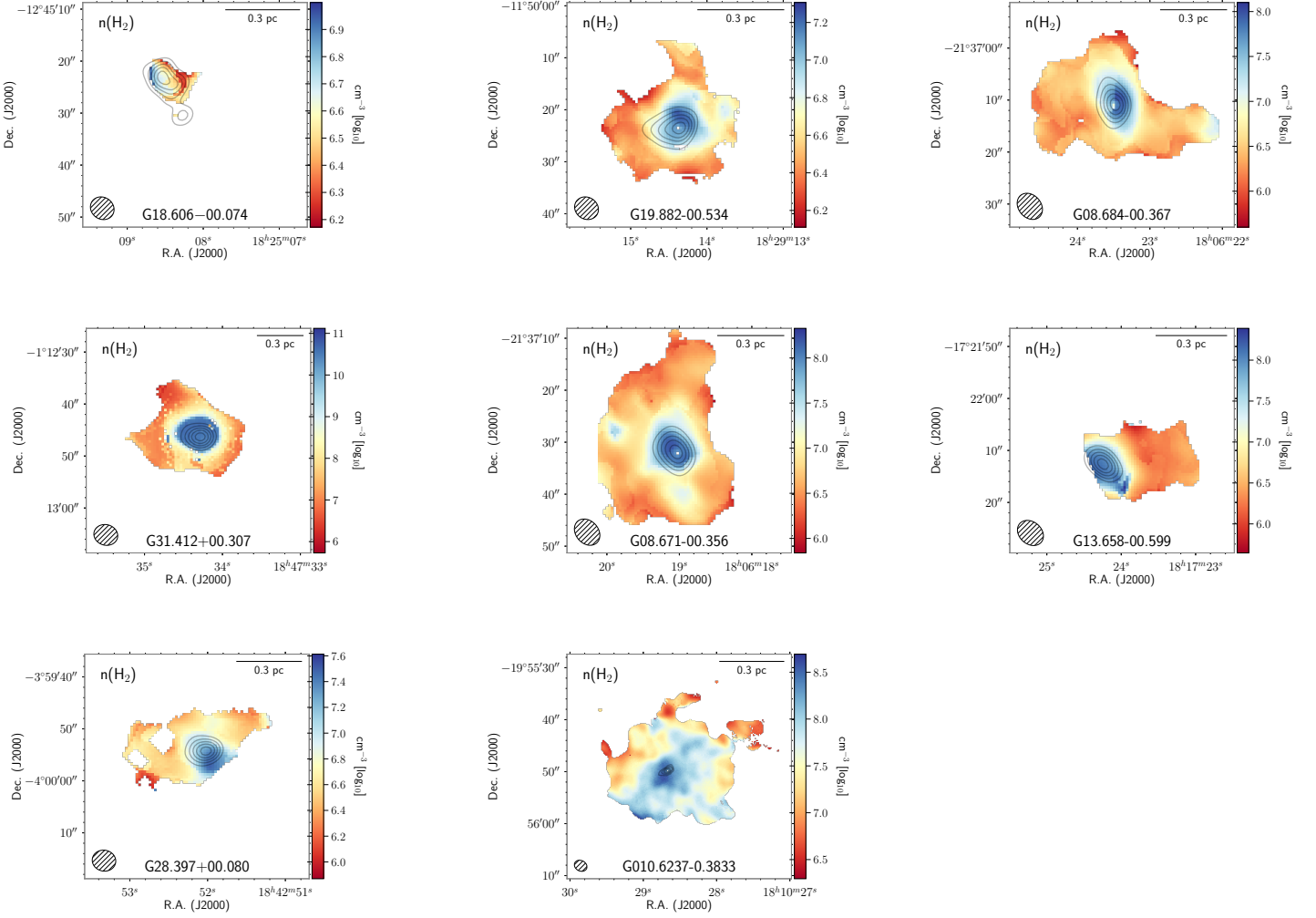


Fig. 11. CH₃OH derived $n(\text{H}_2)$ maps from RADEX modeling, of all target sources. The beam of CH₃OH 5₋₁-4₋₁ E line is indicated in the bottom left corner. Gray contours indicates the SMA 1.2 mm continuum level from 0.1 to 0.9×peak flux represented by 5 levels of uniform interval.

4 (the RADEX results of gas density radial profiles), following:

$$\rho_{\text{dense}}(r) = \begin{cases} \frac{1}{f_r} \rho_0 & (r < r_0) \\ \frac{1}{f_r} \rho_0 (r/r_0)^{q_{\text{radex}}} & (r_0 < r < R_{\text{max}}), \end{cases} \quad (6)$$

where r_0 denotes reference radius of 0.1 pc, or 0.05 pc (for G13 and G31); ρ_0 is the reference density at r_0 . These values, together with R_{max} were derived by RADEX modeling. Here f_r is a reduction factor applied to ρ_0 . This parameter is empirically added to the density profile so that the LIME models better match with the observed data. In essence, it means that RADEX results of one-component non-LTE modeling tend to overestimate the (projected) radial density in a 3D-structure clump. We manually adjusted f_r and $X_{\text{mol}}(r)$ to seek for better fits to the observational data. In what remains, we refer to q_{radex} as q_{dense} as this slope is fitted based on $n(\text{H}_2)$ maps of CH₃OH RADEX modeling and retained as the slope for the dense gas profile in full radiative transfer LIME models. The best-fit model parameters T_{jump} , X_{out} , f_{inc} and f_r for this model (hereafter model B) are summarized in Table 7 (column B). Figure 16 shows a comparison between the CH₃OH line profiles reproduced from model B and the observations towards clump G08a and G08b. The comparisons between model A, model B and observations for other target sources are shown in Appendix G.

3.7. A comparison of the samples: density and temperature structures

We make a comparison of the fitted and refined $T(r)$ profiles (Equation 3) of all sources in Figure 17 (left panel). We can see that, for all the clumps, at 0.1 pc the resolved gas temperatures range from 30-80 K, and at 1 pc at around 20-30 K. Moreover, the gas temperature at a certain clump radius is not a monotonic function of the bolometric luminosity of the clump. Particularly, the hot massive core G31 and the source G13 display higher temperatures in the inner regions than their immediate more luminous sources in the sample. We discuss these temperature profiles in more detail in Section 4.1.

In Figure 17 (right panel), we also compare the derived radial gas density profile of the dense gas from CH₃OH modeling with RADEX/LIME. It can be seen that $n(\text{H}_2)$ is several $\sim 10^5$ to 10^7 cm⁻³ at ~ 0.2 -0.3 pc (projected) radii. In the inner ~ 0.1 pc where the SMA identified continuum cores (Sect. 3.2), $n(\text{H}_2)$ ranges between several $\sim 10^6$ to 10^8 cm⁻³. There is exceptionally high $n(\text{H}_2)$ values at the center of G31. Although we have verified the high level of dense gas of this source compared with the rest of the sample by full radiative transfer modeling of CH₃OH lines (Appendix F), we caution that in this density regime CH₃OH (5-4) lines are becoming heavily optically thick and the critical den-

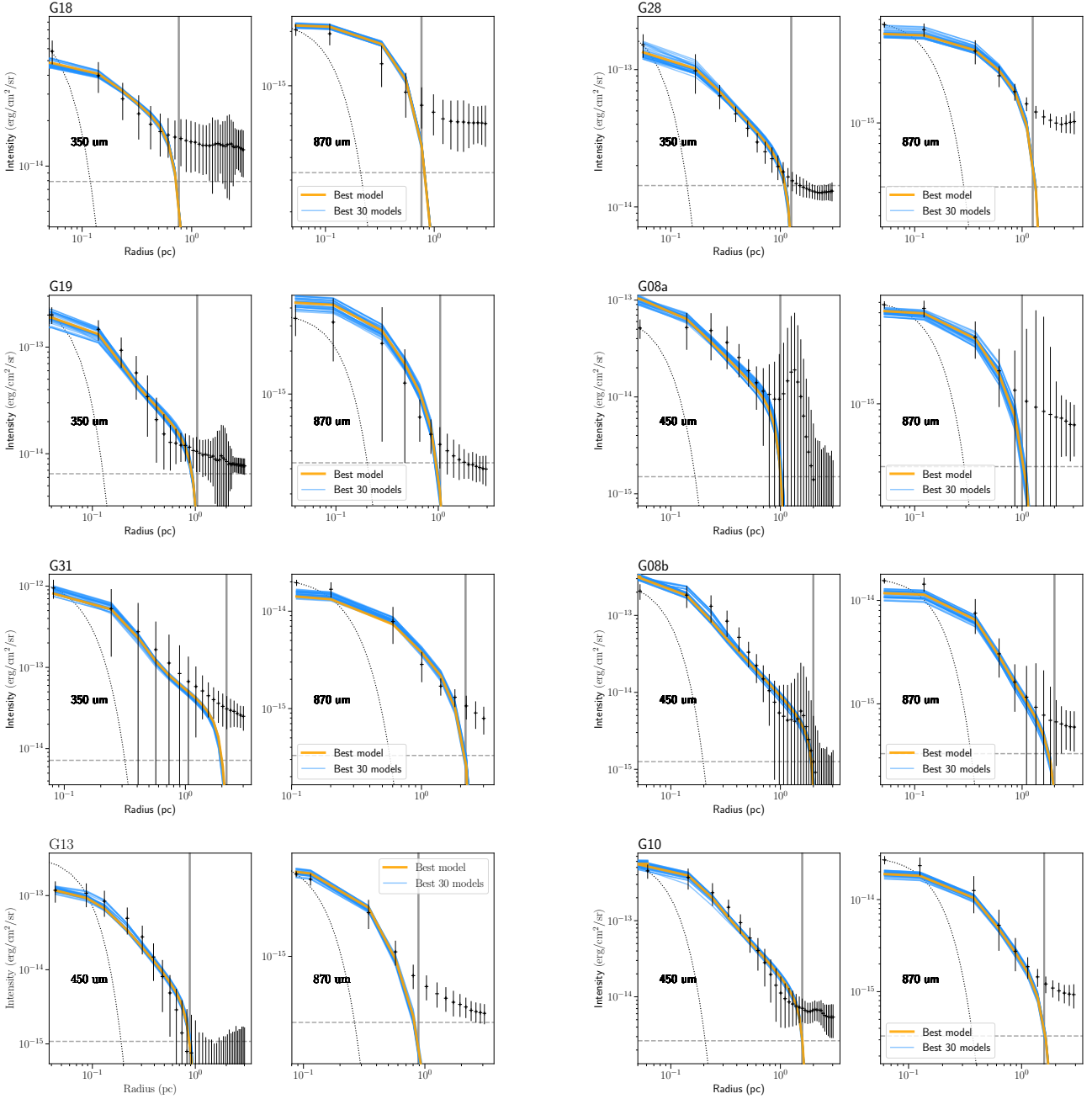


Fig. 12. Radial intensity profile comparisons between observations and best-fit RADMC-3D models. Gray horizontal dashed lines indicate the noise level (3σ). Gray vertical lines indicate the clump radius used in the modeling. Dotted line indicates beam shape in each plot. For source G18, G19, G08a, G13 and G31, model fit after re-adjusting $T(r)$ is shown. The gray vertical line indicates the clump radius R_{clump} .

sity for the considered line transitions is reached (e.g., $n > n_{\text{crit}}$, Table 4), such that the relative differences between the level populations do not serve as ideal densitometers anymore. Nonetheless, we can safely argue that the hot massive core G31 has much higher gas densities in its inner region than other sources, which is also reflected by the very monolithic nature of its central core from higher angular resolution observations (~ 2000 au, c.f., Beltrán et al. 2018). For source G10, there is prominently higher gas densities at extended radii of 0.1–0.4 pc than other sources, which is related to the presence of a large disk-like flattened structure. We discuss further on the density profiles among the sample in Section 4.2.

We compare the steepness of the radial gas density profiles (q_{bulk} and q_{dense} , for ρ_{bulk} and ρ_{dense}) as a function of source evolutionary stages, which is indicated by the clump bolometric luminosity to mass ratio L/M (Figure 18). Using Spearman correlation measure, we find that there are positive correlations (correlation coefficient $\rho = -0.95$ and -0.65) between the density power-law slopes with L/M , for both the dense gas component and the bulk gas structures, although the significance of the correlation of the former is low (p-value = 0.15). The slopes range from -0.6 to -1.7 for the bulk gas, and -0.25 to -1.7 for the dense gas, for L/M spanning from 10 to ~ 100 (L_{\odot}/M_{\odot}) of all sources. The correlation between L/M and the density slope representing the bulk gas distribution is clearly stronger. A similar evo-

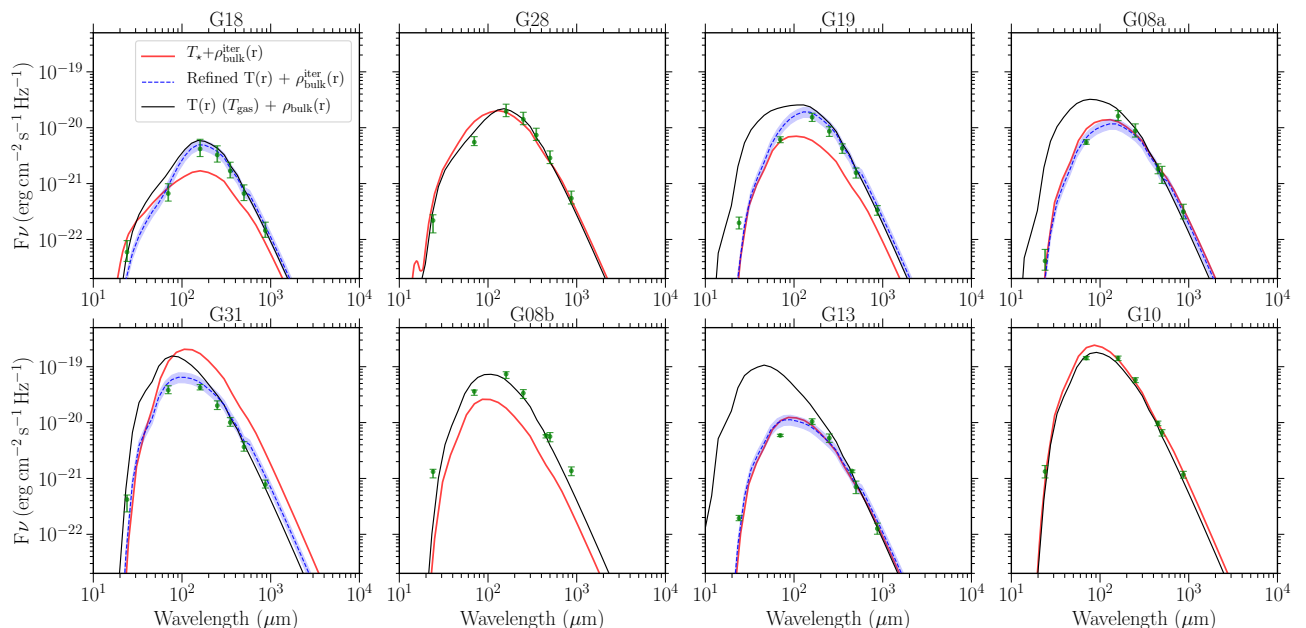


Fig. 13. Comparison of SEDs of the best-fit RADMC-3D models with measured multi-wavelength fluxes (in green dots with error bars indicating 0.8 and 1.2 times the flux level) for each source. Black line indicates the SED generated from assumed $T(r)$ and the corresponding best density profile fits. Blue dashed line indicates the SED generated from refined $T(r)$ and the re-iterated best density profile fits. Blue shaded regions indicates 20% difference around the blue dashed SED profile. Red line shows the SED generated by self-consistently calculating the dust temperature adopting a central heating ZAMS star plus the re-iterated best density profile (for more details see Appendix E).

lutionary trend was reported by Beuther et al. (2002a) based on analyses of 1.2 mm dust continuum emission of a sample of massive clumps, in which the bulk gas density structure was probed. Comparably, other works on the density structures of massive clumps typically derived power-law slopes ranging in -2.25 – -0.75 and peaking at -1.8 – -1.6 (Mueller et al. 2002, Beuther et al. 2002a, van der Tak et al. 2000). In the early-stage sources ($L/M < 20$), the slopes we derived are relatively shallow (> -1.0) for both the bulk gas and dense gas density structures. We note that the slope derived for the dense gas structure of the early-stage source G18 is valid for a confined region of ~ 0.1 pc (just above the beam size), which merely reflects a pocket of dense gas that is rather compact and remains unresolved. Yet, for other early-stage sources, i.e. G28 and G19, the statistics for determining the density slope are rather adequate, and these two sources do exhibit shallow slopes of ~ -0.6 . We note that different analysis methods of density structure could result in systematic biases in the derived density slopes. In addition, the analyses of dust continuum that were based on the optically thin assumption, instead of relying on full radiative transfer models, suffer from the degeneracy of density and temperature profiles in determining the radial intensity profiles. Moreover, close to the source center, the optically thin assumption for dust emission may also break down. Although qualitative comparison can be made, a careful gauge between different analysis conducted are necessary for a stringent comparison between different works. In Sect. 4.5 we discuss further on the relation between density profiles of massive clumps and statistics on cloud structure. We also elaborate on physical implications by comparing ρ_{bulk} and ρ_{dense} , among the sample.

3.8. Molecular linewidths and virial parameter

To understand the dynamic states of the target clumps, we examined how the linewidths and virial parameters vary with clump radii. Part of these analyses were based on the thermometer lines, CH_3CN , H_2CS and CH_3CCH . They primarily trace the dense gas close to the centers (0.1–0.4 pc) of the clumps. In addition, we examined the CS and C^{34}S (5–4) and H^{13}CO^+ (3–2) lines which can trace spatially more extended clump structures due to their lower excitation conditions. We performed single component Gaussian fits to the CS , C^{34}S (5–4) and H^{13}CO^+ (3–2) line cubes in a pixel-by-pixel manner to obtain the linewidth maps. For the analysis, we trimmed the pixels that have fitting errors of linewidth larger than 2 times the velocity channel widths ($\Delta V < 2$ km/s).

The virial parameter α_{vir} characterizes an important aspect of the physical states of the molecular clumps. The ordinary definition of α_{vir} (i.e., ignoring magnetic field; c.f., Bertoldi & McKee 1992) is

$$\alpha_{\text{vir}} = a_1 \frac{2T}{|W|}, \quad (7)$$

where $T = \frac{3}{2} M_{\text{enc}} \sigma_{\text{rms}}^2$ is the kinetic energy, $W = -\frac{3}{5} a_1 \frac{GM_{\text{enc}}^2}{R}$ is the gravitational potential energy, M_{enc} is the enclosed mass, and a_1 is a geometric factor which accounts for the inhomogeneity of the density distribution (e.g. Bertoldi & McKee 1992, McKee & Holliman 1999). For a spherical clump that has a $\propto r^{-q}$ radial gas density profile, $a_1 = \frac{1+q/3}{1+2q/5}$. With this definition, a source in energy equipartition ($T \sim |W|$) has a critical virial parameter of $\alpha_{\text{cr}} = 2a_1$. In a virialized source ($2T \sim |W|$), it stands that $\alpha_{\text{vir}} = a_1$ with $\alpha_{\text{vir}}/\alpha_{\text{cr}} = 0.5$. In the following we refer to the states of $\alpha_{\text{vir}}/\alpha_{\text{cr}} < 0.5$, ~ 0.5 – 1 and > 1 as sub-virial, virial and super-virial state, respectively.

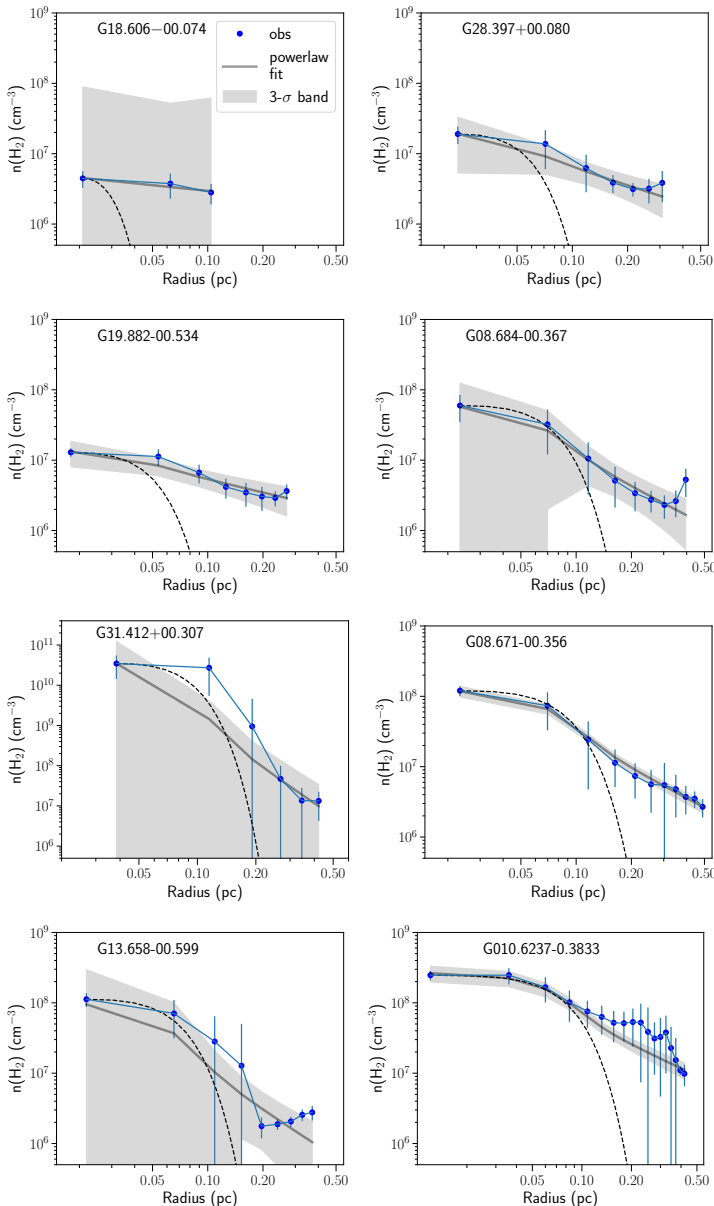


Fig. 14. Projected radial averaged $n(\text{H}_2)$ radial profiles derived from $n(\text{H}_2)$ maps shown in Figure 11. Thick gray line indicates the best-fit single power-law model (beam convolution considered). Gray shadowed band indicates the 3σ confidence band of the best-fit model. The model parameters and 1σ errors are listed in Table 5.

When deriving α_{vir} , it is critical that the tracers observed for the measurement of M_{enc} and σ_{rms} are predominantly emanated from the same gas entity (Traficante et al. 2018). The mass tracer we adopted, which is the dust continuum emission, traces a broad range of gas volume density distributed in a wide range of radius. Our selected tracers to indicate linewidths, as the way the temperature profile is measured, show emission of progressively larger radii, which are complemented with two more extended tracers. We can now examine spatial variation of linewidths and α_{vir} based on multiple tracers that cover distinct critical densities (Table 4), and hence different spatial scales. We evaluated how $\alpha_{\text{vir}}/\alpha_{\text{cr}}$ varies with radius using the best-fit density models from the RADMC-3D continuum modeling (Appendix E) to obtain M_{enc} , a_1 and the linewidth maps from aforementioned tracers. Note that as compared with the SMA observa-

tions, the RADMC-3D models constrained by the coarser resolution single-dish continuum data systematically under-predicted the 1.2 mm fluxes in the inner radii. To avoid this bias, we adopt the M_{enc} as $M_{\text{core}}^{\text{Abel}}$ (Sect. 3.2) for the inner regions. We recall that $M_{\text{core}}^{\text{Abel}}$ is calculated by applying the derived $T(r)$ to SMA 1.2 mm continuum. We discuss the obtained radial profiles of linewidth and virial parameter in Sect. 4.3.

3.9. Molecular abundance and abundance ratios

To facilitate the analysis on clump evolutionary stages, we derived the LOS integrated abundance maps ($N_{\text{mol}}/N(\text{H}_2)$) for some relevant molecular species for all sources. The bulk gas density profiles ($\rho_{\text{bulk}}(r)$, Sect. 3.6, and Appendix E) were adopted and smoothed to the angular resolution of the specific line transition when deriving $N_{\text{mol}}/N(\text{H}_2)$. The calculation of N_{mol} for CH_3CCH , CH_3CN , H_2CS and CH_3OH is introduced in Sect. 3.4 and Section 3.5. The calculations of N_{mol} maps of $\text{CS}/\text{C}^{34}\text{S}$, SO , SO_2 and CCH lines were based on LTE assumption and are detailed in Appendix D. We then derived the projected radial averaged abundance profiles for each molecule. Naturally, the projected radial averaging suppresses the contrast in the spatial variations of the abundance for the molecules that are enriched in the clump center or other localised regions (which reduces $N(\text{H}_2)$ to localised values rather than integration along the LOS extension). Nevertheless, this does not qualitatively change the overall radial trends as long as the abundance is increasing or decreasing with radius monotonically, with a steeper profile than that of the column density, while the latter is rather shallow, following $\Sigma \propto \rho r \propto \rho^{1+q} < \rho^{-0.7}$. In Figures 19-20, we show the relations between the clump bolometric luminosity and the radial abundance variations of the carbon-chain and sulfur-bearing molecules in consideration, respectively.

From Figure 19 we note that the abundances of CH_3OH , CH_3CCH and CH_3CN show similar behaviors. They appear largest in the hot massive cores G31; in the rest of the sources, the abundances of CH_3OH and CH_3CCH are in the range of several 10^{-9} - 10^{-8} , while the abundances of CH_3CN are in the range of 10^{-10} - 10^{-9} . These abundances are slightly positively correlated with the clump luminosity. The abundances of CH_3CN and CH_3OH appear more tightly correlated with the source temperatures in the inner ~ 0.1 pc regions (see the insets in Figure 19). These trends are consistent with theoretical predictions that the de-sorption of these molecules from grain surface is more efficient with higher temperature. We note that these results cannot be obtained if the gas temperature distributions were derived based merely on the assumptions of bolometric luminosity scaling instead of being derived based on multi-transition rotational temperature maps, since we have previously seen that the gas temperatures at certain radii do not necessarily increase monotonically with clump luminosity (Figure 17, left panel). This result demonstrates the importance of measuring detailed temperature profiles when studying chemical evolution.

We observed a weak correlation of abundance of CH_3CCH and bulk gas temperature, which is reminiscent of the small variation of the CH_3CCH abundance towards massive clumps of various evolutionary stages reported by Giannetti et al. (2017) (see also Öberg et al. 2014). Other higher angular resolution observations of this species indicated a mixed behaviour of its spatial distribution, depending on whether the emission coincides with the localised hot cores or appears offset and/or showing more extended structures (Bøgelund et al. 2019, Öberg et al. 2014, Fayolle et al. 2015). Comparing rotational temperature maps of CH_3CCH (12-11), the temperatures of G13 and G31 in the core

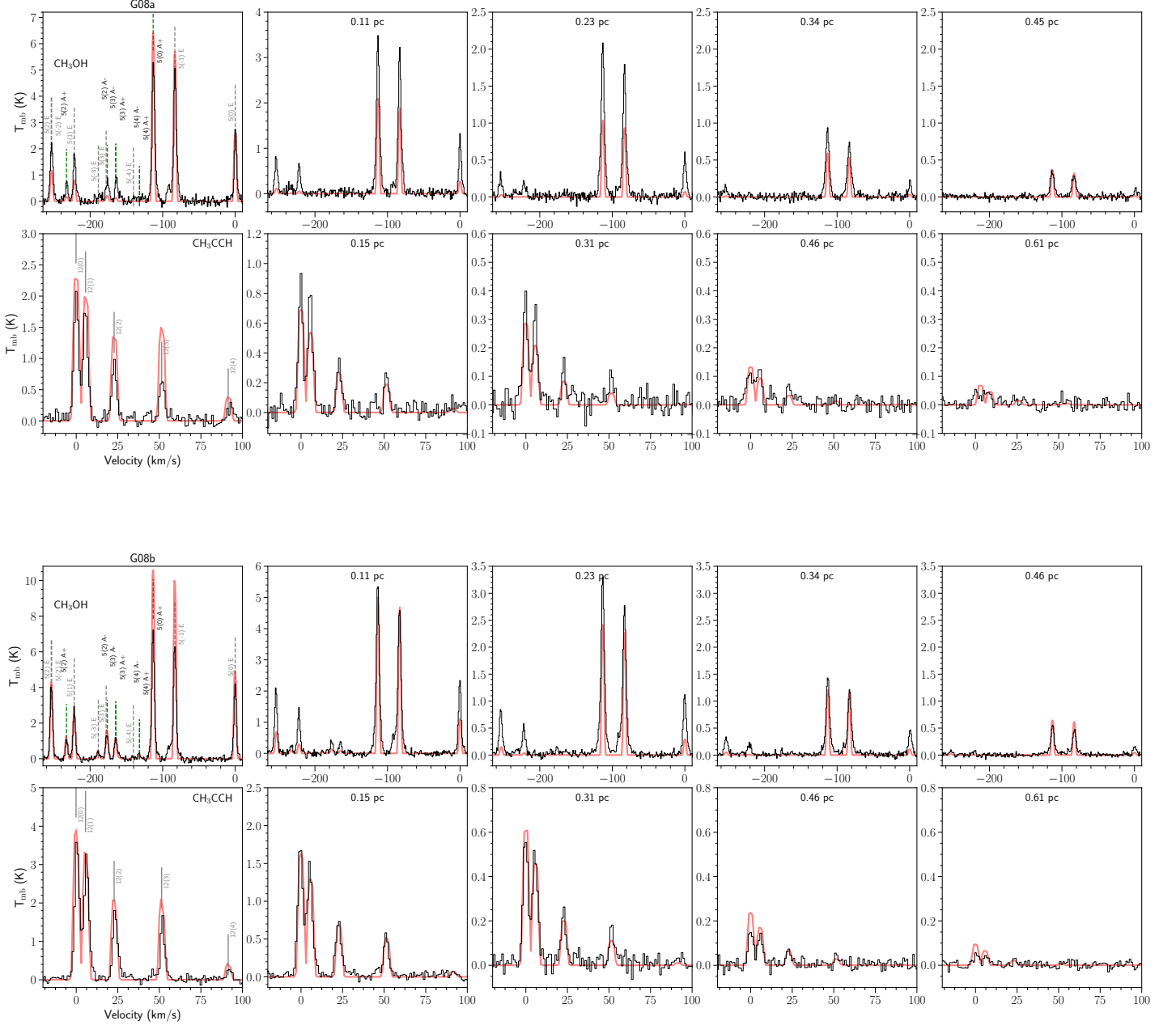


Fig. 15. LIME modeling result (best-fit parameters listed in Table 7, column A) based on best-fit density model from RADMC-3D continuum modeling. From left to right: annular beam-averaged spectra from the continuum center to the outer envelope. Considering the typical beam FWHM of our observations: the distance from the center of each annular region to the center of the source is marked on top of each spectra. The line components of *A* and *E*-type CH_3OH are indicated with short dashed vertical lines in green and gray, respectively.

region is 20-30 K higher than those of G19, G08a and G08b. In addition, the higher *J* transitions CH_3CCH (14-13), (15-14) trace systematically higher temperatures in the core region towards all sources. This evidence indicates that the emission of CH_3CCH does have contribution from gas components residing inside or in the vicinity of hot cores. As for the result of CCH, except for the earliest-stage source G18, its abundance appears enhanced at outer radii. We can also see that the abundance of CCH measured in the inner ~ 0.1 - 0.2 pc region is anti-correlated with the clump luminosity. These results are consistent with previous observations that show shell-like CCH emission towards late-stage

massive star-forming regions (Beuther et al. 2008, Jiang et al. 2015).

The abundance ratios of CCH, CH_3CCH and CH_3CN with CH_3OH in the clump center (0.1-0.15 pc) are shown in Figure 21. Here, normalisation with CH_3OH allows exploring the chemical evolution or initial condition by eliminating the effect of different desorption levels among the sample. There are substantial variations of $[\text{CCH}]/[\text{CH}_3\text{OH}]$ and $[\text{CH}_3\text{CN}/\text{CH}_3\text{OH}]$ across L/M , while variations of $[\text{CH}_3\text{CCH}/\text{CH}_3\text{OH}]$ appear moderate.

The abundances of sulfur-bearing species in the central regions of the clumps also show correlation with temperatures

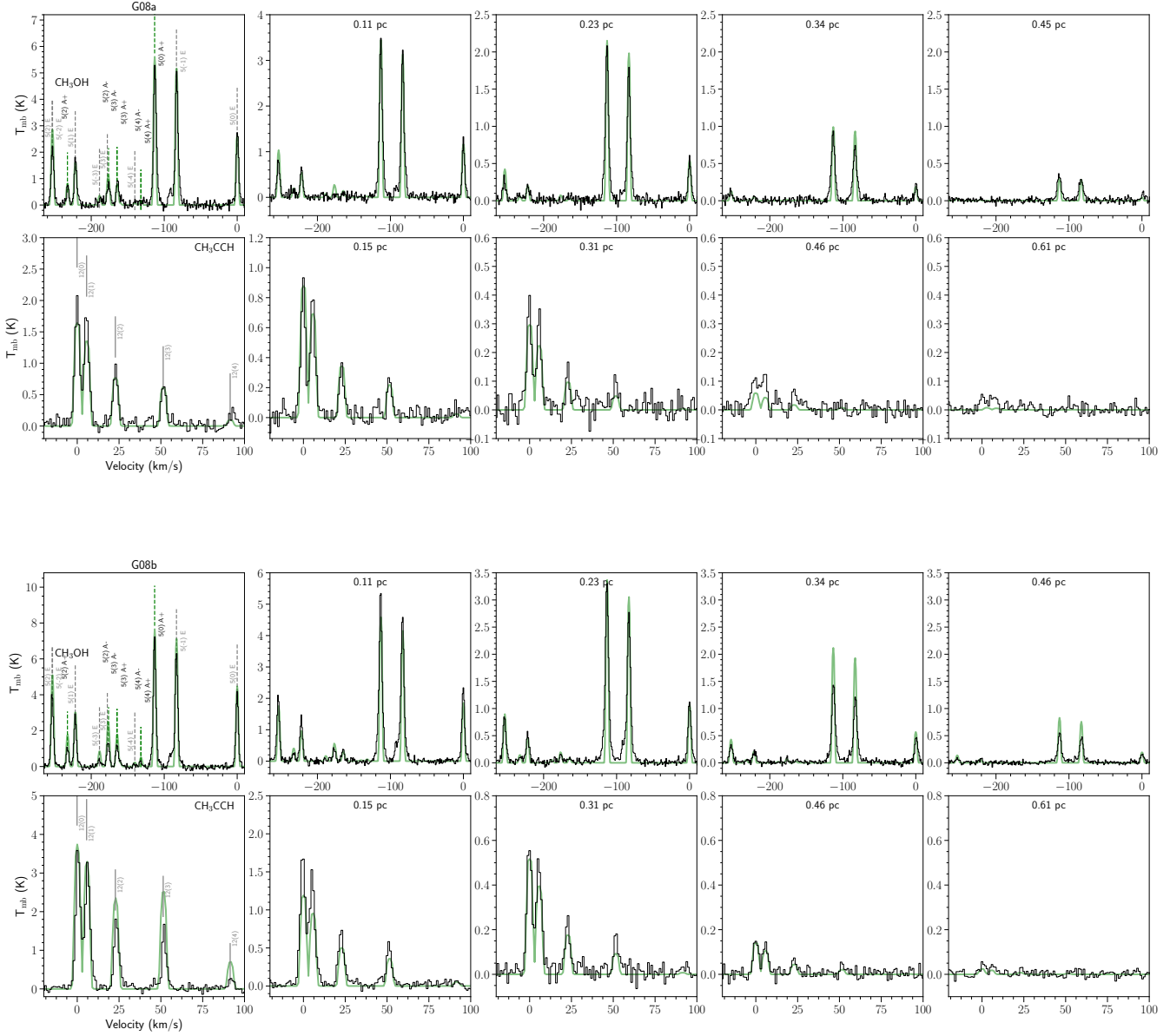


Fig. 16. LIME modeling result (best-fit parameters listed in Table 7, column B) after manually adjusting the density profile obtained from RADEX modeling (Eq. 4), which is prescribed as a piecewise power-law (Eq. 6). From left to right: annular beam-averaged spectra from the continuum center to the outer envelope. Considering the typical beam FWHM of our observations: the distance from the center of each annular region to the center of the source is marked on top of each spectra.

(Figure 20). Comparing the relative abundance of $C^{34}S$ and H_2CS with respect to SO as a function of L/M (Figure 21, bottom panel), it seems there is a mixed behaviour: except for source G13, the other sources show an increasing trend. On the other hand, for $X(SO_2)/X(SO)$ there is a consistently increasing trend with source L/M . We discuss the abundance variations further in Sect. 4.4 in a broader context, with comparisons with published results from chemical modeling.

4. Discussion

4.1. Temperature structure and heating mechanisms of massive star-forming clumps

The temperature measurement from multiple T_{rot} maps and the fitted and refined temperature profile $T(r)$ (Equation 3) are shown in Figure 10. The $d \log T / d \log R$ profiles are also summarized in the bottom right panel. Except for sources G13 and G31, the $d \log T / d \log R$ profiles asymptotes from -0.5 to zero from inner to outer radii. The levelling-off of the temperature at the outer radius of the clump is expected since all these massive star-forming clumps are immersed in intense interstellar radiation fields. At gas densities $> 10^{4.5} - 10^5 \text{ cm}^{-3}$, thermal coupling between gas and dust can be quickly achieved due to col-

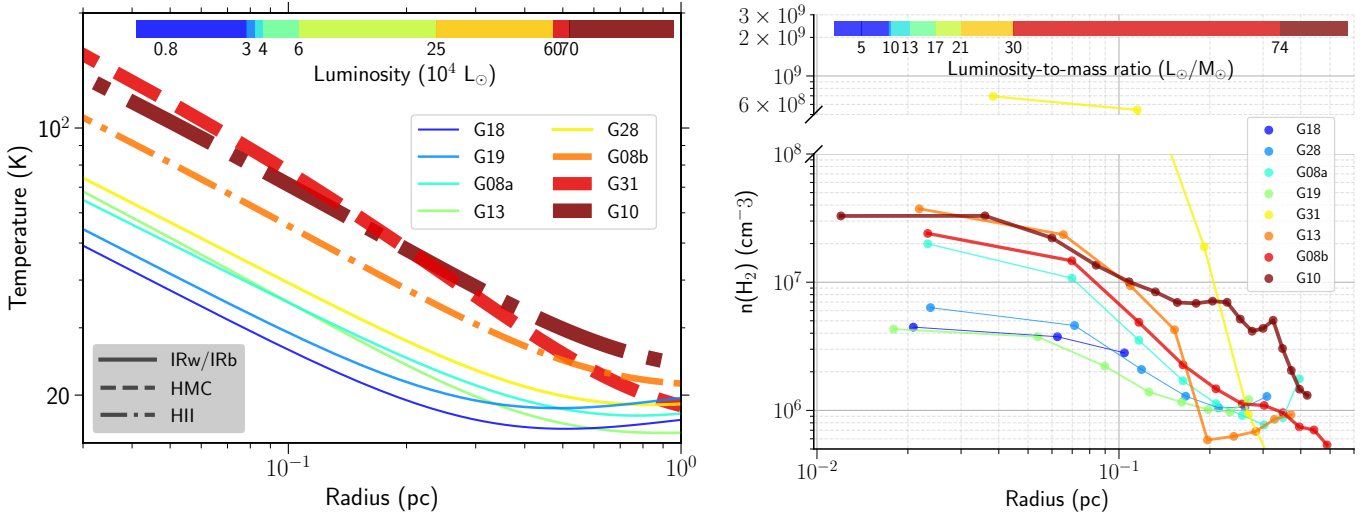


Fig. 17. *Left panel:* Radial temperature profiles $T(r)$ for all the target sources (Equation 3, refined $T(r)$ is used for the relevant source). The thickness of the lines increases with increasing luminosity. *Right panel:* The radial (projected radial averaged) density profile of the dense gas (ρ_{dense}) of all the target sources, from $n(\text{H}_2)$ maps derived by RADEX modeling of CH_3OH lines. The range of the y axis is trimmed to increase contrast. For both panels, the luminosity and clump mass are calculated from RADMC-3D best-fit model (Table 6), which takes into account all the gas component present in the clumps.

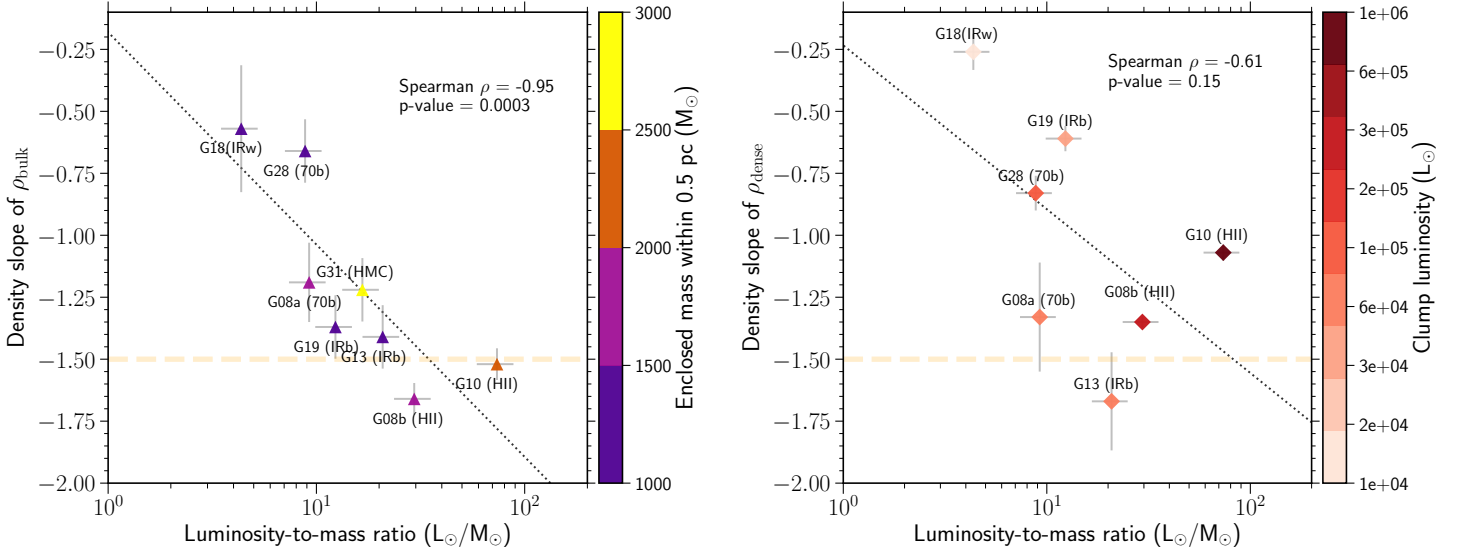


Fig. 18. *Left panel:* Density power-law slope derived from continuum (q) based on RADMC-3D modeling detailed in Appendix E. The luminosity, clump mass and enclosed mass within 0.5 pc are calculated from RADMC-3D best-fit model, as listed in Table 6. *Right panel:* Density power-law slope derived from $n(\text{H}_2)$ maps (q_{radex}) from CH_3OH RADEX modeling detailed in Sect. 3.5. Yellow horizontal line in both plots shows a slope of -1.5, indicating the free-falling density profile of a singular isothermal sphere (with an initial density slope of -2) as in Shu 1977, and the attractor solution of the gravo-turbulent collapsing in Murray et al. (2017).

lisions (Goldsmith 2001; Glover & Clark 2012). However, the $10^{4.5} \text{ cm}^{-3}$ density threshold is not met in the outer layers of the sources which have lower masses. As we will explain below, the thermal decoupling between gas and dust is seen in some of these sources. The outer envelope dust temperature for all these sources flattens around 18-25 K. These values are consistent with an elevated infrared radiation field associated with these regions. Based on these temperatures, the scaling factors of the local ISRF (Mathis et al. 1983) to characterise the radiation field surrounding these clumps are roughly $\geq 10^{2.5}-10^4$ (estimated in the optically thick limit, Krumholz 2014), which are typical values found in the vicinity of Galactic massive star-forming complexes (Binder & Povich 2018).

The $T(r)$ and $d \log T / d \log R$ in the inner regions may be approximated by the analytic temperature profile of thermally balanced dust grains distributed around a central heating point source (e.g. Adams 1991). With optically thin condition and a submillimeter dust opacity spectral index (β), the model of Adams (1991) predicted that the radial temperature profile for dust grains in thermal balance around a central heating point source is proportional to $r^{-2/(4+\beta)}$. If β has no spatial variations, then $d \log T / d \log R$ should be a constant of radius. In the diffuse interstellar medium β is around 1.8 (for a review see Hildebrand 1983), which yields a temperature slope of ~ -0.35 . In high-density regions, β may become lower due to dust growth (e.g. Ossenkopf & Henning 1994), resulting in a steeper temper-

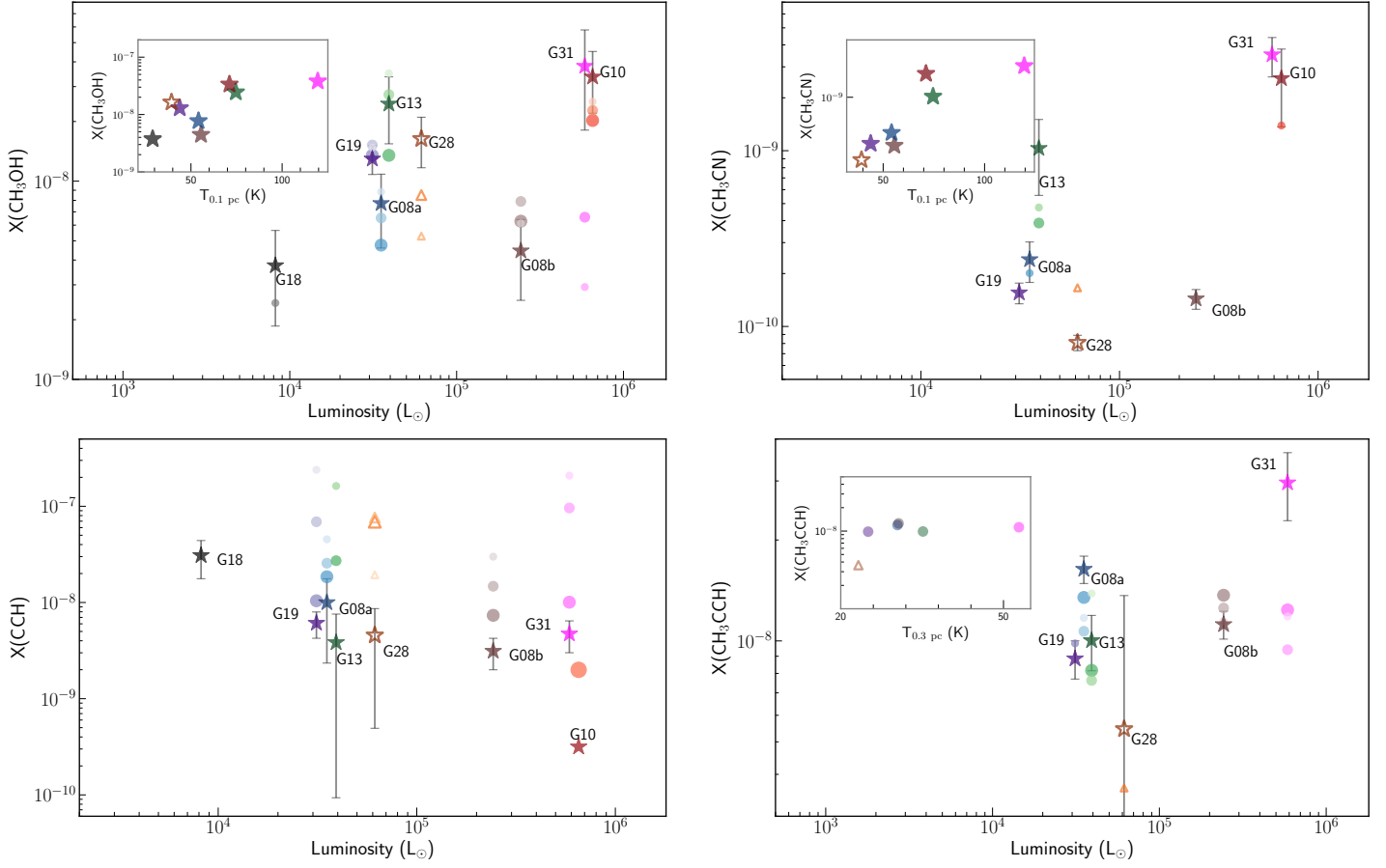


Fig. 19. Abundance profiles of molecules CH_3OH , CH_3CN , CCH and CH_3CCH towards target sources. Markers are color-coded based on relative distance to the clump center (the 1.2 mm continuum peak). Stars represent abundances at the clump centre, whereas hollow circles or triangles indicate abundances obtained from different radii: the larger and darker the latter markers, the closer distance to the continuum peak they represent. For clump G28, the data points at outer radii are marked as triangles, whereas those for other clumps are marked as circles, to further avoid confusion. $X(\text{CCH})$ for source G10 is taken from Jiang et al. (2015). The inset plot for CH_3CN shows the central abundance vs. gas temperature at 0.1 pc; for CH_3CCH shows the envelope abundance vs. gas temperature at 0.3 pc.

ature profile. Values of β lower than 1.8 have been reported by some previous observations towards Class 0-II young stellar objects, and towards protostellar and prestellar cores (e.g. Beckwith & Sargent 1991, Jørgensen et al. 2007, Bracco et al. 2017, and references therein). It should be caveated that the previous (sub)millimeter observations of dust growth might have systematically underestimated β values owing to underestimating optical depths (e.g., Li et al. 2017), neglecting the effect of dust scattering opacity (e.g., Liu 2019), as well as the effects of temperature mixing when performing SED fittings (e.g. Juvela et al. 2018). From a modern point of view, on the spatial scales of molecular clumps, there might not yet be a solid evidence for the presence of $\beta < 1$, i.e. exhibiting a flattened SED curve at longer wavelengths. We note that observations revealing a prevalent excess of 3 mm emission compared to the generic modified blackbody model have been reported (e.g. Lowe et al. 2021), however, the origin of such a feature remains uncertain.

In Figure 10, we also compare the observed temperature profiles with the centrally heated models evaluated for $\beta = 1$ (i.e., $T = 2.70(\frac{L}{L_\odot})^{0.2} (\frac{R}{1\text{pc}})^{-0.4}$; this is based on the assumption of a dust sublimation temperature of 1.1×10^3 K in the derivation, Adams 1991, for more calculation details see their appendix), and with the simple expectation based on the Stefan-Boltzmann law, i.e. $T = 0.86(\frac{L}{L_\odot})^{0.25} (\frac{R}{1\text{pc}})^{-0.5}$. We found that these pro-

files qualitatively agree with the measurements of $T(r)$ except for G13 and G31.

From Figure 10, it is seen that the temperature profiles of G13 and G31 deviate from the form of a single power-law. Specifically, they show abrupt changes as well as elevated temperatures in the ranges of 0.1-0.3 pc and 0.1-0.5 pc radii, respectively. After we adjusted $T(r)$ (Appendix E) according to dust SED profiles, G13 shows a less prominent temperature enhancement in the center while G31 still stands out. Beltrán et al. (2018) also noted the steep temperature profile of G31 within the central 0.1 pc. Their measurement consistently falls onto the functional form we fitted (i.e. the thick purple line in Figure 10) which was based on our independent measurements of T_{rot} on the larger spatial scales.

The rapid decrement of radial temperatures observed in G31 and G13 may be explained by their density profiles of the embedded dense gas structures (i.e., $\rho_{\text{dense}}(r)$). In Figure 14, it can be seen that these two sources have the most steeply decreasing $\rho_{\text{dense}}(r)$. In addition, their central ~ 0.1 pc regions show prominent high-density plateaus. The optically thin assumption of Adams (1991) may break down in the central region of the G31 and G13. Such a higher concentration of dense gas may steepen the temperature distribution in the inner envelope according to $\propto r^{-\frac{1-q}{4-\beta}}$ (e.g. Adams & Shu 1985, Rolffs et al. 2011), where q is the power-law index of radial density profile. This is

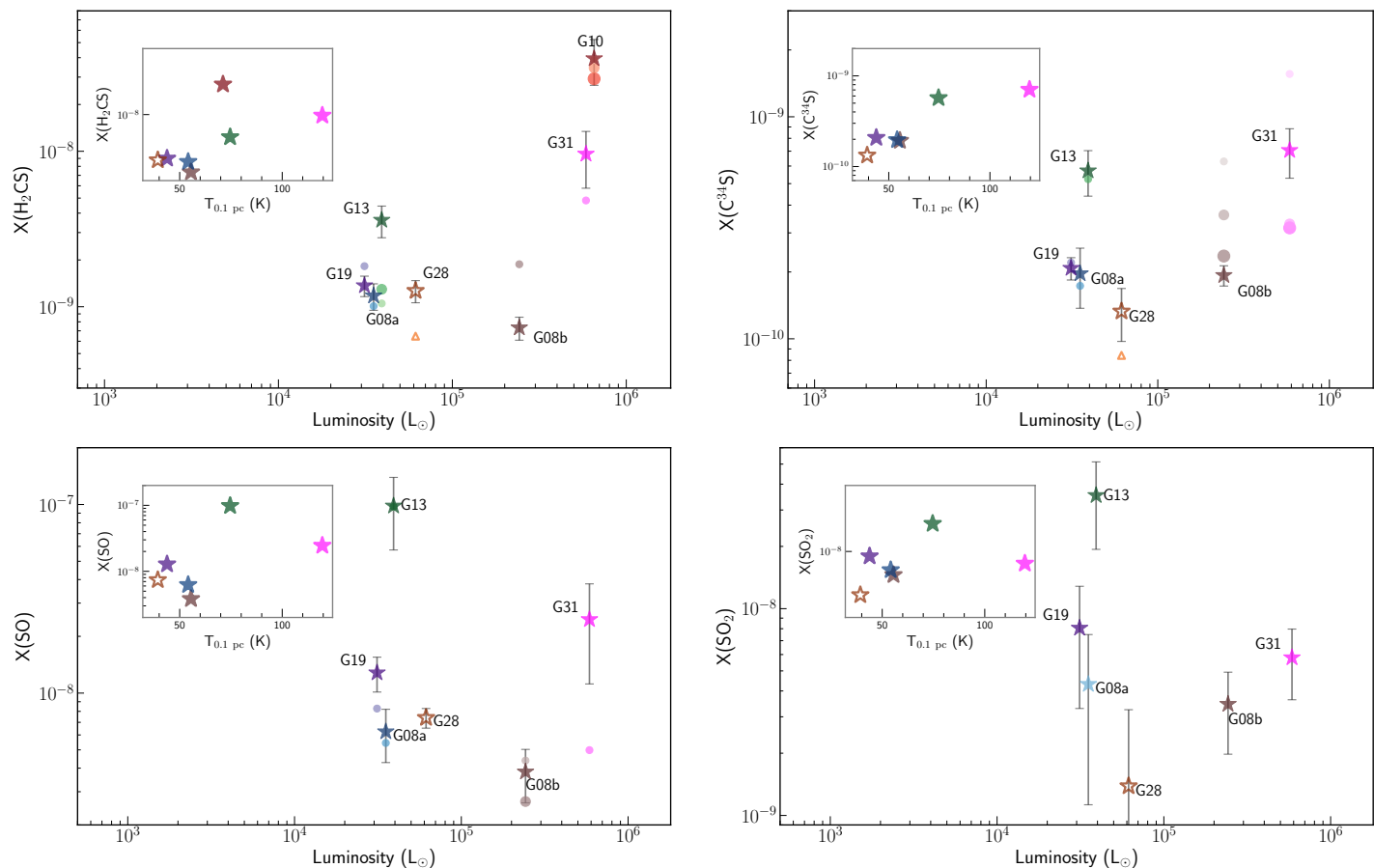


Fig. 20. Same as Figure 19, but for H_2CS , C^{34}S , SO and SO_2 .

sclosed to the diffusion approximation, which effectively means that a higher optical depth gas would mimic the lower value of β in determining the temperature structure. The presence of flattened (protostellar) disks could also induce a steeper gradient (~ 0.75) of temperature variations due to the gas heating by infall and accretion shocks (e.g. Lynden-Bell & Pringle 1974, Walch et al. 2009). Interestingly, hydrodynamic calculations of protostellar collapse demonstrate that a centrally flattened density profile results in a transitory phase of energetic accretion (Foster & Chevalier 1993, see also Henriksen et al. 1997), which may also be tentatively related to the elevated temperatures of G13 and G31.

Observations towards dense massive cores and envelopes of YSOs and discs generally find temperature slopes in the range of $\sim [-0.35, -0.7]$ (e.g. Palau et al. 2014, Beuther et al. 2007, Persson et al. 2016, Jacobsen et al. 2018, van 't Hoff et al. 2020, Gieser et al. 2021). However, the exceptionally steep temperature profile of slope steeper than -0.9 is seen at 1 000-2 000 au around massive YSO object W3IRS4 (Mottram et al. 2020), reminiscent of the result of G31 based on observations of similar spatial scales (Beltrán et al. 2018).

Strong radiative feedback has been invoked as a possible mechanism resisting over-fragmentation, which favors the formation of massive stars and can be influential in ultra dense environment (e.g. Krumholz et al. 2012). When observed with ~ 2000 au resolution, source G31 consists of two cores with one major core dominating the emission (~ 60 times flux difference at 1 mm continuum, Beltrán et al. 2018). The elevated temperature in the inner 0.1 pc might have suppressed the fragmentation of the envelope structure of the main core, leaving with only

one satellite core surrounding it. The highly concentrated dense gas structure of G13 traced by methanol lines (Figure 11) that does not extend further beyond its continuum emission (except to the west direction) may also indicate a featureless fragmentation; high resolution ($1''$) MIR imaging by Varricatt et al. (2018) reveal a binary system, although the mass contrast between the two YSO objects embedded is not as drastic as that of G31.

4.2. Density structure evolution: comparison with theoretical predictions

Figure 11 shows the $n(\text{H}_2)$ maps which were derived based on the RADEX modeling for the CH_3OH lines (Section 3.5). In general, $n(\text{H}_2)$ decreases radially with respect to the continuum center, although some sources appear notably asymmetric and present localised over-densities at large radii. We use single power-law forms (Equation 4) with parameters listed in Table 5, to describe the radial change of $n(\text{H}_2)$ maps. Comparing the observed profile to the fitted single power-law form (Figure 14), it can be seen that there are higher density plateaus at the centers of G13 and G31, such that these two sources are better described by piece-wise power-law including a central density profile of slope ~ 0 . Source G10 harbors even more dense gas at >0.1 pc radii as compared to its best-fit single power-law model, which is due to the highly flattened dense gas geometry of an edge-on rotational disk as revealed by gas kinematics (Liu 2017). In fact, for G10, the slope of dense gas profile q_{dense} is an average from two distributions: a geometrically flattened, high-density pseudo-disk with a slope shallower than -0.5 , and an envelope of which the gas density decreases sharply (Figure 11). Clumps

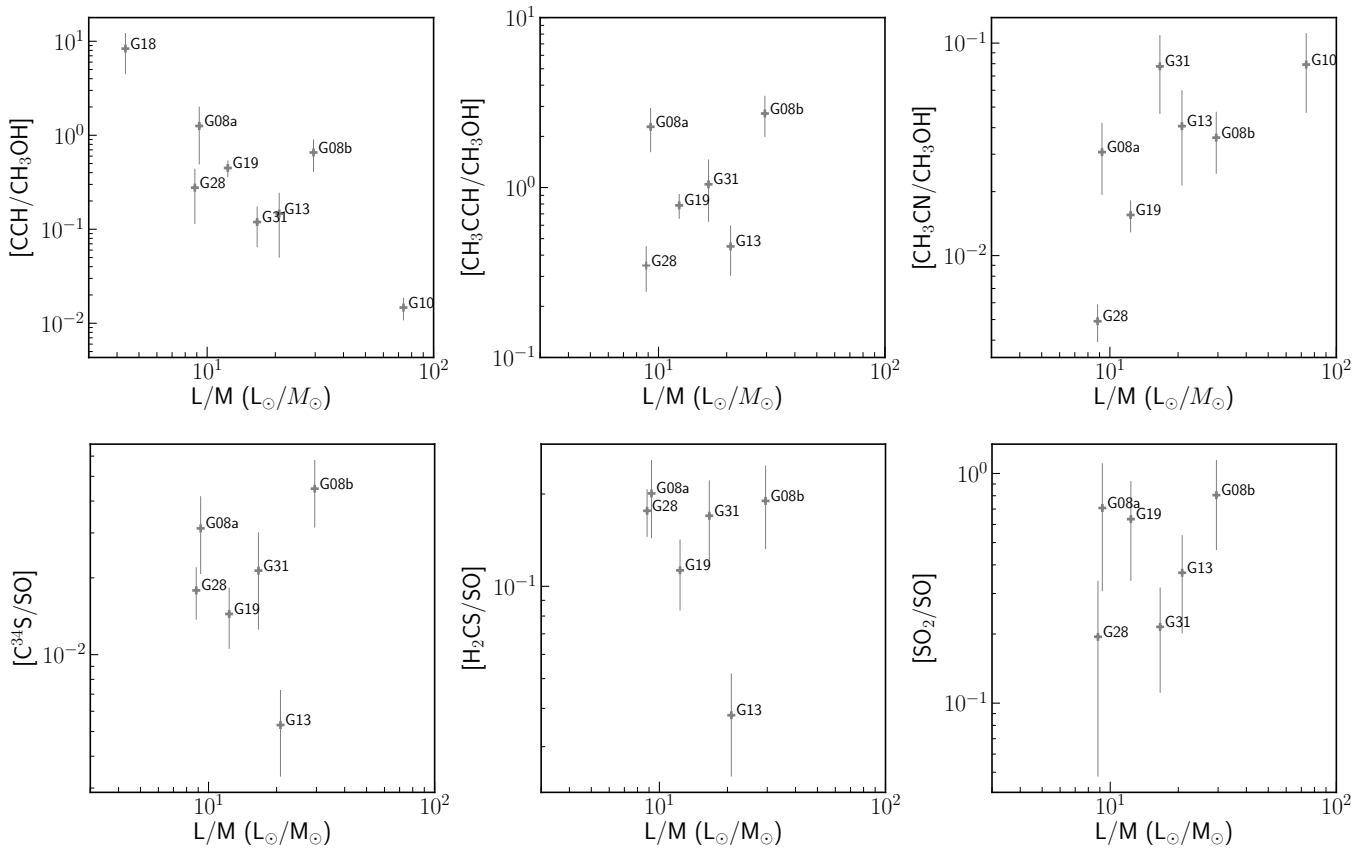


Fig. 21. *Top:* Abundance ratios of carbon-chain molecules; *Bottom:* Abundance ratios of sulfur-bearing molecules at clump center (0.1-0.15 pc, beam averaged), shown against source L/M ratios.

G28, G19 and G08a may also harbor high-density plateaus at the centers although they are not as significantly resolved as those in G10, G13 and G31.

We emphasize that the two set of power-law density slopes derived reflect clump gas in different density regimes: from single-dish continuum the slope represents density distribution of *averaged* (mass-weighted) bulk gas ($\bar{\rho} \sim 10^{4.5} \text{ cm}^{-3}$) where the spherical symmetry might be a rather good approximation of source geometry, while the slope deduced from methanol emission is reflecting the truncated central dense gas portion ($\rho \geq 10^{6.5} \text{ cm}^{-3}$) with an extension of 0.1-0.5 pc. This dense gas structure is likely highly fragmented and of reduced dimension due to the dominant role of self-gravity at progressively smaller scales and denser regimes.

Figure 18 reveals the evolutionary trend of the radial density profiles of bulk gas and dense gas structures of the target massive clumps. Our results indicate that in the initial stage of massive clump evolution, gas may be less concentrated than the singular isothermal sphere (SIS, Shu 1977), and even the logatropic model (McLaughlin & Pudritz 1997). Observations towards low-mass cores at early stages have generally found density profiles with a central plateau (e.g. Ward-Thompson et al. 1999, Bacmann et al. 2002). This density structure implies low pressure gradients at small radii, and hence in quasi-static models additional support of magnetic fields is required. The magnetic field and subsequent ambipolar diffusion may explain the existence and evolution of the shallower radial density profile of the gas, which is at an initial stage of equilibrium (e.g. Mouschovias & Morton 1991). Alternatively, in an isothermal state, the incoherently converging compression wave of shocks propagating

outside-in can also disrupt the centrally peaked density profile (Whitworth et al. 1996). Finally, hydrostatic models of a self-gravitating gas externally heated (e.g. Falgarone & Puget 1985) can also result in a similar density configuration. On the other hand, we can not rule out the possibility that the shallower density profiles are reflecting the underlying fragmentation that is distributed widely within the clump, and that the fragments do not show significant mass segregation (Sanhueza et al. 2019). Their imprints would result in a rather uniform density profile for the clumps.

Following definitions in Section 3.6, we denote the power-law slopes for the radial gas density of bulk gas and dense gas as q_{bulk} and q_{dense} . In G18 and G28, both q_{bulk} and q_{dense} are shallower than -1 (Figure 17). This may be due to a combination of the heated gas profiles and a higher level of turbulence, which effectively slow down gravitational collapse at early stage (Figure 22; more in Section 4.3). Although these two sources have $L/M \lesssim 10$, and are classified to be younger than or just reaching the ZAMS phase (Molinari et al. 2008, Giannetti et al. 2017), it is possible that the enhanced energy release of accretion associated with the massive star formation already introduces an observable temperature gradient (Figure 10).

The more evolved source G08a has a slightly shallower overall distribution of gas ($q_{\text{bulk}} \sim -1.2$) than its dense gas component ($q_{\text{dense}} \sim -1.3$), although the difference is within the errors. Interestingly, source G19 displays an opposite relation between the two slopes ($q_{\text{bulk}} \sim -1.4$, $q_{\text{dense}} \sim -0.6$; Figure 18). Comparing the virial state of these two sources (Figure 22), it seems G19 is close to a global state of energy balance while G08a has excessive kinetic energy in the central 0.2 pc, possibly caused by en-

ergy transfer and induced motions from gravitational collapse (more in Section 4.3). If a steeper density profile corresponds to a more dominant role of gravitational collapse, then the kinematic differences inferred from line-widths are compatible with the relation between density slopes in local (dense gas regime) and global (bulk gas regime) scales for these two sources. We discuss this in more detail in Section 4.5.

The overall trend seen in the right panel of Figure 17 can be qualitatively explained by the growing role of self-gravity in the evolution of gas dynamics in massive clumps (Lee et al. 2015, Gómez et al. 2021). This is illustrated in hydrodynamic simulations of star-forming clouds with continuously driven turbulence (Lee et al. 2015) that shows self-gravity plays the dominant role for all changes that happen with density structures over the scales up to >0.1 pc. Their results reveal that the power-law slopes around density peaks change from -1.3 to -1.55 before and after onset of star-formation, of 0.75 and 1.25 times global free-fall timescale (t_{ff}). By separating the scales based on dominant mass contributor of gas or (forming) stars, Murray et al. (2017) demonstrate that close to the (proto)stars the gas density profile has a slope of -1.5 (an attractor solution, see also Coughlin 2017) and in the outer envelope the slope ranges from -1.6 to -1.8. These values are in quantitative agreement with the evolved sources in our sample. The three sources having bulk gas density slopes shallower than -1 (left panel of Figure 18) may reflect an initial condition close to a constant-density core when gravitational collapse has not significantly altered the gas density profile, for both the bulk gas and dense gas structures (G18 and G28) or only the dense gas component (G19). The tendency of an initial flat inner density profile remaining flat over one t_{ff} determined by the gas central density is also discussed in Henriksen et al. (1997), which is attributed to the fact that the cloud center has the fastest growing velocity mode. The timescale is fleetingly short without further support of turbulence.

4.3. The kinematic state of clumps: radial profiles of molecular line-width and virial parameter

Based on the calculations in Section 3.8, Figure 22 shows the radial profiles of the molecular linewidths ($\Delta V = 2.355 \sigma_v$) for individual species. We fitted a power-law to the radial linewidth profiles traced by thermometer lines (i.e. excluding the data points from C^{34}S and H^{13}CO^+). In G08a, G31 and G13, the linewidth traced by these lines decrease radially with power-law indices of -0.40, -0.31, -0.56, respectively. Except for the sources G18 and G19, the linewidths on the extended regions traced by C^{34}S , H^{13}CO^+ are systematically larger than that traced by the thermometer lines. Again, for clump G18, we had to rely on pointed observations from IRAM 30m telescope to tentatively mark the radii of the linewidths obtained from thermometer lines, based on a fixed temperature profile (Sect. 3.4). We therefore note that the analysis for this clump is not based on the same, spatially resolved measurement as the other clumps.

In general, the variation in line widths does not seem to follow a monolithic radial change, as opposed to the $\sigma_v \propto r^{1/2}$ universal law observed in giant molecular clouds and low-mass cores (i.e., Larson's first law; Larson 1981). This is in agreement with the results presented in Izquierdo et al. (2021, Figure 7), where they show that the linewidth-size relationship is not uniform but rather depends on the analysed spatial scale and the physical processes taking place there (see also Hacar et al. 2016).

In high-mass star-forming regions, the observed line-widths are systematically larger, and σ_v may have a shallower power-law relation with scales (e.g. Plume et al. 1997, Caselli & Myers

1995). In addition, the virial equilibrium naturally infers that σ_v has a dependence on gas surface density, such that $\sigma_v \propto (\Sigma R)^{0.5}$ (Heyer et al. 2009).

Moreover, recent 1D simulations incorporating gravitation-driven turbulence (i.e., adiabatic heating; c.f., Robertson & Goldreich 2012) found distinct relations between σ_v and spatial scales for star-forming clumps, due to the change of the dominant turbulent driving mechanism from inner to outer regions (Murray & Chang 2015). It has been found that $v_T \propto r^{-0.5}$ holds within the sphere enclosed by the stellar influence radius, which is defined as the radius where the enclosed gas mass is comparable (e.g., 1-3 times) to the stellar mass (Murray & Chang 2015, Murray et al. 2017; see also Coughlin 2017, Xu & Lazarian 2020 for the analytic derivations).

As a rough estimate of the stellar influence radius, assuming the L_{bol} of each source is contributed solely from the luminosity of a single ZAMS star, adopting the stellar evolution model of Choi et al. (2016), the stellar mass M_* are estimated to be $12M_{\odot}$ for G19, $15\text{-}16M_{\odot}$ for G08a, G13 and G28, $30M_{\odot}$ for G08b. Grave & Kumar (2009) fit radiative transfer accretion models of YSO to source G19 and G13 by building SED from near-infrared to submm, and their derived stellar masses are consistent with our rough estimates. For G10, previous observations suggest a stellar mass of $\sim 200M_{\odot}$ (Baobab Liu et al. 2010). We note that inferring stellar mass from luminosity assuming the sole contribution from a single star leads to a lower limit, as these clumps are forming a cluster of stars following the IMF. With the same total bolometric luminosity, this corresponds to a higher total stellar mass. Comparing with the central core masses we derived from 1.2mm continuum (Table 2), it seems we marginally resolved the influence radius (about half beam FWHM) for sources G13, G08a and G10, but a bit further in the case of G08b. This may partially explain why in the inner region of G08b the observed linewidths do not decrease rapidly with radius. In G10, the observed linewidths have shallower variations with radius. This may be due to the presence of the ~ 0.2 pc scale edge-on rotational disc (Liu 2017), towards which gas settles into coherent rather than random motions.

For the early-stage clumps G18, G19, and G28, the bolometric luminosity is likely dominated by accretion energy. This leads to an overestimate of the stellar mass, such that in reality there appears to be a more drastic difference between the embedded stellar mass and the gas mass at the scale probed, than our rough estimates. Therefore, it is likely that we do not see the decreasing trend of linewidths with radius in their inner regions due to the too coarse resolution to resolve the stellar influence radius. In addition, assuming turbulent velocity scales as the local infall velocity, Coughlin (2017) demonstrates that there is temporal steepening of the radial profile of the rms velocities, due to gravitational field starting to dominate the dynamics of inflowing gas, which changes from $v_T \propto r^{-0.2}$ to $v_T \propto r^{-0.5}$. Hence, it may also be that early-stage clumps have a shallower inner slope that tend to flatten out, further smeared in coarser resolution measurements.

Exterior to the stellar influence radius, simulations found that $v_T \propto r^{0.2}$ (see also Lee et al. 2015). Compared to classical subsonic turbulence following Kolmogorov law ($v_T \propto r^{1/3}$) or supersonic turbulence ($v_T \propto r^{1/2}$), the shallower scaling relation between linewidth and spatial scale of the region beyond stellar influence radius, could be due to additional energy converted from (part of) gravitational collapse (Ballesteros-Paredes et al. 2011, Xu & Lazarian 2020) and/or kinetic energy of extended inflow gas transported by radial motions (Padoan et al. 2020). Klessen & Hennebelle (2010) demonstrate that the conversion efficiency

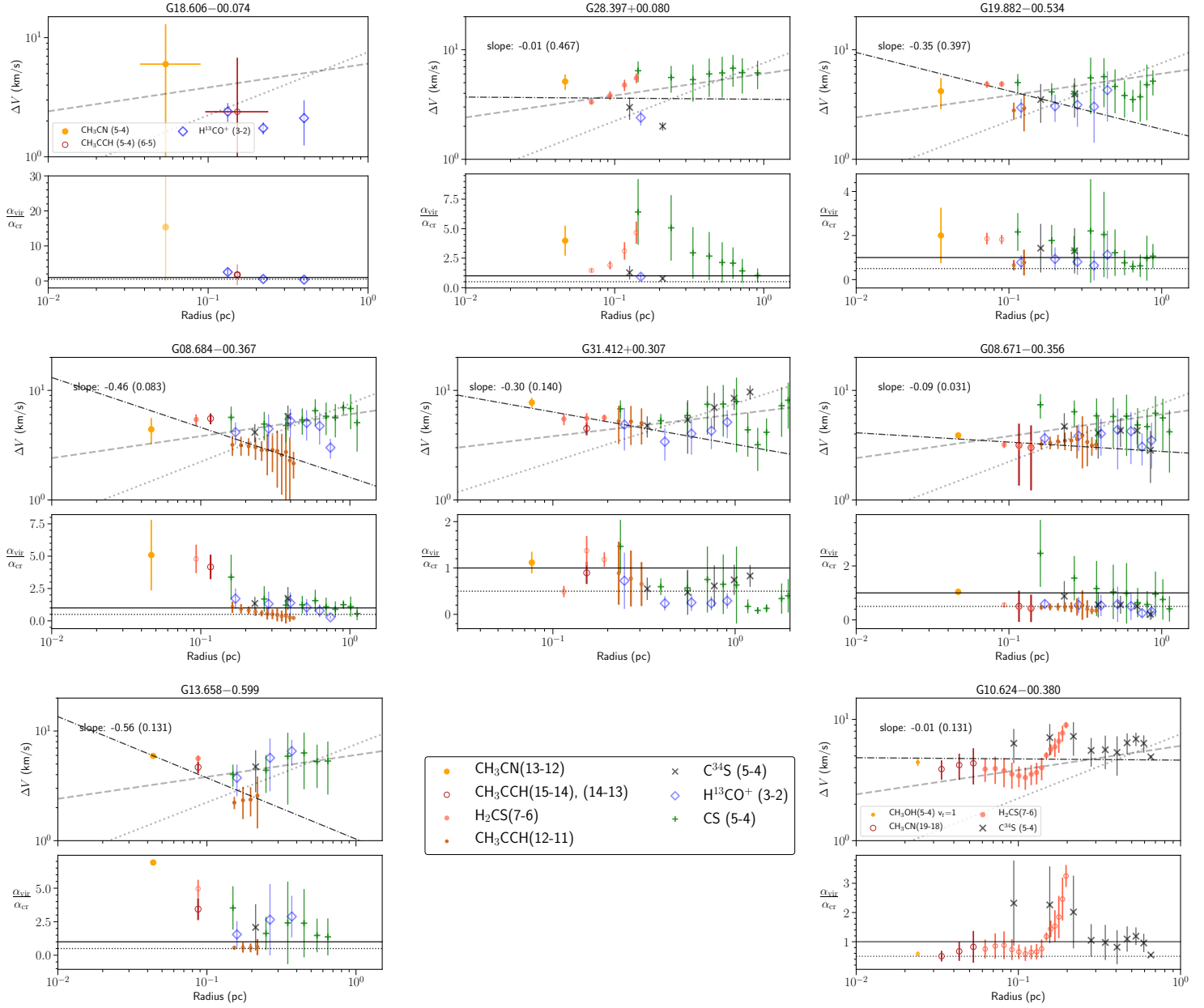


Fig. 22. Derived averaged radial linewidth and virial parameter profiles. Dashed dotted line in each upper panel indicates the power-law fit to the linewidths from thermometer lines. In each upper panel, gray dotted line indicates relation found by Caselli & Myers (1995) of Orion low-mass cores scaled up by a factor 5, which roughly matches the observed linewidth in our case, of $\Delta v/1 \text{ km s}^{-1} = 7.5 (\tau/1 \text{ pc})^{0.53}$; Gray dashed line shows a relation of $\Delta v/1 \text{ km s}^{-1} = 6.0 (\tau/1 \text{ pc})^{0.2}$. These two reference lines are identical in all plots. In each lower panel, the ratio between α_{vir} to critical virial parameter α_{cr} is shown; horizontal solid line and dotted line indicate ratio 1 (equipartition) and 0.5 (virial equilibrium), respectively. All plots except for G10 and G18 share the same legend shown in the middle panel of the last row, in which the color coding for the thermometer lines is the same as in Figure 10.

to internal turbulence depends on the density contrast between the accreting entity and the inflowing gas. These may explain why in the outer regions of G08a, G08b, G13 and G10, the observed linewidths rise with radius, having a power-law slope of $\geq 0.2-0.3$.

In light of the radial profiles of α_{vir} , it appears that our target clumps can be classified into three types, based on their $\alpha_{\text{vir}}/\alpha_{\text{cr}}$ ratios: sources G08b, G31 and G10 are in an overall virial to sub-virial state; G18, G08a and G13 show super-virial states in the centre and sub-virial states in outer envelope; G28 and G19 have uniform α_{vir} fluctuating mostly above α_{cr} (see the detailed description in Table 8). To explain the observed super-virial states

in the central regions of some of these clumps, it is required to introduce other line-broadening mechanisms.

The three sources that have large virial parameters in the centers have the lowest central core masses and densities (Table 2). If central cores are treated as a decoupled structure from the clump envelope, the more massive and denser cores being more sub-virial is consistent with previous observations towards massive star-forming regions (e.g. Kauffmann et al. 2013, Liu et al. 2015, Traficante et al. 2018). However, due to the insufficient angular resolution, the estimate of α_{vir} in the clump center may suffer from larger uncertainties, e.g. there is possibly higher level of clumpiness with complex velocity structures that confuse the

Table 8. Properties related to radial linewidth and virial parameter profiles of the target clumps.

Source	M_{\star}^a (M_{\odot})	Slope ^b	$\Delta V_{0.1\text{pc}}^b$ (km/s)	Radial variations of $\alpha_{\text{vir}}/\alpha_{\text{cr}}$
G18 ^c	11	-	-	>10 in center (<0.1 pc) and ~1-2 at outer envelope (>0.1 pc)
G28	23	-0.01(0.48)	3.6(0.6)	fluctuate at ~0.5-5 at all radii
G19	18	-0.35(0.40)	4.2(0.5)	fluctuate at ~0.5-5 at all radii
G08a	17	-0.46(0.08)	4.6(0.3)	>2 in center (<0.2 pc) and ~0.5-2 at outer envelope (>0.2 pc)
G31	64	-0.30(0.14)	6.3(0.4)	~1 in center (<0.1 pc) and ~0.5-1 at outer envelope (>0.1 pc)
G08b	26	-0.09(0.03)	3.3(0.1)	$\lesssim 1$ at all radii
G13	19	-0.56(0.13)	3.7(0.4)	>2 in center (<0.1 pc) and ~1-2 at outer envelope (>0.2 pc)
G10	68	-0.01(0.13)	4.7(0.4)	~0.5 in center (<0.1 pc) and ~1-2 at outer envelope (>0.1 pc)

^a: Estimated (single) stellar mass based on interpolating the ZAMS models of Choi et al. (2016), from the clump L_{bol} listed in Table 6.

^b: Fitted slope and linewidth amplitude at 0.1 pc (and errors) of the linewidth radial profile in the inner region. The fitted relation is indicated as the dashed dotted line in the upper panel of Figure 22.

linewidth measurement. In addition, the α_{vir} in the centermost is derived from linewidth of CH_3CN . CH_3CN has been shown to trace the interface of convergent flows in high-mass clumps (Csengeri et al. 2011), which is also enhanced in shocks (Bell et al. 2014) and associated with hot accretion flows (Liu et al. 2015).

Camacho et al. (2016) and Ballesteros-Paredes et al. (2018)) have shown that the observed high α_{vir} may not be indicative of pressure confining or gas dispersal. Alternatively, for low column density clumps this picture might be due to highly dynamic externally driven gas accumulation. For high column density clumps it might be a result of neglecting the stellar mass or accreting materials outside the cores in contributing to the gravitational energy. The latter may qualitatively explain the super-virial state in the center of the three sources G18, G08a and G13, which does not necessarily indicate a halt of collapse. On the other hand, the inclusion of infall velocities to the observed linewidth may also cause the source which is undergoing collapse to appear seemingly unbound (e.g. Smith et al. 2009). Infall motions of dense cores that have large $\alpha_{\text{vir}} \sim 5-8$ are revealed by Cesaroni et al. (2019), inside a massive cluster-forming clump.

Giannetti et al. (2017) suggest that CH_3CCH is a reliable tracer for the kinematics of bulk gas structures in the massive clumps. From the α_{vir} derived based on the CH_3CCH lines, it appears that all clumps are in sub-virial or virial status. But at smaller scales in the central region of the clumps, the gas can appear super-virial. Aside from the three clumps showing large α_{vir} in the center, other clumps show an evolution of globally (for all radii) decreasing α_{vir} with increasing L/M . Ballesteros-Paredes et al. (2018) and Camacho et al. (2020) investigated the evolution of α_{vir} in molecular clouds based on numerical simulations. They showed that the gas structures may be initially assembled due to the large-scale turbulence. Afterwards, the assembled gas structures evolve from over-virial to sub-virial status, and finally approach energy equipartition, or further become super-virial after one t_{ff} due to gas expulsion. Our observations do not show such non-monolithic evolution of α_{vir} with L/M . This is likely because all target clumps remain in early to intermediate evolutionary stages, which are prior to or in the stage of active star formation and the gas mass dominates the mass budget preceding the gas dispersal stage.

4.4. Comparison with chemical models: carbon-chain molecules and sulfur-bearing species

The formation pathways of molecules and chemical rates are tightly influenced by gas temperature and volume density. In Section 3.9, we used the molecular column densities of CH_3CCH , H_2CS , CH_3CN , CH_3OH , C^{34}S , CCH , SO and SO_2 to derive the molecular abundance distributions and abundance ratios between relevant species. We discuss comparisons between these results with predictions from chemical models in this section.

4.4.1. CH_3OH , CH_3CCH , CH_3CN , and CCH

CH_3CCH is designated as a ‘cold molecule’ (Bisschop et al. 2007), since it presents low excitation temperatures compared to other complex organic molecules (COMs) such as CH_3CN and CH_3OCH_3 . The formation pathways of CH_3CCH include cold gas phase reactions and grain-surface chemistry (Calcutt et al. 2019). The reactions in gas phase involve thermal desorption which requires low temperatures. Calcutt et al. (2019) suggested that CH_3CCH is a ‘gateway’ molecule which traces the interface between hot cores/corinos and colder envelope, and extends further out in the envelope. The inset in Figure 19 shows measured CH_3CCH abundances averaged from the outer region (≥ 0.1 pc) of the clumps with the gas temperature measured at 0.3 pc. These properties represent the bulk luke-warm gas. The small variation of CH_3CCH abundance across our sample indicates that it is not a sensitive molecule to trace the ≥ 100 K thermal desorption of hot core regions. Its emission rather traces the more extended gas and is a good kinematic tracer for >0.1 pc gas structures within massive clumps (e.g. Giannetti et al. 2017). There is also not drastic radial change of the abundances of the other two COMs CH_3OH and CH_3CN for individual sources (Figure 19). This is expected since our angular resolution is not sufficiently high to reveal the >100 K region (confined within 0.1 pc) where prominent abundance enhancement of COMs is expected (Garrod et al. 2017).

The abundance profiles of CCH exhibit an increase towards the outer clump envelope for most the sources in the sample (Figure 19) and an overall decrease of abundance with clump luminosity. These results reflect that CCH is abundant at an early stage and then transformed to other molecules in the clump center (Beuther et al. 2002a). The abundance of CCH in outer regions is maintained by reproduction of CO dissociated by an ex-

ternal UV field. Similarly, in early-stage low-mass cores, CCH is also tracing more quiescent gas, e.g. the outer part of a circumbinary envelope (van Dishoeck et al. 1995).

We compare the abundance ratios between CCH, CH₃CN and CH₃CCH with CH₃OH in Figure 21. In low-mass star-forming cores, the ratio of [CCH]/[CH₃OH] is usually used to distinguish less evolved warm carbon-chain cores with hot corinos (e.g. Graninger et al. 2016). The strong anti-correlation of [CCH]/[CH₃OH] with L/M indicates that in the central region of massive clumps this ratio serves well as an evolutionary indicator. [CH₃CN]/[CH₃OH] has a tight correlation with L/M as well: except the hot massive core G31, the other sources show a clear monotonic increase of [CH₃CN]/[CH₃OH] with increasing L/M . This is consistent with the formation timescale of the two species: CH₃OH forms at early stages (10 K) on grain surfaces, primarily via successive hydrogenation of CO (e.g. Watanabe et al. 2003), while the formation of CH₃CN appears late, through radiative association between HCN and CH₃⁺ on grain surface as well as CH₃ with CN in gas phase (Nomura & Millar 2004).

4.4.2. Sulfur-bearing molecules

Time-dependent theoretical chemical models of sulfur-bearing species find that the evaporation of H₂S and subsequent chemical reactions in hot cores lead to an increasing abundance ratio of SO₂/SO (Wakelam et al. 2011, Esplugues et al. 2014). At a late stage of hot core evolution, H₂CS and CS are also drastically enhanced; together with SO₂, they become the most abundant sulphur-bearing species. In shocked regions, similar trends along evolution are predicted (Wakelam et al. 2005, Esplugues et al. 2014). But observations seem to suggest opposite variations of X(CS)/X(SO) with source evolutionary stages (Li et al. 2015, Gerner et al. 2014, Herpin et al. 2009). Assuming same ³⁴S/S isotopic ratio for our target clumps, we find a similar result which is reflected by the feature in Figure 21 (left panel, bottom row). Similar results of X(H₂CS)/X(SO) and X(SO₂)/X(SO) with clump L/M are derived in Figure 21 (middle and right panel, bottom row): there are no prominent correlations found. We note that the temporal evolution of abundance of sulfur-bearing species is highly dependent on the source physical structure (Wakelam et al. 2005, Wakelam et al. 2011), which require tailored chemical modeling for individual source to disentangle this impact and the evolutionary time.

4.5. Density structure: relation with cloud structure and implications for different dense gas conversions

In this section, we discuss how the radial density profiles of massive clumps (see Section 4.2) may be linked to statistics of parental cloud structures on large scales (≥ 10 pc). We also elaborate on the physical implications of the radial density profiles comparisons between bulk gas and dense gas structures, ρ_{bulk} and ρ_{dense} .

Gravoturbulence simulations of molecular clouds (e.g., Kritsuk et al. 2011, Lee et al. 2015) showed that the cloud volume density probability distribution functions (ρ -PDF, p_s) have lognormal and power-law forms in the low- and high-density regimes, respectively. The lognormal form is attributed to the primordial and maintained supersonic turbulence, while the power-law tail is usually regarded as a sign of gravitational collapse. Thus, the study of PDF statistics is a useful method to understand the physical mechanisms at play in molecular clouds. Gravitational contraction converts a fraction of low-density gas

to high-density structures over a timescale comparable to the free-fall timescale (t_{ff}) of the mean density. With this process, the slope of the power-law tail s changes from $s \approx -3$ to $s \approx -1.5$ – -1 (e.g. Girichidis et al. 2014, Guszejnov et al. 2018) in a mean free-fall time. When the power-law tail of the ρ -PDF is dominated by a single gravitationally bound massive clump with a $\rho(r) \propto r^q$ density profile, there is a relation $s = 3/q$ (Federrath & Klessen 2013b). In other words, q is expected to evolve from ≈ -1 to -3 – -2 over a mean t_{ff} . Observational works usually constrain the column density probability distribution function (N-PDF, p_n) rather than ρ -PDF. In this case, the power-law slope of the N-PDF (s_N) can be related to the radial density profile of the molecular clump by $\frac{2}{1+q}$. Column density mapping towards Galactic massive star forming complexes yield power-law slopes for N-PDF ranging between ~ -4 to -2 (Lin et al. 2017). The evolutionary trend of steepening density profiles (the bulk gas density profile) of the massive clumps resolved in this work is in general consistent with the prediction from cloud-scale statistics.

The cloud-scale (10 pc) dense gas fraction can be relatively well described by statistics of ρ/N -PDFs, which do not factor in features of spatial distribution. Within the ~ 1 pc scale clump structure, the spatial configuration of dense gas can be critical in determining the properties of final star clusters. We discussed the gas radial density profiles probed by dust emission and dense gas tracer (CH₃OH) separately in Section 4.2. Here we note again that dust emission is tracing *averaged* (mass-weighted) bulk gas structures ($\bar{\rho} \sim 10^{4.5} \text{ cm}^{-3}$) while CH₃OH emission probes dense gas regimes ($\rho \gtrsim 10^{6.5} \text{ cm}^{-3}$, up to several 10^8 cm^{-3}) within the massive clumps. We note that the gas density difference seen by dust and higher angular resolution CH₃OH emission can also be partially related to the coarser resolution of the single-dish continuum images, which tend to smear out the gas over-densities at smaller spatial scales. However, the major cause of the difference is that CH₃OH transitions selectively trace the higher-density gas component, while the dust emission does not critically depend on the volume density of the gas (in the regimes we are interested in), providing a measure of bulk gas properties. By relying on two density probes for different gas density regimes, we go beyond the self-similar solution of gravitational collapse by characterising the density configuration of massive clumps with two “layers” ρ_{bulk} and ρ_{dense} , each of which is described by a power-law form. The ρ_{dense} traced by CH₃OH from RADEX modeling (Section 3.5) is verified by full radiative transfer non-LTE models described in Appendix F, by introducing a volume filling factor ff_{dens} (Table 7) to spherical models. The low volume filling factor indicates that the dense gas is highly clumpy and organised into filament- or sheet-like structures, which is a natural outcome of supersonic turbulence and gravitational collapse (Smith et al. 2020). In general there seems to be a higher density contrast (decreasing ff_{dens}) with increasing L/M (as listed sequentially in Table 7, last column). While ff_{dens} provides an upper limit of the volume filling factor of high-density gas, we will make here some inferences for the dense gas mass fraction based on intuitive assumptions and references to numerical simulations. The aim is to establish the ratio of the bulk gas and dense gas density profiles, $\rho_{\text{bulk}}/\rho_{\text{dense}}$, as a measure of the dense gas fraction, and the radial profile of this ratio as an indicator of different star formation modes (or temporal variations of the SFE) for the massive clumps.

It is a well-known fact that there is a strong correlation between SFR and dense gas. Based on a gravo-turbulent fragmentation scenario, Padoan et al. (2012, 2017) derived an empirical relation between SFR per free-fall time ϵ_{ff} (the fraction of a cloud’s mass that is converted to stellar mass over a free-fall

time scale, Krumholz & McKee 2005) and α_{vir} ,

$$\epsilon_{\text{ff}} = \dot{M}/(M/t_{\text{ff}}) \propto \exp(-\alpha_{\text{vir}}^{1/2}) \quad (8)$$

In a hierarchical description of cloud structure in which gas density increases with decreasing scale, the conservation of \dot{M} (or equivalently SFR) translates into

$$\epsilon_{\text{ff},1} M_{1,\text{tot}}/t_{\text{ff},\rho_1} = \epsilon_{\text{ff},2} M_{2,\text{tot}}/t_{\text{ff},\rho_2} \quad (9)$$

in which the number indices of 1 and 2 denote two adjacent levels in a hierarchy. We assume ρ_{bulk} represents the gas density of a lower-level structure in the hierarchy from which a higher level structure of gas density ρ_{dense} originates from. We further assume that only the dense gas ρ_{dense} participates in the star formation process. Then with a scale-invariant ϵ_{ff} (or equivalently scale-invariant α_{vir}), Equation 9 translates to $M_{\text{dense}} = M_{\text{tot}}(t_{\text{ff},\rho_{\text{dense}}}/t_{\text{ff},\rho_{\text{bulk}}})$. Substituting the free-fall timescale $t_{\text{ff}} \propto \rho^{-1/2}$ into the equation, we obtain,

$$M_{\text{dense}} \sim M_{\text{tot}} \left(\frac{\rho_{\text{bulk}}}{\rho_{\text{dense}}} \right)^{1/2}. \quad (10)$$

Naively, this relation means that at a certain scale, the closer the derived dense gas density is to the bulk gas density, the more mass fraction of the clump is occupied by the dense gas. We note that even without the assumption of scale-invariant ϵ_{ff} , considering only that the two set of densities are each the mass-weighted value in their respective density regimes, the mass fraction of dense gas to total clump gas is also largely determined by $\rho_{\text{bulk}}/\rho_{\text{dense}}$, when the ratio between density of bulk gas and gas not seen by CH₃OH is similar among sources and does not vary with scale.

Figure 23 shows the density profiles ρ_{dense} and ρ_{bulk} . This figure also shows the ratios between these two profiles, which provide a measure of dense gas mass fraction (DGMF), i.e. $M_{\text{dense}}/M_{\text{tot}}$. We found that the DGMF in G19, G08b, and G10 decrease with radius, while it increases with radius in G28, G08a, G13 and G31. For G31, since the optical depths of the CH₃OH lines are high such that the line ratios do not serve as good as a densitometer in the density regimes it associates as the other sources, we omitted discussion on this source while note that the clump indeed holds the highest dense gas densities seen by CH₃OH, among all target sources. Among the other six sources, specifically, G19 shows an decreasing DGMF from 25% to 19%, G08b from 22% to 18% and G10 from 24% to 15%. For G28, DGMF increases from 15% to ~17% at 0.1-0.2 pc. In G08a and G13, DGMF is ~19% at their centers and achieve ~22% at 0.2-0.3 pc radii.

Given these radial variations of DGMF, it might be indicative that among these 6 sources, G19 and G10 may be most efficiently converting gas into the dense gas regime, having a focused DGMF towards clump center. G08b exhibits a similarly high DGMF that changes slightly with scale, while early-phase clump G08a and the least massive G13 have DGMF peaking around the intermediate scales relative to the center. Another early-stage source G28 has the least DGMF overall and also shows an relatively invariant DGMF over scales. This trend is only partially reflected in the density profiles slopes of $\rho_{\text{bulk}}(r)$, which is generally regarded as a measure of dense gas concentration that directly inflates the SFR (e.g. Parmentier 2019). It is noteworthy that radial variations of the DGMF for individual sources is compatible with the radial dependence of the virial parameter shown in Section 4.3 (Figure 22). These two measures are both indicative of the capability of the source

in converting gas into the denser regime at different positions relative to the bottom of the clump's gravitational potential. It is straightforward to see that the three classes of increasing/flattened/decreasing DGMF as a function of radius, for a particular source, correspond to a shallower/similar/steepier dense gas profile (q_{dense}) compared to that of its bulk gas (q_{bulk}) on the basis of Eq. 2, 4 and 10. In the non-homologously spherical collapse framework, the physical condition of an outer shell can be regarded as an earlier stage preceding the inner shell (e.g. Vázquez-Semadeni et al. 2019), then a radially-decreasing (increasing) DGMF corresponds to an accelerating (retarding) dense gas conversion and temporal increase (decrease) of SFE for a particular source.

The localised behavior of dense gas conversion may be causing the chaotic and scattered SFR vs. gas density relation, and such behavior goes beyond the self-similar solutions for collapsing clumps. The non-self-similar behavior is suggested to be relevant even for the spherical collapse as shown theoretically by Coughlin (2017), dependent on the initial conditions. The spatial variations of the DGMF may also reflect two competing gravitational collapses within these massive clumps: collapse towards the global potential center, and collapse of dense regions into ambient filaments, and the latter process is mostly induced by turbulence (Girichidis et al. 2011). The dominance of one or another process depends on the initial density profile and turbulence driving modes (Girichidis et al. 2011, Lomax et al. 2015).

We can also establish $\rho_{\text{bulk}}/\rho_{\text{dense}}$ as a measure of DGMF from another perspective, with a less strong assumption. In the framework of turbulent convergent flows, the gas density enhancement after a compressive shock has an inverse length scale relation following,

$$\rho_{\text{post}}/\rho_0 \propto L_0/l_{\text{post}} \sim M_s^2 \quad (11)$$

in which L_0 and l_{post} denote the length scales of the pre-shock and post-shock gas, and ρ_0 and ρ_{post} the gas densities, respectively. M_s denotes the sonic Mach number, $M_s = \frac{\sigma_{\text{rms}}}{c_s}$. This shock jump condition is at the origin of the lognormal distribution of PDF. As Equation 11 links the gas length scale to density with an inverse relation, then the mass ratio of post-shock dense gas versus the pre-shock gas, may also be represented by a power-law form following $(\rho_0/\rho_{\text{post}})^{-s}$ with slope s dependent on the assumed geometry. With a cylindrical geometry describing infinite filaments, the gas mass is $\propto \rho l^2$ with l denotes thickness (radius), with slope $s = 1$.

If the enhancement of gas density (ρ_{dense}) as traced by CH₃OH is regarded as the result of compressive turbulence on the pre-shock gas that has a density represented by ρ_{bulk} , the ratio $(\rho_0/\rho_{\text{post}})$ still holds as a DGMF measure. Compared to Eq 10 ($s = 1/2$), the different scaling of $s = 1$ does not change the general trend of the radial change of this measure, but only to increase the contrast between outer layer and inner region.

In any case, the dense gas probed by CH₃OH does have contributions from shock entrainment, as suggested by locally increased M_s and the fact that CH₃OH is likely enhanced in shocked regions. On the other hand, we have already seen in Section 4.3 that gravitational collapse has altered the general scaling relation of v_T (hence M_s), which makes the slope s vary. A more stringent comparison of radial change of dense gas mass fraction to indicate the dense gas conversion efficiency would benefit from properly separating the part of dense gas associated with transient gas substructures with virialised cores and coherent flows, which is achievable with finer (both spectral and spatial) resolution observations.

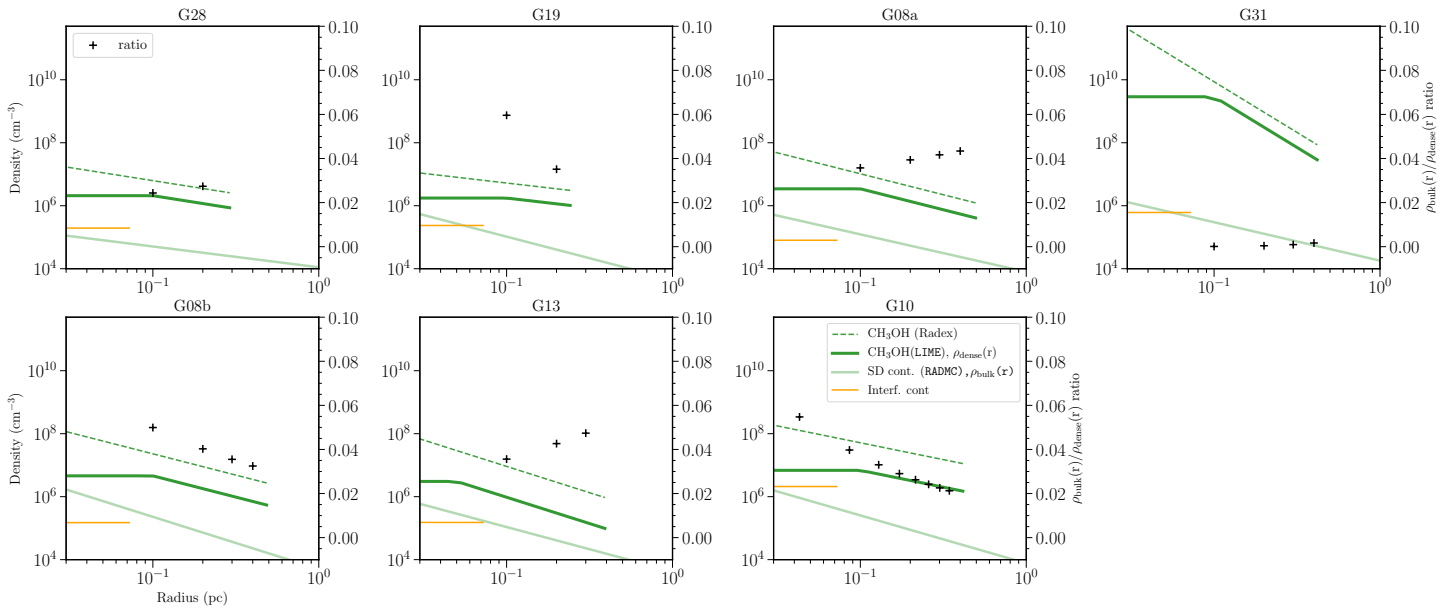


Fig. 23. Comparison between gas density profiles derived by modeling continuum and CH_3OH line emission. The ratio between densities derived by CH_3OH LIME modeling (ρ_{dense}) and continuum (ρ_{bulk}) results are shown as pluses (following right y-axis). The density estimated by SMA 1.2 mm continuum observations representing the central core average density is shown as vertical orange line in each plot (Table 2).

5. Conclusions

The gas thermal properties are critical to the star-formation process. For massive star formation, the density structure of the nursery gas clumps may not be well predicted by previous hydrostatic equilibrium core models which are generally good representative of low-mass cores, due to a higher level of turbulence and gravitational collapse set at larger scales. We conducted a SMA and APEX line survey towards a sample of eight massive star-forming clumps, in order to understand the evolution of temperature and density structures. The major findings are as follows:

1. Transitions of multiple molecular species (CH_3CN , CH_3CCH , H_2CS) of distinct critical densities, together with dust emission, provide a reasonably good sampling of different gas temperature regimes ($\gtrsim 200\text{--}20\text{ K}$) over the full clump scale. There is not a single power-law relation dependent only on source luminosity that could describe all the radial temperature variations in our sample. The elevated temperature of a less luminous source may be related to the intermittency of accretion and shock-related activities.
2. CH_3OH line series are good density probes for massive clumps, selectively tracing density regimes of $\gtrsim 10^6\text{ cm}^{-3}$. Systematic steepening of density profiles along clump evolution, indicated by L/M , is revealed among the sample, from both continuum (bulk gas) and CH_3OH line (dense gas) modeling. The density slopes change from >-1 to ~-1.5 . The dense gas proportion becomes denser with increasing L/M , and the volume filling factor of the dense gas decreases, which corresponds to a higher density contrast along clump evolution.
3. The radial line-width profile traced by multiple lines displays a scale-dependent relation. Several sources, which have comparable stellar mass and gas content at the scale probed, have a central decreasing trend of $v_T \propto r^{-0.4}$ and $v_T \propto r^{0.2}$ in the outer envelope, which may be tentatively related to conversion of gravitational energy to turbulence. On larger scales

(0.2–0.5 pc) all clumps are close to virial state ($\alpha_{\text{vir}}/\alpha_{\text{cri}} \sim 1$), as indicated by CH_3CCH , H^{13}CO^+ lines. Small scale ($\lesssim 0.1$ pc) virial parameters traced by CH_3CN and H_2CS can exceed equilibrium values for some of the sources, the origin of which is hindered by our limited resolution. Overall, we observe that the clump gas evolves from super-virial to sub-virial state with increasing L/M .

4. The abundance of CH_3OH , CH_3CN , H_2CS shows a better correlation with source central temperature than with luminosity. Abundance ratios of $[\text{CCH}]/[\text{CH}_3\text{OH}]$ and $[\text{CH}_3\text{CN}]/[\text{CH}_3\text{OH}]$ are in good correlation with clump L/M , and can be used as indicators of evolutionary stages of massive star-forming clumps.
5. The evolutionary trend of clump density profiles is compatible with cloud-scale diagnosis that frequently reveal the time-varying power-law tail of PDFs. In a hierarchical view, the radial variation of the dense gas mass fraction, which can be approximated by the density ratio between that representing the averaged bulk gas (dust continuum, no spatial filtering) and that probed by a high density tracer (CH_3OH) may be indicative of the efficiency of the source in dense gas conversion and dense gas focusing to the global gravitational center. The bulk gas density profile is a less distinct measure due to the fact that self-similar approximation is not adequately describing the clumpy gas structures within massive clumps.

In this work, we attempt to understand the role of self-gravity in shaping the gas structure as massive clumps evolve over time. Our results are based on $\lesssim 0.1$ pc observations, although a dense gas filling factor (probed by CH_3OH) indicates on smaller scales a clumpy gas environment of higher density contrast along the evolutionary track. Detailed fragmentation properties, cores and filaments and their kinematics, remain unresolved. In any case, deduction of line-of-sight cloud geometry is difficult. With the unknown cloud thickness, the mass scale of the high-density gas regime remains highly uncertain.

Existing observations have broadly revealed transonic to subsonic line-widths associated with localised substructures in massive star-forming regions, the length scale of which is well above sonic scale, indicating an efficient turbulence dissipation process. More robust velocity line-width profiles require better resolved observations to disentangle multiple velocity components, and confusion from stellar feedback (outflows), etc. In addition, while the scale-dependent line-width vs. radius relation is more indirect evidence (based on assumption that it mirrors radial infall velocity) of changing role of gravitational collapse in dominating gas dynamics, more direct evidence would be measurement of infall velocities, or accretion rates as a function of radius. The latter is indispensable to distinguish different collapse models (e.g. Padoan et al. 2020). This calls for observations of multiple “infall tracers” sensitive to different gas density regimes, along with a proper description of the temperature distribution.

Acknowledgements. This work was partly funded by the Deutsche Forschungsgemeinschaft (DFG, German Research Foundation) Collaborative Research Council 956, sub-project A6. Y.L. is a member of the International Max-Planck Research School (IMPRS) for Astronomy and Astrophysics at the Universities of Bonn and Cologne. H.B.L. is supported by the Ministry of Science and Technology (MoST) of Taiwan (Grant Nos. 108-2112-M-001-002-MY3 and 110-2112-M-001-069-). The Submillimeter Array is a joint project between the Smithsonian Astrophysical Observatory and the Academia Sinica Institute of Astronomy and Astrophysics and is funded by the Smithsonian Institution and the Academia Sinica.

References

- Adams, F. C. 1991, *ApJ*, 382, 544
 Adams, F. C. & Shu, F. H. 1985, *ApJ*, 296, 655
 Bachiller, R. & Gutiérrez, M. P. 1997, *The Astrophysical Journal*, 487, L93
 Bacmann, A., Lefloch, B., Ceccarelli, C., et al. 2002, *A&A*, 389, L6
 Ballesteros-Paredes, J., Vázquez-Semadeni, E., Gazol, A., et al. 2011, *MNRAS*, 416, 1436
 Ballesteros-Paredes, J., Vázquez-Semadeni, E., Palau, A., & Klessen, R. S. 2018, *MNRAS*, 479, 2112
 Baobab Liu, H., Ho, P. T. P., Zhang, Q., et al. 2010, *ApJ*, 722, 262
 Bate, M. R. 2009, *MNRAS*, 392, 1363
 Beckwith, S. V. W. & Sargent, A. I. 1991, *ApJ*, 381, 250
 Bell, T. A., Cernicharo, J., Viti, S., et al. 2014, *A&A*, 564, A114
 Belloche, A., Meshcheryakov, A. A., Garrod, R. T., et al. 2017, *A&A*, 601, A49
 Beltrán, M. T., Cesaroni, R., Neri, R., et al. 2004, *ApJ*, 601, L187
 Beltrán, M. T., Cesaroni, R., Rivilla, V. M., et al. 2018, *A&A*, 615, A141
 Bergin, E. A., Goldsmith, P. F., Snell, R. L., & Ungerechts, H. 1994, *ApJ*, 431, 674
 Bertoldi, F. & McKee, C. F. 1992, *ApJ*, 395, 140
 Beuther, H., Henning, T., Linz, H., et al. 2010, *A&A*, 518, L78
 Beuther, H., Leurini, S., Schilke, P., et al. 2007, *A&A*, 466, 1065
 Beuther, H., Ragan, S. E., Johnston, K., et al. 2015, *A&A*, 584, A67
 Beuther, H., Schilke, P., Menten, K. M., et al. 2002a, *ApJ*, 566, 945
 Beuther, H., Schilke, P., Menten, K. M., et al. 2002b, *ApJ*, 566, 945
 Beuther, H., Semenov, D., Henning, T., & Linz, H. 2008, *ApJ*, 675, L33
 Binder, B. A. & Povich, M. S. 2018, *ApJ*, 864, 136
 Bisschop, S. E., Jørgensen, J. K., van Dishoeck, E. F., & de Wachter, E. B. M. 2007, *A&A*, 465, 913
 Blake, G. A., van Dishoeck, E. F., Jansen, D. J., Groesbeck, T. D., & Mundy, L. G. 1994, *ApJ*, 428, 680
 Bøgelund, E. G., Barr, A. G., Taquet, V., et al. 2019, *A&A*, 628, A2
 Bracco, A., Palmeirim, P., André, P., et al. 2017, *A&A*, 604, A52
 Bradley, L., Sipőcz, B., Robitaille, T., et al. 2021, *astropy/photutils: 1.2.0*
 Brinch, C. & Hogerheijde, M. R. 2010, *A&A*, 523, A25
 Calcutt, H., Willis, E. R., Jørgensen, J. K., et al. 2019, *A&A*, 631, A137
 Camacho, V., Vázquez-Semadeni, E., Ballesteros-Paredes, J., et al. 2016, *ApJ*, 833, 113
 Camacho, V., Vázquez-Semadeni, E., Palau, A., Busquet, G., & Zamora-Avilés, M. 2020, *ApJ*, 903, 46
 Carey, S. J., Feldman, P. A., Redman, R. O., et al. 2000, *ApJ*, 543, L157
 Carey, S. J., Noriega-Crespo, A., Mizuno, D. R., et al. 2009, *PASP*, 121, 76
 Caselli, P. & Myers, P. C. 1995, *ApJ*, 446, 665
 Caswell, J. L. 1998, *MNRAS*, 297, 215
 Cesaroni, R., Beltrán, M. T., Zhang, Q., Beuther, H., & Fallscheer, C. 2011, *A&A*, 533, A73
 Cesaroni, R., Beuther, H., Ahmadi, A., et al. 2019, *A&A*, 627, A68
 Cesaroni, R., Olmi, L., Walmsley, C. M., Churchwell, E., & Hofner, P. 1994, *ApJ*, 435, L137
 Chapin, E. L., Berry, D. S., Gibb, A. G., et al. 2013, *MNRAS*, 430, 2545
 Choi, J., Dotter, A., Conroy, C., et al. 2016, *The Astrophysical Journal*, 823, 102
 Churchwell, E., Walmsley, C. M., & Cesaroni, R. 1990, *A&AS*, 83, 119
 Contreras, Y., Schuller, F., Urquhart, J. S., et al. 2013, *A&A*, 549, A45
 Coughlin, E. R. 2017, *ApJ*, 835, 40
 Csengeri, T., Bontemps, S., Schneider, N., et al. 2011, *ApJ*, 740, L5
 Csengeri, T., Urquhart, J. S., Schuller, F., et al. 2014, *A&A*, 565, A75
 Csengeri, T., Weiss, A., Wyrowski, F., et al. 2016, *A&A*, 585, A104
 Cummins, S. E., Green, S., Thaddeus, P., & Linke, R. A. 1983, *ApJ*, 266, 331
 Curry, C. L. & McKee, C. F. 2000, *ApJ*, 528, 734
 Cyganowski, C. J., Whitney, B. A., Holden, E., et al. 2008, *AJ*, 136, 2391
 Dempsey, J. T., Friberg, P., Jennens, T., et al. 2013, *MNRAS*, 430, 2534
 Dullemond, C. P., Juhasz, A., Pohl, A., et al. 2012, *RADMC-3D: A multi-purpose radiative transfer tool*, *Astrophysics Source Code Library*
 Esplugues, G. B., Viti, S., Goicoechea, J. R., & Cernicharo, J. 2014, *A&A*, 567, A95
 Estalella, R. 2017, *PASP*, 129, 025003
 Falgarone, E. & Puget, J. L. 1985, *A&A*, 142, 157
 Fallscheer, C., Beuther, H., Zhang, Q., Keto, E., & Sridharan, T. K. 2009, *A&A*, 504, 127
 Fayolle, E. C., Öberg, K. I., Garrod, R. T., van Dishoeck, E. F., & Bisschop, S. E. 2015, *A&A*, 576, A45
 Federrath, C. & Klessen, R. S. 2013a, *ApJ*, 763, 51
 Federrath, C. & Klessen, R. S. 2013b, *ApJ*, 763, 51
 Flower, D. R., Pineau des Forêts, G., & Rabli, D. 2010, *MNRAS*, 409, 29
 Flower, D. R., Pineau Des Forêts, G., & Walmsley, C. M. 2006, *A&A*, 449, 621
 Foreman-Mackey, D., Hogg, D. W., Lang, D., & Goodman, J. 2013, *PASP*, 125, 306
 Foster, P. N. & Chevalier, R. A. 1993, *ApJ*, 416, 303
 Garrod, R. T., Belloche, A., Müller, H. S. P., & Menten, K. M. 2017, *A&A*, 601, A48
 Garrod, R. T. & Herbst, E. 2006, *A&A*, 457, 927
 Gerner, T., Beuther, H., Semenov, D., et al. 2014, *A&A*, 563, A97
 Giannetti, A., Leurini, S., Wyrowski, F., et al. 2017, *A&A*, 603, A33
 Gieser, C., Beuther, H., Semenov, D., et al. 2021, *A&A*, 648, A66
 Girichidis, P., Federrath, C., Banerjee, R., & Klessen, R. S. 2011, *MNRAS*, 413, 2741
 Girichidis, P., Konstantin, L., Whitworth, A. P., & Klessen, R. S. 2014, *ApJ*, 781, 91
 Glover, S. C. O. & Clark, P. C. 2012, *MNRAS*, 421, 9
 Goldsmith, P. F. 2001, *ApJ*, 557, 736
 Gómez, G. C., Vázquez-Semadeni, E., & Palau, A. 2021, *MNRAS*, 502, 4963
 Gómez, L., Luis, L., Hernández-Curiel, I., et al. 2010, *ApJS*, 191, 207
 Gómez-Ruiz, A. I., Kurtz, S. E., Araya, E. D., Hofner, P., & Loinard, L. 2016, *ApJS*, 222, 18
 Graninger, D. M., Wilkins, O. H., & Öberg, K. I. 2016, *ApJ*, 819, 140
 Grave, J. M. C. & Kumar, M. S. N. 2009, *A&A*, 498, 147
 Green, J. A. & McClure-Griffiths, N. M. 2011, *MNRAS*, 417, 2500
 Green, S. 1986, *ApJ*, 309, 331
 Griffin, M. J., Abergel, A., Abreu, A., et al. 2010, *A&A*, 518, L3
 Güsten, R., Nyman, L. Å., Schilke, P., et al. 2006, *A&A*, 454, L13
 Guszejnov, D., Hopkins, P. F., & Grudić, M. Y. 2018, *MNRAS*, 477, 5139
 Guszejnov, D., Hopkins, P. F., & Ma, X. 2017, *MNRAS*, 472, 2107
 Guszejnov, D., Krumholz, M. R., & Hopkins, P. F. 2016, *MNRAS*, 458, 673
 Hacar, A., Kainulainen, J., Tafalla, M., Beuther, H., & Alves, J. 2016, *A&A*, 587, A97
 Harju, J., Lehtinen, K., Booth, R. S., & Zinchenko, I. 1998, *A&AS*, 132, 211
 Hatchell, J. & van der Tak, F. F. S. 2003, *A&A*, 409, 589
 Helmich, F. P. & van Dishoeck, E. F. 1997, *A&AS*, 124, 205
 Hennebelle, P., Commerçon, B., Lee, Y.-N., & Chabrier, G. 2020, *ApJ*, 904, 194
 Henriksen, R., Andre, P., & Bontemps, S. 1997, *A&A*, 323, 549
 Herpin, F., Marseille, M., Wakelam, V., Bontemps, S., & Lis, D. C. 2009, *A&A*, 504, 853
 Heyer, M., Krawczyk, C., Duval, J., & Jackson, J. M. 2009, *ApJ*, 699, 1092
 Hildebrand, R. H. 1983, *QJRAS*, 24, 267
 Ho, P. T. P. & Haschick, A. D. 1986, *ApJ*, 304, 501
 Hofner, P. & Churchwell, E. 1996, *A&AS*, 120, 283
 Hosokawa, T. & Omukai, K. 2009, *ApJ*, 691, 823
 Humire, P. K., Thiel, V., Henkel, C., et al. 2020, *A&A*, 642, A222
 Izquierdo, A. F., Galván-Madrid, R., Maud, L. T., et al. 2018, *MNRAS*, 478, 2505
 Izquierdo, A. F., Smith, R. J., Glover, S. C. O., et al. 2021, *MNRAS*, 500, 5268
 Jacobsen, S. K., Jørgensen, J. K., van der Wiel, M. H. D., et al. 2018, *A&A*, 612, A72

- Jappsen, A. K., Klessen, R. S., Larson, R. B., Li, Y., & Mac Low, M. M. 2005, *A&A*, 435, 611
- Jiang, X.-J., Liu, H. B., Zhang, Q., et al. 2015, *ApJ*, 808, 114
- Jørgensen, J. K., Bourke, T. L., Myers, P. C., et al. 2007, *ApJ*, 659, 479
- Juvela, M., He, J., Pattle, K., et al. 2018, *A&A*, 612, A71
- Kainulainen, J., Beuther, H., Banerjee, R., Federrath, C., & Henning, T. 2011, *A&A*, 530, A64
- Kainulainen, J., Beuther, H., Henning, T., & Plume, R. 2009, *A&A*, 508, L35
- Kauffmann, J., Pillai, T., & Goldsmith, P. F. 2013, *ApJ*, 779, 185
- Keto, E. R. 1990, *ApJ*, 355, 190
- Keto, E. R., Ho, P. T. P., & Haschick, A. D. 1988, *ApJ*, 324, 920
- Keto, E. R., Ho, P. T. P., & Reid, M. J. 1987, *ApJ*, 323, L117
- Klessen, R. S. 2000, *ApJ*, 535, 869
- Klessen, R. S. & Hennebelle, P. 2010, *A&A*, 520, A17
- Klessen, R. S., Spaans, M., & Jappsen, A.-K. 2007, *MNRAS*, 374, L29
- Koda, J., Sawada, T., Wright, M. C. H., et al. 2011, *ApJS*, 193, 19
- Kritsuk, A. G., Norman, M. L., & Wagner, R. 2011, *ApJ*, 727, L20
- Kroupa, P., Tout, C. A., & Gilmore, G. 1993, *MNRAS*, 262, 545
- Kroupa, P., Weidner, C., Pflamm-Altenburg, J., et al. 2013, *The Stellar and Sub-Stellar Initial Mass Function of Simple and Composite Populations*, ed. T. D. Oswalt & G. Gilmore, Vol. 5, 115
- Krumholz, M. R. 2014, *MNRAS*, 437, 1662
- Krumholz, M. R., Klein, R. I., & McKee, C. F. 2011, *ApJ*, 740, 74
- Krumholz, M. R., Klein, R. I., & McKee, C. F. 2012, *ApJ*, 754, 71
- Krumholz, M. R. & McKee, C. F. 2005, *ApJ*, 630, 250
- Kuiper, T. B. H., Kuiper, E. N. R., Dickinson, D. F., Turner, B. E., & Zuckerman, B. 1984, *ApJ*, 276, 211
- Kurono, Y., Morita, K.-I., & Kamazaki, T. 2009, *PASJ*, 61, 873
- Larson, R. B. 1969, *MNRAS*, 145, 271
- Larson, R. B. 1981, *MNRAS*, 194, 809
- Lee, E. J., Chang, P., & Murray, N. 2015, *ApJ*, 800, 49
- Lee, Y.-N. & Hennebelle, P. 2019, *A&A*, 622, A125
- Leurini, S., Codella, C., López-Sepulcre, A., et al. 2014, *A&A*, 570, A49
- Leurini, S., Menten, K. M., & Walmsley, C. M. 2016, *A&A*, 592, A31
- Leurini, S., Schilke, P., Menten, K. M., et al. 2004, *A&A*, 422, 573
- Leurini, S., Schilke, P., Wyrowski, F., & Menten, K. M. 2007, *A&A*, 466, 215
- Li, J., Wang, J., Zhu, Q., Zhang, J., & Li, D. 2015, *ApJ*, 802, 40
- Li, J. I.-H., Liu, H. B., Hasegawa, Y., & Hirano, N. 2017, *ApJ*, 840, 72
- Li, S., Zhang, Q., Pillai, T., et al. 2019, *ApJ*, 886, 130
- Lin, Y., Csengeri, T., Wyrowski, F., et al. 2019, *A&A*, 631, A72
- Lin, Y., Liu, H. B., Dale, J. E., et al. 2017, *ApJ*, 840, 22
- Lin, Y., Liu, H. B., Li, D., et al. 2016, *ApJ*, 828, 32
- Liu, H. B. 2017, *A&A*, 597, A70
- Liu, H. B. 2019, *ApJ*, 877, L22
- Liu, H. B., Chen, H.-R. V., Román-Zúñiga, C. G., et al. 2019, *ApJ*, 871, 185
- Liu, H. B., Galván-Madrid, R., Jiménez-Serra, I., et al. 2015, *ApJ*, 804, 37
- Liu, H. B., Quintana-Lacaci, G., Wang, K., et al. 2012, *ApJ*, 745, 61
- Liu, H. B., Zhang, Q., & Ho, P. T. P. 2011, *ApJ*, 729, 100
- Lodders, K. 2003, *ApJ*, 591, 1220
- Lomax, O., Whitworth, A. P., & Hubber, D. A. 2015, *MNRAS*, 449, 662
- Longmore, S. N., Pillai, T., Keto, E., Zhang, Q., & Qiu, K. 2011, *ApJ*, 726, 97
- Lowe, I., Mason, B., Bhandarkar, T., et al. 2021, *arXiv e-prints*, arXiv:2105.13432
- Lynch, S. M. 2007, *Introduction to Applied Bayesian Statistics and Estimation for Social Scientists* (New York, NY: Springer Science & Business Media, LLC.)
- Lynden-Bell, D. & Pringle, J. E. 1974, *MNRAS*, 168, 603
- Mathis, J. S., Mezger, P. G., & Panagia, N. 1983, *A&A*, 500, 259
- McKee, C. F. & Holliman, John H., I. 1999, *ApJ*, 522, 313
- McKee, C. F. & Tan, J. C. 2003, *ApJ*, 585, 850
- McLaughlin, D. E. & Pudritz, R. E. 1997, *ApJ*, 476, 750
- Minh, Y. C., Liu, S. Y., Chen, H. R., & Su, Y. N. 2011, *ApJ*, 737, L25
- Molinari, S., Merello, M., Elia, D., et al. 2016, *ApJ*, 826, L8
- Molinari, S., Pezzuto, S., Cesaroni, R., et al. 2008, *A&A*, 481, 345
- Molinari, S., Swinyard, B., Bally, J., et al. 2010, *A&A*, 518, L100
- Möller, T., Endres, C., & Schilke, P. 2017, *A&A*, 598, A7
- Monsch, K., Pineda, J. E., Liu, H. B., et al. 2018, *ApJ*, 861, 77
- Motte, F., Bontemps, S., & Louvet, F. 2018, *ARA&A*, 56, 41
- Mottram, J. C., Beuther, H., Ahmadi, A., et al. 2020, *A&A*, 636, A118
- Mouschovias, T. C. & Morton, S. A. 1991, *ApJ*, 371, 296
- Mueller, K. E., Shirley, Y. L., Evans, Neal J., I., & Jacobson, H. R. 2002, *ApJS*, 143, 469
- Müller, H. S. P., Thorwirth, S., Roth, D. A., & Winnewisser, G. 2001, *A&A*, 370, L49
- Murray, D. W., Chang, P., Murray, N. W., & Pittman, J. 2017, *MNRAS*, 465, 1316
- Murray, N. & Chang, P. 2015, *ApJ*, 804, 44
- Myers, P. C. 2015, *ApJ*, 806, 226
- Nomura, H. & Millar, T. J. 2004, *A&A*, 414, 409
- Offner, S. S. R., Klein, R. I., McKee, C. F., & Krumholz, M. R. 2009, *ApJ*, 703, 131
- Ossenkopf, V. & Henning, T. 1994, *A&A*, 291, 943
- Padoan, P., Haugbølle, T., & Nordlund, Å. 2012, *ApJ*, 759, L27
- Padoan, P., Haugbølle, T., Nordlund, Å., & Frimann, S. 2017, *ApJ*, 840, 48
- Padoan, P., Pan, L., Juvela, M., Haugbølle, T., & Nordlund, Å. 2020, *ApJ*, 900, 82
- Palau, A., Estalella, R., Girart, J. M., et al. 2014, *ApJ*, 785, 42
- Pan, L. & Padoan, P. 2009, *ApJ*, 692, 594
- Parmentier, G. 2019, *ApJ*, 887, 179
- Passot, T. & Vázquez-Semadeni, E. 1998, *Phys. Rev. E*, 58, 4501
- Penston, M. V. 1969, *MNRAS*, 144, 425
- Persson, M. V., Harsono, D., Tobin, J. J., et al. 2016, *A&A*, 590, A33
- Pham, D. T., Ghanbarzadeh, A., Koç, E., et al. 2006, in *The Bees Algorithm - A Novel Tool for Complex Optimisation Problems*
- Pillai, T., Wyrowski, F., Carey, S. J., & Menten, K. M. 2006, *A&A*, 450, 569
- Plume, R., Jaffé, D. T., II, N. J. E., Martin-Pintado, J., & Gomez-Gonzalez, J. 1997, *The Astrophysical Journal*, 476, 730
- Poglitsch, A., Waelkens, C., Geis, N., et al. 2010, *A&A*, 518, L2
- Purcell, C. R., Balasubramanyam, R., Burton, M. G., et al. 2006, *MNRAS*, 367, 553
- Qi, C. 2003, in *SFCHEM 2002: Chemistry as a Diagnostic of Star Formation*, ed. C. L. Curry & M. Fich, 393
- Qiu, K., Zhang, Q., Beuther, H., & Yang, J. 2007, *ApJ*, 654, 361
- Rabli, D. & Flower, D. R. 2010, *MNRAS*, 406, 95
- Ragan, S., Henning, T., Krause, O., et al. 2012, *A&A*, 547, A49
- Ragan, S. E., Henning, T., Tackenberg, J., et al. 2014, *A&A*, 568, A73
- Rivilla, V. M., Beltrán, M. T., Cesaroni, R., et al. 2017, *A&A*, 598, A59
- Robertson, B. & Goldreich, P. 2012, *ApJ*, 750, L31
- Rodríguez-Garza, C. B., Kurtz, S. E., Gómez-Ruiz, A. I., et al. 2017, *ApJS*, 233, 4
- Rolfis, R., Schilke, P., Wyrowski, F., et al. 2011, *A&A*, 527, A68
- Roy, A., André, P., Palmeirim, P., et al. 2014, *A&A*, 562, A138
- Sanhueza, P., Contreras, Y., Wu, B., et al. 2019, *ApJ*, 886, 102
- Sanhueza, P., Jackson, J. M., Zhang, Q., et al. 2017, *ApJ*, 841, 97
- Sanna, A., Reid, M. J., Menten, K. M., et al. 2014, *ApJ*, 781, 108
- Sault, R. J., Teuben, P. J., & Wright, M. C. H. 1995, in *Astronomical Society of the Pacific Conference Series*, Vol. 77, *Astronomical Data Analysis Software and Systems IV*, ed. R. A. Shaw, H. E. Payne, & J. J. E. Hayes, 433
- Schuller, F., Menten, K. M., Contreras, Y., et al. 2009, *A&A*, 504, 415
- Shirley, Y. L. 2015, *PASP*, 127, 299
- Shu, F. H. 1977, *ApJ*, 214, 488
- Siringo, G., Kreysa, E., Kovács, A., et al. 2009, *A&A*, 497, 945
- Smith, R. J., Longmore, S., & Bonnell, I. 2009, *MNRAS*, 400, 1775
- Smith, R. J., Trefß, R. G., Sormani, M. C., et al. 2020, *MNRAS*, 492, 1594
- Sollins, P. K., Zhang, Q., Keto, E., & Ho, P. T. P. 2005, *ApJ*, 624, L49
- Spaans, M. & Silk, J. 2000, *ApJ*, 538, 115
- Sridharan, T. K., Beuther, H., Saito, M., Wyrowski, F., & Schilke, P. 2005, *ApJ*, 634, L57
- Sutton, E. C., Blake, G. A., Genzel, R., Masson, C. R., & Phillips, T. G. 1986, *ApJ*, 311, 921
- Traficante, A., Lee, Y. N., Hennebelle, P., et al. 2018, *A&A*, 619, L7
- Troscopmt, N., Faure, A., Maret, S., et al. 2009, *A&A*, 506, 1243
- Urquhart, J. S., König, C., Giannetti, A., et al. 2018, *MNRAS*, 473, 1059
- van der Tak, F. F. S., Black, J. H., Schöier, F. L., Jansen, D. J., & van Dishoeck, E. F. 2007, *A&A*, 468, 627
- van der Tak, F. F. S., van Dishoeck, E. F., Evans, Neal J., I., & Blake, G. A. 2000, *ApJ*, 537, 283
- van Dishoeck, E. F., Blake, G. A., Jansen, D. J., & Groesbeck, T. D. 1995, *ApJ*, 447, 760
- van 't Hoff, M. L. R., van Dishoeck, E. F., Jørgensen, J. K., & Calcutt, H. 2020, *A&A*, 633, A7
- Varricatt, W. P., Davis, C. J., Ramsay, S., & Todd, S. P. 2010, *MNRAS*, 404, 661
- Varricatt, W. P., Wouterloot, J. G. A., Ramsay, S. K., & Davis, C. J. 2018, *MNRAS*, 480, 4231
- Vasyunina, T., Vasyunin, A. I., Herbst, E., et al. 2014, *ApJ*, 780, 85
- Vázquez-Semadeni, E., Palau, A., Ballesteros-Paredes, J., Gómez, G. C., & Zamora-Avilés, M. 2019, *MNRAS*, 490, 3061
- Wakelam, V., Ceccarelli, C., Castets, A., et al. 2005, *A&A*, 437, 149
- Wakelam, V., Hersant, F., & Herpin, F. 2011, *A&A*, 529, A112
- Walch, S., Burkert, A., Whitworth, A., Naab, T., & Gritschneider, M. 2009, *MNRAS*, 400, 13
- Wang, Y., Zhang, Q., Pillai, T., Wyrowski, F., & Wu, Y. 2008, *ApJ*, 672, L33
- Ward-Thompson, D., Motte, F., & Andre, P. 1999, *MNRAS*, 305, 143
- Watanabe, N., Shiraki, T., & Kouchi, A. 2003, *The Astrophysical Journal*, 588, L121
- Whitworth, A. P., Bhattal, A. S., Francis, N., & Watkins, S. J. 1996, *MNRAS*, 283, 1061
- Wienen, M., Wyrowski, F., Menten, K. M., et al. 2015, *A&A*, 579, A91
- Williams, J. P., Blitz, L., & McKee, C. F. 2000, in *Protostars and Planets IV*, ed. V. Mannings, A. P. Boss, & S. S. Russell, 97
- Williams, S. J., Fuller, G. A., & Sridharan, T. K. 2005, *A&A*, 434, 257
- Wilson, T. L., Rohlf, K., & Hüttemeister, S. 2013, *Tools of Radio Astronomy*
- Wood, D. O. S. & Churchwell, E. 1989, *ApJS*, 69, 831
- Wyrowski, F., Güsten, R., Menten, K. M., Wiesemeyer, H., & Klein, B. 2012, *A&A*, 542, L15
- Xu, S. & Lazarian, A. 2020, *ApJ*, 890, 157
- Zapata, L. A., Rodríguez, L. F., Ho, P. T. P., Beuther, H., & Zhang, Q. 2006, *AJ*, 131, 939
- Zhang, Q., Wang, Y., Pillai, T., & Rathborne, J. 2009, *ApJ*, 696, 268
- Öberg, K. I., Fayolle, E. C., Reiter, J. B., & Cyganowski, C. 2014, *Faraday Discuss.*, 168, 81

Appendix A: Target sources

Appendix A.1: G19.882-00.534

G19.882-00.534 (IRAS 18264-1152), is classified as an extended green object (EGO, Cyganowski et al. 2008), located at 3.7 kpc with luminosity of $>10^4 L_{\odot}$. Most prominent features of this source are the high-velocity outflow (Qiu et al. 2007, Leurini et al. 2014) and the high level of maser activity (among a sample of 56 high-mass star-forming regions, Rodríguez-Garza et al. 2017). The outflow is oriented in a east-west direction, showing enhanced H_2 near-infrared emission as well (Varricatt et al. 2010). Sensitive 7 mm and 1.3 cm observations resolved the source into a triple system, consisting of two optically thin HII or dust emitting sources, and a thermal jet or a partially optically thick HII region (Zapata et al. 2006).

Appendix A.2: G08.684-00.366 and G08.671-00.356

These two massive star-forming clumps are part of the IRAS 18032-2137 star-forming cloud located at 4.8 kpc (Purcell et al. 2006). Multiple water, methanol and hydroxide masers are detected towards both sources (Hofner & Churchwell 1996, Caswell 1998, Gómez et al. 2010). G08.671-00.356 ($\sim 9000 L_{\odot}$) is a UCHII region (Wood & Churchwell 1989), while G08.684-00.366 ($\sim 3000 L_{\odot}$) is a less evolved relatively infrared weak source, lying $1'$ offset in the north-eastern direction. Strong SiO emission towards G08.684-00.366 indicates that star formation already takes place in this source (Harju et al. 1998). Previous SMA observations resolve the source into 3 dense cores accompanied by extended outflow components traced by CO (2-1) emission; the core masses are around several to ten solar masses, a small fraction of the total clump mass (Longmore et al. 2011).

Appendix A.3: G10.624-00.380

G10.624-00.380 is an extremely luminous and massive ($>10^5 L_{\odot}$, $\sim 5000 M_{\odot}$) OB cluster forming clump in the galaxy, located at 4.95 kpc (Sanna et al. 2014). Previous high angular resolution submm and centimeter observations revealed that the clump in the central 0.6 pc is a flattened rotating system (Keto et al. 1987, 1988) where multiple UCHII regions are deeply embedded (Ho & Haschick 1986, Sollins et al. 2005); the clump is fed by the converging flows from ambient filamentary clouds (Liu et al. 2011, 2012). Within the HII region, absorption lines indicate that the gas accretion continues despite the ionising and radiative pressure (Keto 1990). Overall, the clump seems to be in an global collapsing state with a rotating Toomre-unstable disk-like structure in the center (Liu 2017).

Appendix A.4: G13.658-00.599

G13.658-00.599 (IRAS 18144-1723) is a molecular clump with a luminosity of $>10^4 L_{\odot}$ at 3.7 kpc. It is associated with multiple water and methanol masers (Gómez-Ruiz et al. 2016). H_2 emission displays a bowshock feature $18''$ offset in the west from the center of the IRAS emission, which seems to originate from an extended K-band continuum source associated with the IRAS source (Varricatt et al. 2010). The bowshock feature is surrounded by multiple 44 GHz methanol masers (Gómez-Ruiz et al. 2016), indicating it is likely caused by outflow activity. Deep mid-infrared imaging reveals that the central source hosts two YSOs separated by ~ 10000 au, at different evolutionary stages; outflow traced by CO(3-2) line coincides well with the

H_2 emission, and is likely caused by the younger source in formation (Varricatt et al. 2018).

Appendix A.5: G31.412+00.307

G31.412+00.307 is a well-known hot massive core (HMC) that has been extensively studied by both single-dish and interferometry observations (e.g. Cesaroni et al. 1994, Beltrán et al. 2004, 2018, Rivilla et al. 2017), a source showing great chemical richness. It is located at a kinematic distance of 7.9 kpc (Churchwell et al. 1990), and has a luminosity of $\geq 10^5 L_{\odot}$. The central hot core structure is massive and compact ($\sim 500 M_{\odot}$ of ~ 8000 au in size, Cesaroni et al. 2011, Beltrán et al. 2004). There is an ultra-compact HII region $5''$ away from the core (Churchwell et al. 1990). The kinematic features consistently support a rotating core experiencing infall motions (Cesaroni et al. 2011, Wyrowski et al. 2012). Recent ALMA observations of higher angular (~ 1700 au) resolution suggest that both the rotation and infall velocities increase towards the center, and that the core is composed of a main core of size ~ 5300 au and a satellite core of much smaller mass (Beltrán et al. 2018). The overall monolithic feature of source G31 makes it an ideal source for understanding the high-mass star formation scenario in light of gas mass origin and evolution.

Appendix A.6: G18.606-00.074

G18.606-00.074, is a massive infrared-dark clump located in a ~ 4 pc long filamentary cloud associated with IRAS18223 (Carey et al. 2000, Beuther et al. 2002b, Sridharan et al. 2005). The parental molecular cloud is part of an even larger (>50 pc) molecular gas filament (e.g. Kainulainen et al. 2011, Ragan et al. 2014), which undergoes star formation activities of various evolutionary stages (e.g., Beuther et al. 2002b, 2007, 2010, Fallscheer et al. 2009, Ragan et al. 2012). G18.606-00.074 (also named as IRDC18223-3, or core 11 in Beuther et al. 2015), compared to its ambient core and clump structures, appears to have a larger mass reservoir, showing larger linewidth of N_2H^+ line (Beuther et al. 2015).

Appendix A.7: G28.397+00.080

G28.397+00.080 (named as P2 in Wang et al. 2008) is a molecular clump located in a massive ($>10^4 M_{\odot}$) filamentary infrared dark cloud, G28.34+0.06 (Carey et al. 2000, Pillai et al. 2006, Lin et al. 2017). The central region of the clump is not associated with any near-infrared compact source counterpart while appears bright at $24/70 \mu m$ wavelength (Fig. 3, Wang et al. 2008). It also shows line emission of COMs such as CH_3OCH_3 , CH_3CHO (Zhang et al. 2009, Vasyunina et al. 2014), likely hosting massive protostar(s) which heats the gas up to 45 K, as measured from NH_3 observations (Zhang et al. 2009).

Appendix B: Subtraction of free-free emission from SMA 1.2 mm continuum

We use centimeter radio continuum data collected from the NRAO data archive⁵ for Very Large Array (VLA) for sources G08b, G31 and G10, to estimate the free-free emission contribution to the 1.2 mm flux. Given the time variability of centimeter emission, we select the most recent data products, whose basic information is listed in Table B.1.

⁵ <http://www.aoc.nrao.edu/vlbacald/ArchIndex.shtml>

Assuming that the dust and free-free emission are both optically thin, and that the dust emission follows a spectral index $\beta = 1.0$, then the relations $S_\nu \propto \nu^{2+\beta}$ and $S_\nu \propto \nu^{-0.1}$ describe the variation of the two emission components, respectively, as a function of frequency. The free-free emission at 1.2 mm can then be solved using simultaneous equations of total flux, at two considered frequencies. The centimeter data was smoothed and regridded to match the 1.2 mm data and subtraction was done in a pixel-by-pixel basis. The total flux contributed from free-free emission to the 1.2 mm continuum is also listed in Table B.1.

Appendix C: RADEX modeling of CH₃OH lines: the MCMC procedure

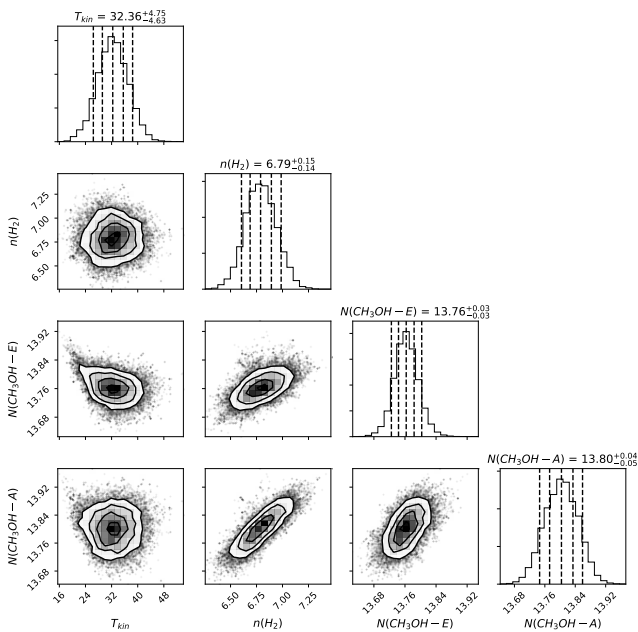


Fig. C.1. Posterior distribution of parameters from MCMC RADEX fitting of CH₃OH (5-4) line series. The column densities of *A/E* type are velocity averaged values ($\log \text{cm}^{-2}/\text{km s}^{-1}$). The vertical dashed lines in the 1d histograms are showing the quantiles of 10%, 25%, 50%, 75%, 90%. The contour levels in the 2D histograms indicate 0.5 σ , 1 σ , 1.5 σ and 2 σ , respectively. The figure shows an example of the fitted parameters of observed lines in one pixel of clump G08b.

For both *E*-type and *A*-type CH₃OH, we generated RADEX model grids in the column density ($N/\Delta v$) range from 10^{12} to 10^{18}cm^{-2} (with 60 logarithmically spaced uniform intervals), in the density range from 10^4 to 10^9cm^{-3} (with 100 logarithmically spaced uniform intervals), and in the kinetic temperature range between 10–200 K (with 80 uniform intervals). In the RADEX models, the linewidth is taken as 1 km/s for all the grids of parameters, while the total column densities (shown in Fig. C.2) are obtained by multiply the fitted $N/\Delta v$ with the linewidth obtained from Gaussian fits (Sect. 3.5). The external radiation field was taken to be the cosmic background at 3 K. We used a linear interpolator to estimate the line intensities for parameters in between the intervals to better constrain the parameters and to allow for a continuous examination of parameter space. Nevertheless, the accuracy of the best-fit parameters remains limited by the resolution of the grid.

We fit the *A*- and *E*-CH₃OH (5-4) ($v_t = 0$) line profiles with Gaussian models pixel-by-pixel for all the sources. We as-

sumed that the line width is identical for all the K components and for *A* and *E* types. We also took into consideration that the HNC0 11_{0,11} – 10_{0,10} line is blended with the CH₃OH 5₋₁ – 4₋₁ *E* line ($\delta V \sim 8.44 \text{km s}^{-1}$) and removed the contribution from this HNC0 line by fitting an additional Gaussian component of which the line-width and amplitude are free parameters.

We employ the Markov Chains Monte Carlo (MCMCs) method with an affine invariant sampling algorithm⁶ (emcee, Foreman-Mackey et al. 2013) to perform the pixel-by-pixel fitting. Our prior assumption for each pixel adopted the temperature T_{rot} predicted from the temperature profiles in Section 3.4, which means that for T_{kin} we assumed a normal distribution centering at T_{rot} and with a standard deviation of 5 K. For the other parameters, the priors were assumed to be uniform distributions. We use a likelihood distribution function which takes into account observational thresholds; the formulas follow,

$$P \propto \prod_i p_i \prod_j p_j \quad (\text{C.1})$$

where p_i stands for probabilities of the i th data that is a robust detection and p_j the j th data that gives a constrain by an upper limit; we adopt the normal distribution as likelihood function,

$$p_i \propto \exp \left[-\frac{1}{2} \left(\frac{f_i^{\text{obs}} - f_i^{\text{model}}}{\sigma_i^{\text{obs}}} \right)^2 \right] \Delta f_i \quad (\text{C.2})$$

$$p_j \propto \int_{-\infty}^{f_{\text{lim},j}^{\text{obs}}} \exp \left[-\frac{1}{2} \left(\frac{f_j - f_j^{\text{model}}}{\sigma_j} \right)^2 \right] df_j, \quad (\text{C.3})$$

in which f_i^{obs} (or f_j) stands for the observed intensity (or intensity upper limit) obtained from Gaussian fit, f_i^{model} (or f_i^{obs}) the model intensity, σ_i^{obs} is the standard error of the observed intensity which was adopted as the fitted 1 σ error of the Gaussian fit, Δf_i being the data offset from the true value of f_i , and df_j the integrated flux probability to the detection threshold $f_{\text{lim},j}^{\text{obs}}$.

The starting points (initialization) for the chains were chosen to be the parameter set corresponding to a global χ^2 minimum calculated between the grid models and the observed values. We also employed the "burn-in" phase in the MCMC chains and several resets of the starting-points to ensure the final chains are reasonably stable around the maximum of the probability density. An example posterior distribution of the fitted parameters is shown in Figure C.1. The obtained $n(\text{H}_2)$ maps and column density maps of CH₃OH for all sources are shown in Figure 11 and Figure C.2, respectively.

After the first run of generating parameter maps, we find that the $n(\text{H}_2)$ of clump G31 are truncated to $\sim 10^9 \text{cm}^{-3}$, the parameter boundary of our conducted RADEX models. Therefore we additionally ran a larger grid with $n(\text{H}_2)$ up to $\sim 10^{11} \text{cm}^{-3}$ with the same range of T_{kin} and N_{mol} as the first grid, and re-derive the parameter maps for this clump.

Appendix D: LTE analysis for other lines

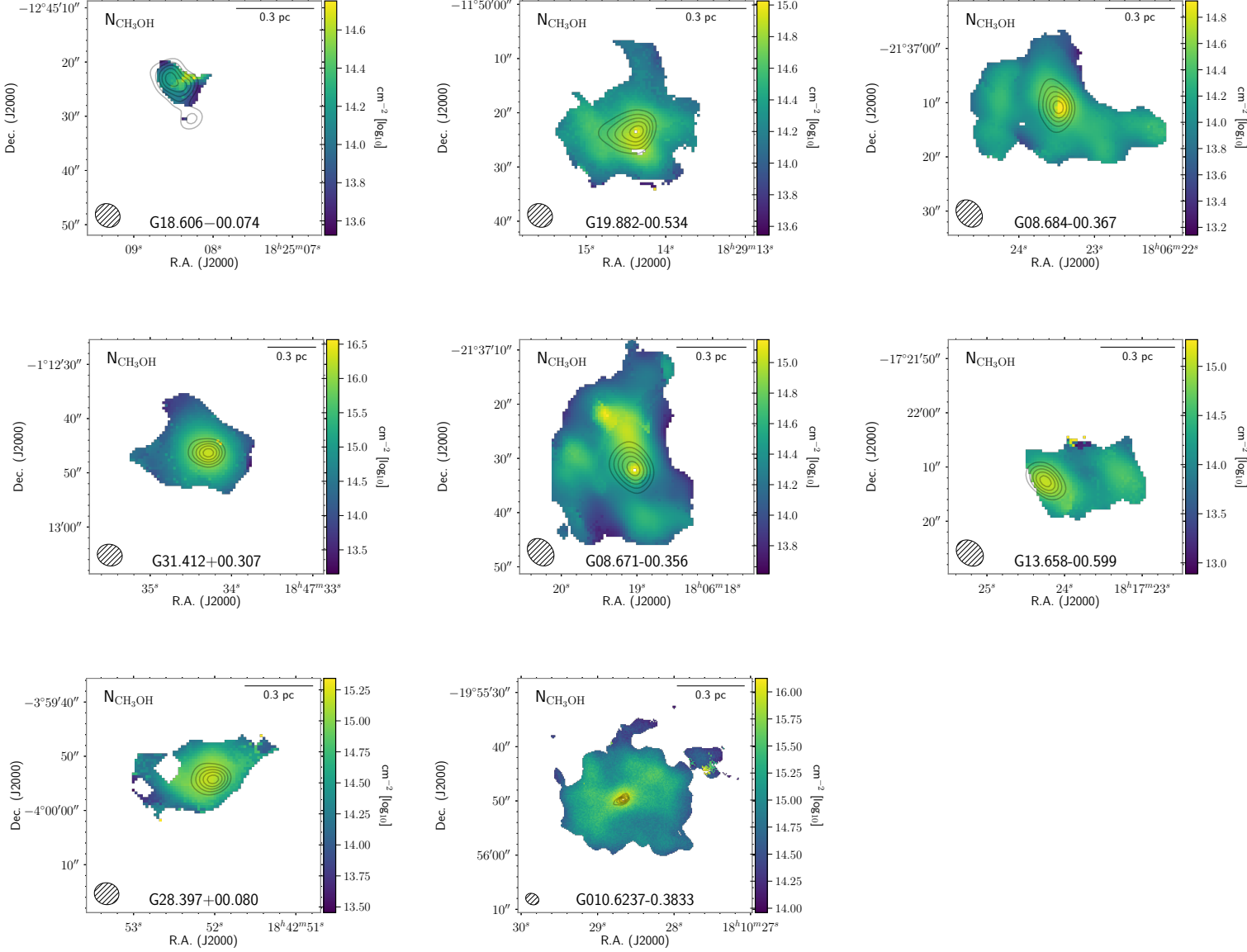
Appendix D.1: CS/C³⁴S (5-4)

CS transitions are commonly adopted tracers for dense gas. Our spectral setup covered the $J=5-4$ transition of CS and its rare isotopologue, C³⁴S, for the 7 sources. For G10, the data we utilized only covered the C³⁴S (5-4) line. In the observed sources, the

⁶ A detailed description of the method can be found in the emcee documentation.

Table B.1. Information of the centimeter continuum data collected from NRAO archive.

Source	Freq. (GHz)	Resolution (")	Obs. Date	Integrated flux (Jy)	Extrapolated total flux of free-free emission at 1.2 mm (Jy)
G31	43.3	1.62	2001-11-26	0.42	0.40
G08b	8.5	0.85	2005-02-28	0.99	0.70
G10	23.8	0.09	2002-02-01	3.55	2.80


Fig. C.2. CH_3OH column density maps ($N_{\text{CH}_3\text{OH}}$) derived from RADEX modeling of all target sources. The beam of CH_3OH $5_{-1}-4_{-1}$ E line is indicated in the bottom left corner. Gray contours indicates the SMA 1.2 mm continuum level from 0.1 to $0.9 \times$ peak flux represented by 5 levels of uniform interval.

CS line and the 1.2 mm continuum emission trace similar structures. Additionally, the CS line images revealed some spatially more extended structures.

Assuming that CS and C^{34}S trace gas of identical temperature and linewidths, the optical depth of the C^{34}S line can be estimated by

$$\frac{W_{\text{CS}}}{W_{\text{C}^{34}\text{S}}} = \frac{[1 - \exp(-R\tau_{\text{C}^{34}\text{S}})]}{[1 - \exp(-\tau_{\text{C}^{34}\text{S}})]}, \quad (\text{D.1})$$

where W_{CS} and $W_{\text{C}^{34}\text{S}}$ are the integrated line intensities, and we assumed a $^{32}\text{S}/^{34}\text{S}$ abundance ratio of $R = 22.6$, which is consistent with terrestrial value, e.g., Lodders (2003), although there are indications that the ratio varies as a function of Galactocentric distance (e.g. Humire et al. 2020). The CS line, as expected, is broader than the C^{34}S line, and shows self-absorption profiles in most of the cases. These are two effects that can mitigate each other's effect on biasing the $\tau_{\text{C}^{34}\text{S}}$ estimate as our derivation

was based on the integrated intensity ratios. We found that $\tau_{\text{C}^{34}\text{S}}$ ranges from less than 0.1 to 0.25 in most of the sources, while it reaches 0.3-0.45 in G08b and values as high as 0.9 in G31.

Assuming a beam filling factor $f = 1$, a lower limit of the excitation temperature (T_{ex}) can be estimated from the brightness temperature of C^{34}S ,

$$J(T_{\text{b}}) = [J(T_{\text{ex}}) - J(T_{\text{bg}})] [1 - \exp(-\tau_{\text{C}^{34}\text{S}})]. \quad (\text{D.2})$$

Since the n_{crit} of CS is higher than the thermometers except CH_3CN used in Sect. 3.4, and because of the fact that there is more extended cold envelope gas contributing to the emission of CS line, as expected, the derived T_{ex} is in general lower than the T_{rot} profiles derived from the observations of multiple transitions of the other molecular thermometers (see Sect. 3.4). The derived T_{ex} is <10 K in G18, in the range of 20-30 K in most of the other sources, and reaches ~ 45 K at the emission peak of G31.

Under LTE assumption, the overall column densities of the C^{34}S ($N_{\text{C}^{34}\text{S}}$) can then be estimated by evaluating the partition functions, adopting T_{ex} , with,

$$N_{\text{tot}} = \frac{8\pi\nu^3}{c^3 A_{\text{ul}}} \frac{Q_{\text{rot}}}{g_{\text{u}}} \exp\left(\frac{E_{\text{up}}}{kT_{\text{ex}}}\right) \left[\exp\left(\frac{h\nu}{kT_{\text{ex}}}\right) - 1\right]^{-1} \int \tau_{\text{C}^{34}\text{S}} dv, \quad (\text{D.3})$$

in which g_{u} stands for the level degeneracy and Q_{rot} the partition function at T_{ex} . The derived C^{34}S column densities are in the range of $4.4 \times 10^{12} - 5.0 \times 10^{14} \text{ cm}^{-2}$.

In an alternative approach, we assumed that the T_{ex} of C^{34}S is the same with the T_{rot} measured from the other molecular thermometers, and then directly solved for $\tau_{\text{C}^{34}\text{S}}$ based on an LTE assumption. The $N_{\text{C}^{34}\text{S}}$ derived this way is 1.1-1.5 times larger for warmer sources except for G18. In G18, the $N_{\text{C}^{34}\text{S}}$ derived with this approach is ~ 10 times smaller than the derivation based on the CS/ C^{34}S intensity ratio. This is due to the dependence between $N_{\text{C}^{34}\text{S}}$ and T_{ex} under LTE assumption: $N_{\text{C}^{34}\text{S}}$ drops significantly below ~ 30 K and slowly increases for larger values of T_{ex} .

Appendix D.2: CCH (3-2)

The hyperfine line components of CCH resulting from electron-nucleus interactions allow for an direct measure of the CCH line optical depth. We followed fitting procedure similar to that described in Estalella (2017), adopting relative line intensities from LTE predictions. From hyperfine line fitting, we derived excitation temperature and optical depth in a pixel-by-pixel basis, and then used these to estimate the CCH column densities. We found that the optical depth of the main line, $\tau_{\text{m}} \sim 0.1$ in extended regions, but can become optically thick at high column densities in localized regions. In most of the sources, τ_{m} reaches up to ~ 3 . But in G18, τ_{m} reaches ~ 10 at the center, which is close to the upper limit in our fitting procedure. The column density of CCH ranges between $1.2 \times 10^{14} - 6 \times 10^{15} \text{ cm}^{-2}$ across the emission region for all the sources. In general, the CCH column density distribution shows porosity over extended regions (~ 0.2 - 0.3 pc) except G18, and is systematically larger in outer regions, resembling a ring-like structure, especially for clump G08b and G31. The central region of the hot massive core G31 is almost completely devoid of CCH emission. Jiang et al. (2015) presented high-angular resolution CCH observations towards clump G10 together with other 3 more evolved high-mass clumps than our sample, which also exhibit ring-like distributions.

Appendix D.3: SO and SO_2

Our spectral setup covered three SO lines (Table 4) which have similar upper level energies E_{up} . These three lines were detected in all clumps except G18. The resolved SO intensities were spatially compact and were confined within where 1.2 mm continuum emission was detected.

The SO_2 $14_{0,14}-13_{1,13}$ ($E_{\text{up}} \sim 94$ K) line was detected in the all clumps except G18 and G28; in G28, a lower excitation transition SO_2 $3_{2,2}-2_{1,1}$ ($E_{\text{up}} \sim 15$ K) was marginally detected.

These SO and SO_2 transitions are likely thermalized given that the emission closely follows the extension of the central core, and are of relatively high critical densities (Table 4). We cannot directly derive the excitation temperatures of the SO and SO_2 molecules owing to not covering multiple transitions, or owing to that the covered transitions have similar E_{up} . Therefore, we adopted the gas temperature derived from the thermometer lines (Section 3.4) when estimating their column densities, assuming LTE condition.

Appendix E: Radiative transfer modeling of multi-wavelength continuum

We divided the 870 μm (using APEX/LABOCA), 450 μm (using JCMT/SCUBA-2), or 350 μm (using CSO/SHARCII or APEX/SABOCA) images (whenever available) of each clump into annuli which have intervals equal to half of the beam FWHM, and then (projected) radially averaged the intensities in the annuli. When the intensity distribution is largely asymmetric with respect to the clump center (e.g., when there is a bright adjacent core/clump or a bright external gas filament), we trimmed the contribution from those asymmetric (sub)structures before making the averages. In practice, at each radius we first derived the mean and standard deviation (I_{std}) of the intensities and then masked the pixels at which the sum of the radial intensities deviates from the mean by more than 0.9 times the sum of radial I_{std} .

We used radiative transfer models to invert these derived radial intensity profiles to radial density profiles. We employed the publicly available Monte Carlo radiative transfer code RADMC-3D (Dullemond et al. 2012). To find the simulated intensity profiles which match the observed ones, our modeling ergodically visited the parameter spaces of the assumed functional form for density (Equation 2, Sect. 3.6). This means that the resultant models, when the number of which is sufficiently large (as in our case we adopt 10,000 models), can represent the average statistical properties of the models constructed from the full parameter space.

To benchmark and refine the radial temperature profile, we conducted aperture photometry with multi-wavelength dust continuum data. We used the tools in Python package photutils (Bradley et al. 2021). The total fluxes at each wavelength of 24, 70, 160, 250, 350, and 500 μm from *Spitzer/MIPS* (Carey et al. 2009), *Herschel/PACS*, and *Herschel/SPIRE* images are measured and they provide an observed SED profile. We then let RADMC-3D generate the SEDs ranging from mid-IR to mm wavelength and ensure that the best-fit model can reproduce an SED profile which is broadly consistent with the observed SED.

We assumed that dust opacity does not have spatial variation and quoted the opacity model from Ossenkopf & Henning (1994). Specifically, we quoted the column evaluated for the thin ice mantle coated dust which was coagulated for 10^5 years in an environment with 10^6 cm^{-3} gas density (hereafter OH5 model). This model has been successfully applied in previous studies to explain the radial profiles of dust emission around high-mass

embedded protostars (Mueller et al. 2002; Rolfs et al. 2011). The maximum grain size in the OH5 opacity model is under the Rayleigh limit such that the scattering opacity can be neglected in the modeling.

The hydrogen gas density profile ($\rho_{\text{bulk}}(r)$) is described by the functional form of Equation 2. Using Monte Carlo radiative transfer to evaluate the temperature distributions (e.g., based on assumptions of heating sources and interstellar radiation field) is subject to a very large degree of freedom. Instead, we adopted the radial gas temperature profile probed by the thermometers in Section 3.4, following the form of Equation 3.

The overall mass of individual clumps derived by single-component SED fitting (M_{sed} as in Table 1) is used as a prior for our subsequent modeling. Given that we only need to fit two free parameters ($\bar{\rho}$, q , c.f. Equation 2), the Markov chain Monte Carlo (MCMC) method has no clear advantage. Instead, for each observed molecular clump, we drew 10,000 samplers from the parameter space of $q = 0.0$ -2.5, $\bar{\rho} = 10^3$ - 10^6 cm $^{-3}$ with a random process. The likelihood function of the clump total mass follows the truncated normal distribution (e.g. Lynch 2007):

$$\ln \mathcal{L} = \begin{cases} -0.5 \left(\frac{M - M_{\text{sed}}}{3M_{\text{sed}}} \right)^2 & (0.2M_{\text{sed}} \leq M \leq 5M_{\text{sed}}) \\ -\text{inf} & (M < 0.2M_{\text{sed}} \text{ or } M > 5M_{\text{sed}}) \end{cases} \quad (\text{E.1})$$

We then ran RADMC-3D for each sampler and convolved the derived images with the corresponding Gaussian beams to compare with the multi-wavelength observations. When summing the χ^2 , we assumed that the observational data can have nominal $\sim 20\%$ errors, and adopted one standard deviation in the radial profile calculation as the uncertainty of the observational data. The χ^2 calculation follows,

$$\chi^2 = \sum_{\lambda} \sum_r \frac{(f_{\text{mod}} - I_{\text{obs}})^2}{I_{\text{std}}^2 + (0.2I_{\text{obs}})^2} \quad (\text{E.2})$$

where \sum_{λ} and \sum_r denote summing over all wavelengths and sampled radii, respectively. f_{mod} stands for the model intensity at a certain radius.

Figure 12 compares the observed radial intensity profiles with the best-fit models. The fitted values of q and $\bar{\rho}$, the (pre-determined) clump radius, overall clump mass, and the characteristic density determined from the best-fit model at 0.1 pc radius, are summarized in Table 6. The posterior probability distributions of $\bar{\rho}$ - q are shown in Figure E.1, with best-fit parameter set marked. In Figure 13 the observed multi-wavelength flux densities are compared with the SED generated from best-fit RADMC-3D models.

It can be seen that the observed SEDs of sources G18, G19, G08a, G13 and G31 show large deviation from that of the best-fit models which were produced based on the assumed $T(r)$ profiles. For sources G18, G19, G08a and G13, the deviations are partially expected as these three sources exhibit the smallest densities in the sample, from the clump center to outer region. It is likely that T_{rot} estimated from aforementioned thermometers is biased to the small proportion of the dense gas at each radius (clumpiness), while the temperature for the bulk gas at each layer, or the *average* gas temperature is smaller. In addition, for the intermediate-scale gas having densities $\leq 10^5$ cm $^{-3}$, which are mostly probed by CH₃CCH (12-11) and H₂CS lines in terms of gas temperature, the gas temperature being higher than dust temperature may also have an origin from turbulent heating, as under such gas densities thermal coupling between

dust and gas is weaker (Pan & Padoan 2009). For G31, which is much denser in terms of bulk gas radially but shows the most prominent monolithic core in the center, the over-estimation of temperature likely originates from optical depth effect.

To refine $T(r)$ as guided by the observed SED shape, we retain the parametric form (Equation 3) as elaborated in Section 3.6, and only adjust the parameter r_{in} (Equation 3), scaled by a factor < 1 . Based on the adjustment, we regenerate SED profiles from RADMC modeling and find the best-fit rescaled r_{in} , which is listed in Table 6 for the 5 sources. For these 5 sources, we then iterate the fitting of radial density profiles from RADMC-3D calculations, based on the adjusted temperature profiles $T(r)$. From Figure E.1, the best-fit parameter set before and after adjusting $T(r)$ are shown together. Decreasing r_{in} in the temperature form, is equivalent to reduce the steepness and absolute value of temperature radial profile, which results in an increment of mean gas density and density profile slope in the radial intensity profile fits, as expected. As a further benchmark, we use RADMC-3D to self-consistently calculate the dust temperature. To convert the clump luminosity to a central stellar source, we use the stellar evolution models of solar metallicity from Choi et al. (2016) which give relations between luminosity, mass, radius and temperature for ZAMS to estimate the stellar T_{eff} . The re-iterated best-fit density model is used to describe the envelope structure. The resultant SED is also shown in Figure 13.

Appendix F: Radiative transfer modeling of CH₃OH and CH₃CCH lines: benchmarking the results from one-component non-LTE/LTE models

The RADEX analysis of CH₃OH (5-4) lines in Section 3.5, with one-component non-LTE assumption, can be biased due to the mixed contribution along the LOS. On the other hand, the RADMC-3D modelings for dust continuum in Appendix E better represents the enclosed masses within certain radii by constraining ρ_{bulk} while they cannot provide constraint on the higher volume density internal structures. To refine our estimates of physical parameters, we build on these two efforts to conduct 3D radiation transfer forward modelings of CH₃OH (5-4) and CH₃CCH (12-11) lines. Specifically, we performed the non-LTE modeling for the excitation conditions using the LIME code (Brinch & Hogerheijde 2010) and then compared the synthetic spectra with the observed spectral cubes. The spatial distributions of CH₃OH (5-4) and CH₃CCH (12-11) line emission are rather extended such that they better characterize the majority of dense gas in the clumps. We focus on benchmarking the radial density profile of the dense gas (ρ_{dense}). We fixed the gas temperature profiles ($T(r)$; Section 3.6) according to the profiles obtained in Section 3.4 (and refined in Appendix E), when constructing the input models. As $T(r)$ has been verified by full radiative transfer of dust continuum by building SEDs, the CH₃CCH (12-11) modeling conducted here is further used as a sanity check that the assumed temperature profile can reproduce the line emission of this thermometer.

The gas density radial profiles were initially specified to be the best fits from the modeling continuum intensity profiles, ρ_{bulk} (Equation 2, see details in Appendix E). Based on this density model and temperature profile $T(r)$, we then experimented various assumptions of the abundance spatial variations of CH₃OH and CH₃CCH, motivated by the results of chemical network from Belloche et al. (2017) and Calcutt et al. (2019).

Based on the chemical network of Belloche et al. (2017), Calcutt et al. (2019) calculated the variation of gas-phase abun-

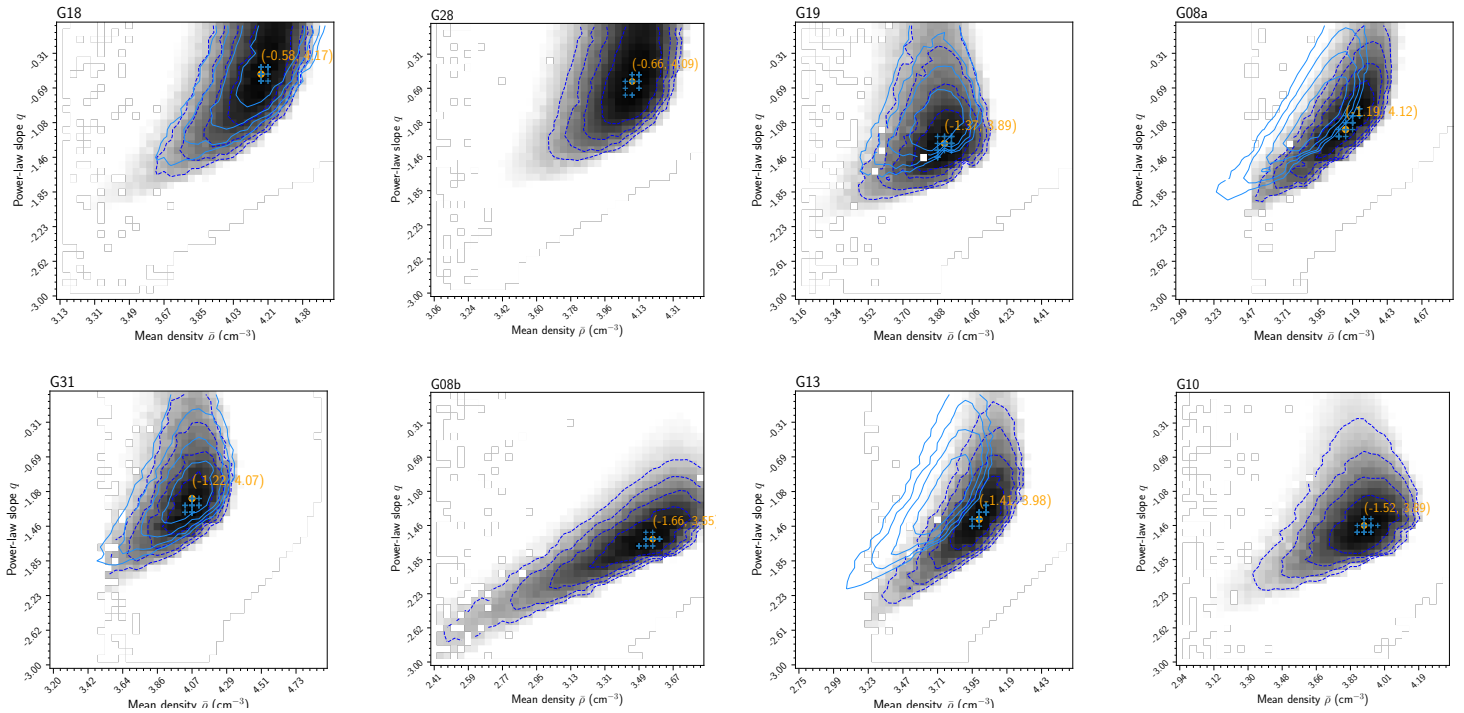


Fig. E.1. χ^2 converted probability distribution of the 10 000 parameter set of RADMC-3D models for all clumps. Orange point indicates the best-fit model. Blue crosses mark the positions of the 30 best-fit models, so there could be overlaps between different parameter set due to the binning. For sources G31, G13, G08a and G19, results before re-adjusting $T(r)$ based on SED are shown as light blue contours.

dance of CH_3CCH as a function of warm-up time at different densities which range from 10^7 to 10^{10} cm^{-3} . In these calculations, a two-stage physical evolution is assumed: a cold collapse stage is followed by a static warm-up stage which reaches a gas temperature of 400 K. The CH_3CCH abundance is enhanced when the gas temperature reaches 30-40 K due to desorption of CH_4 to form CH_3CCH (i.e., dissociative recombination of larger hydrocarbons). The CH_3CCH abundance is significantly enhanced again when the gas temperature reaches 80-100 K, due to the direct desorption of CH_3CCH from grain surfaces. Finally, the models with higher final gas density present systematically lower CH_3CCH abundance since in these high-density models CH_4 desorbs at slightly higher temperature (lower panel of Figure F.1). Similarly, according to the chemical model of Garrod et al. (2017), the abundance of CH_3OH experiences two significant enhancements at 30-40 K and 80-100 K gas temperatures (upper panel of Figure F.1). The chemical modeling include three warm-up models, depending on the timescale for the system to increase from 10-200 K, over 5×10^4 (fast), 2×10^5 (medium) and 1×10^6 (slow) yr (Garrod & Herbst 2006).

To mimic the abundance enhancement in the warm or luck-warm regions as described by these chemical models, we parameterized the CH_3OH and CH_3CCH abundance profiles as Equation 5. Again, we assumed that the *A* and *E*-type CH_3OH have the same abundance. The parameter ranges of X_{in} and X_{out} were chosen by referencing to N_{mol} for CH_3CCH and CH_3OH from XCLASS/RADEX modeling results (Section , 3.4-3.5) and the aforementioned chemical models. Figure F.1 shows a comparison between the parameter space we explored and the chemical modeling results.

Presently, only the collisional coefficients of CH_3OH with para- H_2 are available, although it seems that only in hot shocked gas there is a significant difference between the thermal rate coefficients of collisions with ortho- and para- H_2 (Flower et al.

2010). Our non-LTE models were not affected by the uncertain collisional coefficients because we assumed a low ortho-to para- H_2 ratio (OPR), such that the collisions with ortho- H_2 is negligible. Chemical models and observations towards early stage dense cores indeed indicate an OPR value of $\sim 10^{-3}$ - 10^{-2} (Flower et al. 2006, cf. Troscompt et al. 2009), which is well below the equilibrium value of 3. In the post-shock gas, the OPR may remain low since the short timescale does not allow significant conversion from para- H_2 to ortho- H_2 (Leurini et al. 2016).

When performing non-LTE modeling of CH_3CCH , the collisional rates of CH_3CN (Green 1986) were substituted by those of CH_3CCH . This is a common approach since CH_3CCH and CH_3CN have similar molecular weights and configuration, while there is not yet published collisional rates for CH_3CCH . The collisional rates of CH_3OH were quoted from Rabli & Flower (2010) (c.f., Section 3.5).

To create the distributions of physical properties we adopted the `sf3dmodels` package (Izquierdo et al. 2018) to generate homogeneous grids in Cartesian coordinates, which are then interpolated onto the LIME input format of randomly generated set of points. We used the linear resolution of ~ 0.015 - 0.03 pc (depending on the source radius R_{clump} , Table 6) as grid size which corresponds to better than 1/5 beam size for each source. On each grid, we specified a mean gas velocity using a random process to mimic the turbulent velocity field: the direction was uniformly sampled from the 4π solid angle while the magnitude of the velocity was drawn from a Gaussian distribution with $\sigma = 3.5 \text{ km s}^{-1}$. We additionally adopted a uniform Doppler broadening of 0.4 km s^{-1} ($\sigma_{\text{turb}} = 0.4 \text{ km s}^{-1}$) to accommodate the unresolved (micro-)turbulence velocity. Therefore the intrinsic line-width for each model is $\sigma_{\text{ID}} = \sqrt{\sigma_{\text{turb}}^2 + \sigma_{\text{thermal}}^2}$, where σ_{thermal} is determined by the assumed gas temperature.

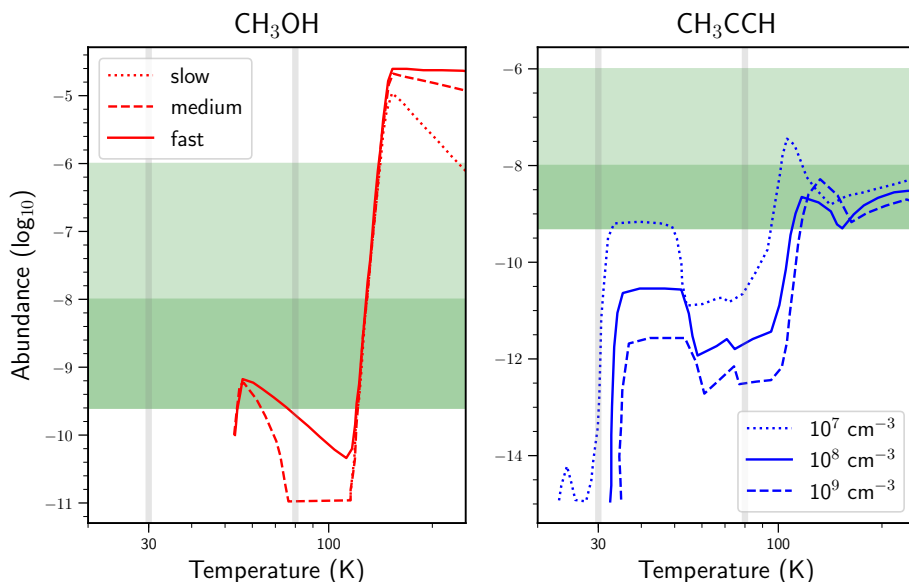


Fig. F.1. The abundance variations of CH_3OH and CH_3CCH from chemical models (lines) and the explored parameter space (filled) for the LIME models based on ρ_{bulk} density model (column A of Table 7). The results from chemical models are shown in lines (solid, dashed and dotted): for CH_3OH the abundance profiles for different warm-up timescales are shown (Garrod et al. 2017); for CH_3CCH , abundance profiles of different final collapse densities are shown (Calcutt et al. 2019). The dark green filled region indicates the lower abundance range explored for X_{out} by the LIME models, and the light green filled region the upper range explored for X_{in} . The vertical gray lines indicate the jump temperature of 30 and 80 K.

This yields linewidths comparable to the observed values ($\Delta V = 3.5 \pm 1.2 \text{ km s}^{-1}$).

We post-processed the output of LIME to match the angular and velocity resolutions of our observations, and then compared the annularly and beam averaged synthetic spectra with those from observed spectral cubes. For each observed clump, the best-fit model was taken as the one with the lowest χ^2 . The parameters of these best-fit chemical models are summarized in Table 7, column A.

We found that these initial models systematically underestimated the intensities of the higher K components of CH_3OH lines in the inner regions for all sources (Figure 15). There are some sources in which the intensities of the higher K components were underestimated also at outer radii. This implies that, in general, the density profiles ρ_{bulk} derived from dust continuum modeling (Appendix E) were not high enough to collisionally excite the high K levels of CH_3OH (e.g., gas may be concentrated in substructures of higher volume density). This was expected, as was revealed by the comparison to the ρ_{dense} derived by RADEX modeling: gas densities are 50-200 times larger than that of ρ_{bulk} derived by single-dish dust continuum. Therefore, we updated the radial density profile in the models according to the RADEX results ρ_{dense} (Section 3.5), following Equation 6. We manually adjusted the flexible parameters, which are the density scaling factor f_{n} (Equation 6) and f_{inc} to quantify the abundance profile of $X_{\text{mol}}(r)$ in Equation 5, in a trial-and-error manner to seek for better fits to the observational data. Figure F.2 demonstrates how the line ratios of CH_3OH K components vary with gas density and molecular abundance while keeping a fixed overall molecular column density, as an example using the density model of G08b.

Our best-fit model parameters for all the clumps are summarized in Table 7, column B. In these results, f_{r} ranges from 1.5 to 5 in all the sources except G31, indicating RADEX results only moderately overestimated the gas densities. As mentioned in Section 3.7, the rather large f_{r} in G31 is due to the very high optical depth of its lower CH_3OH K components in the central

region. In this case the CH_3OH (5-4) lines do not provide meaningful constraints for the RADEX modeling which was based on the assumption of moderate optical depth.

When spatially integrating Equation 6 with a spherical symmetric assumption, the resulting overall molecular gas masses (M_{mod}) considerably exceed those derived based on modeling dust continuum emission, by integrating ρ_{bulk} (see Appendix E). This implies that the dense gas structures traced by CH_3OH do not have spherically symmetric distributions. Instead, they are local gas concentrations that have small volume filling factors. To reconcile the mass difference, we defined $f_{\text{fdens}} \equiv M_{\text{enc}}/M_{\text{mod}}$, where M_{enc} designates the enclosed molecular gas mass within 0.5 pc radius (a scale encompassing the CH_3OH emission entirely for all sources) derived from the dust continuum models following ρ_{bulk} (Equation 2, Appendix E). f_{fdens} can be regarded roughly as an upper limit of volume filling factor of the dense gas traced by CH_3OH . From the radiative transfer modeling point of view, to fit the observed line profiles, in the optically thin limit, varying the dense gas volume does not affect line intensity ratios, while the values of $X_{\text{mol}}(r)$ can be adjusted accordingly such that the overall molecular column densities are not altered. We discuss the implications from the inferred *volume filling* factor of dense gas, and the dense gas mass fraction based on comparing ρ_{bulk} and ρ_{dense} in Section 4.5.

Appendix G: Comparison between observed spectra and modeling results: other targets

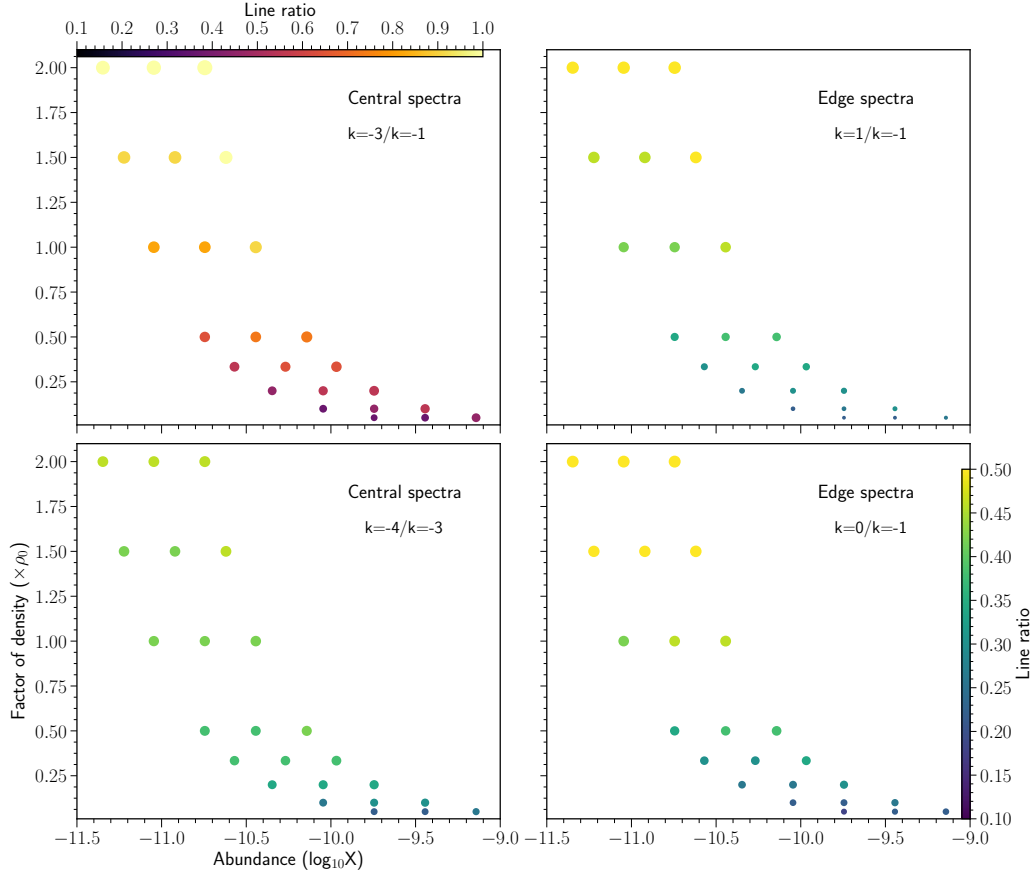


Fig. F.2. Line ratios of CH_3OH (5-4) K components from LIME models based on density profile of G08b (ρ_0 corresponds to the adjusted reference density at 0.1 pc for this source, as in Equation 6). Abundance value corresponds to the outer abundance (X_{out}) as in Table 7. The central marker at horizontal line of $y = 1$ corresponds to the best-fit model listed in Table 7 (column B). The comparison of observations with model spectra is presented in Figure 16, top panel.

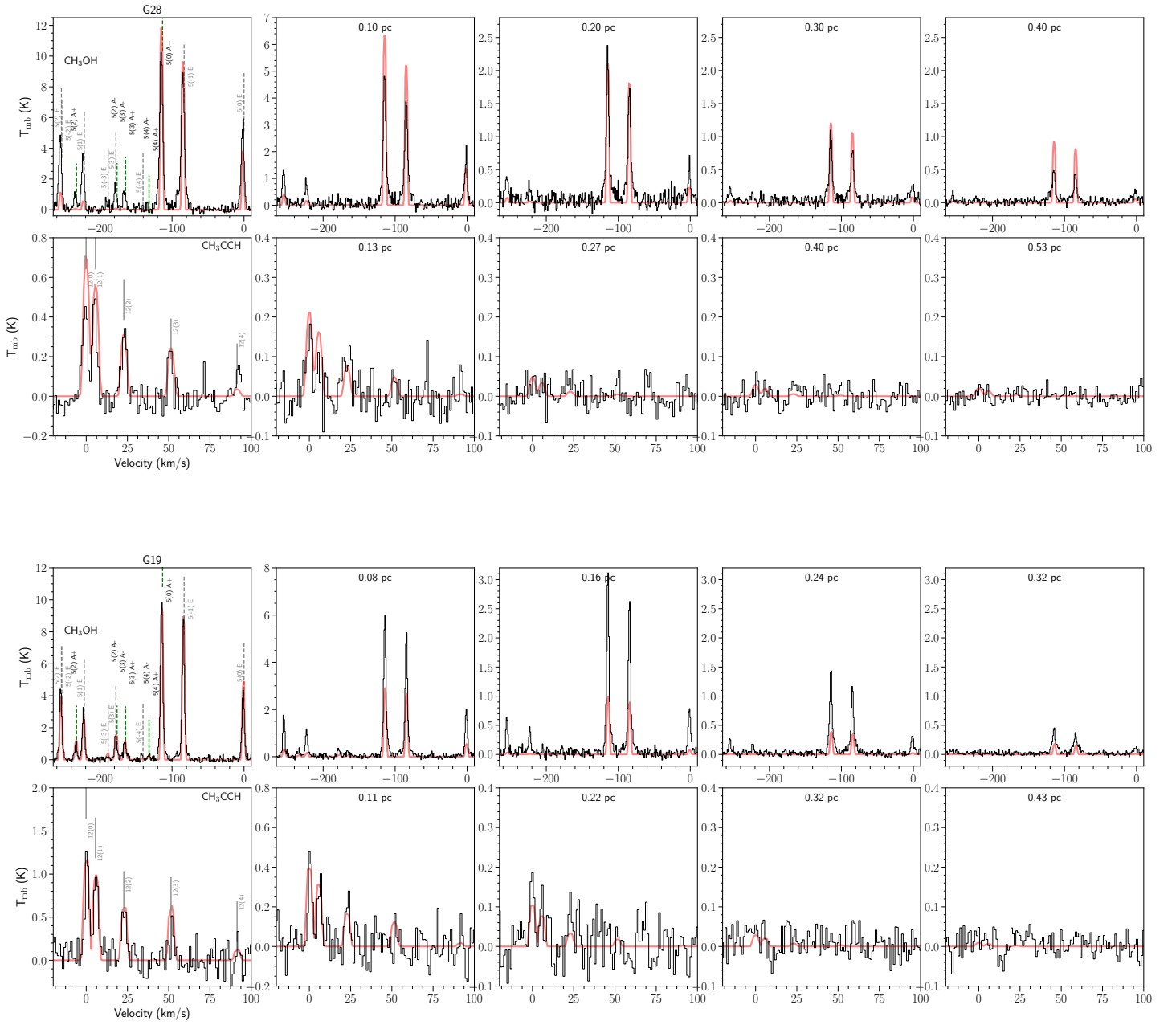


Fig. G.1. Same as Figure 15, for other target sources.

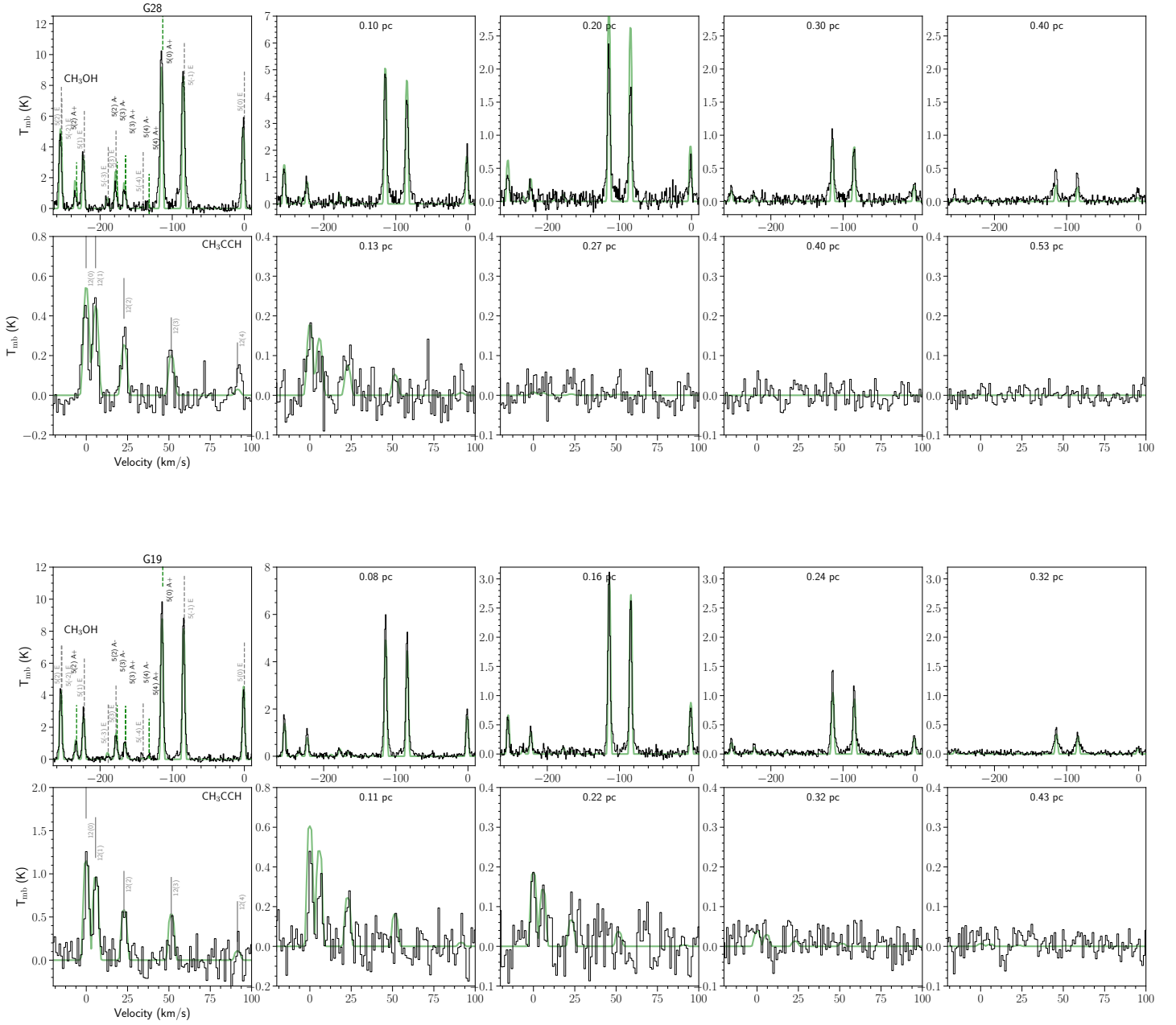


Fig. G.2. Same as Figure 16, for other target sources.

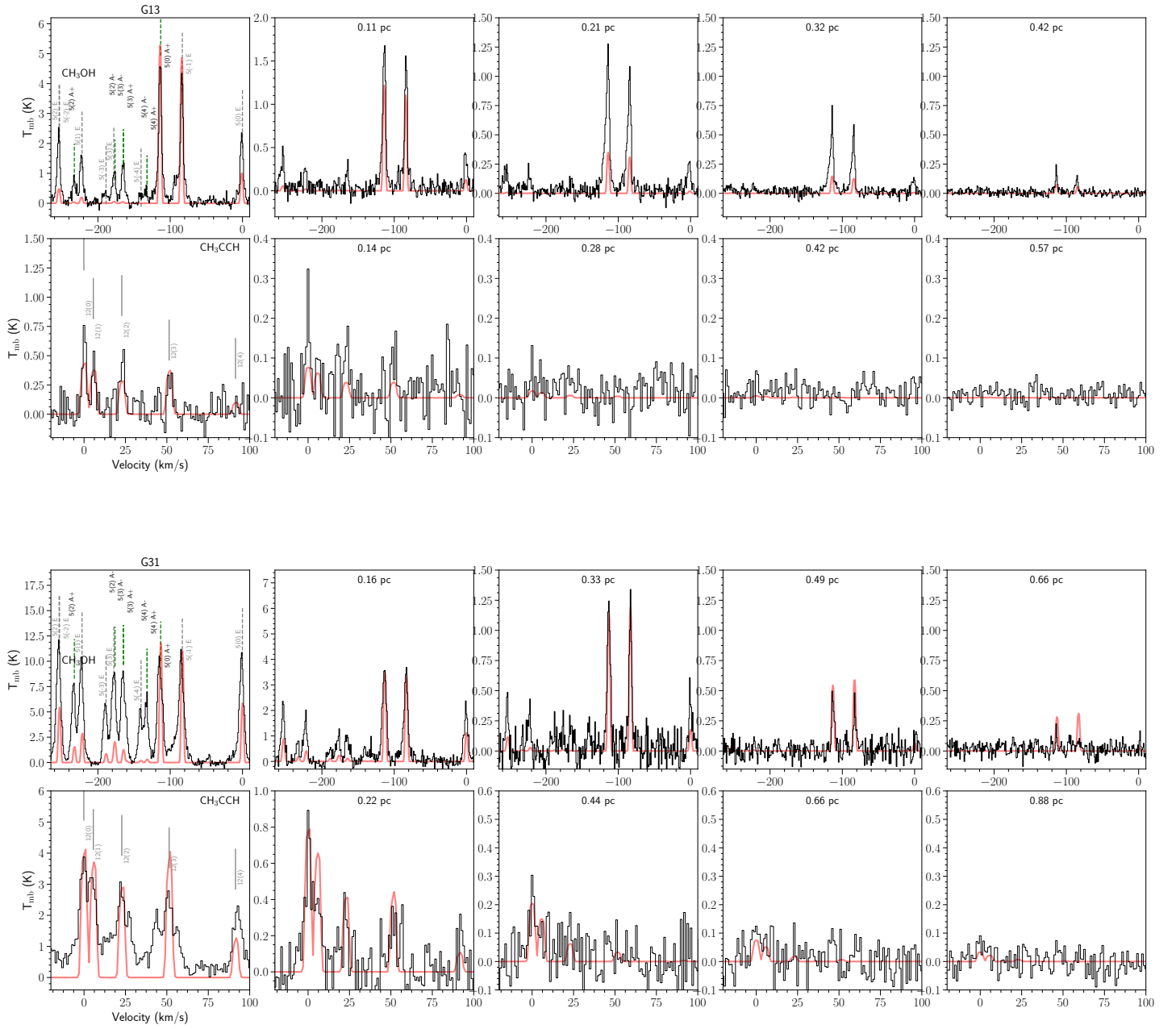


Fig. G.3. Same as Figure 15 , for other target sources.

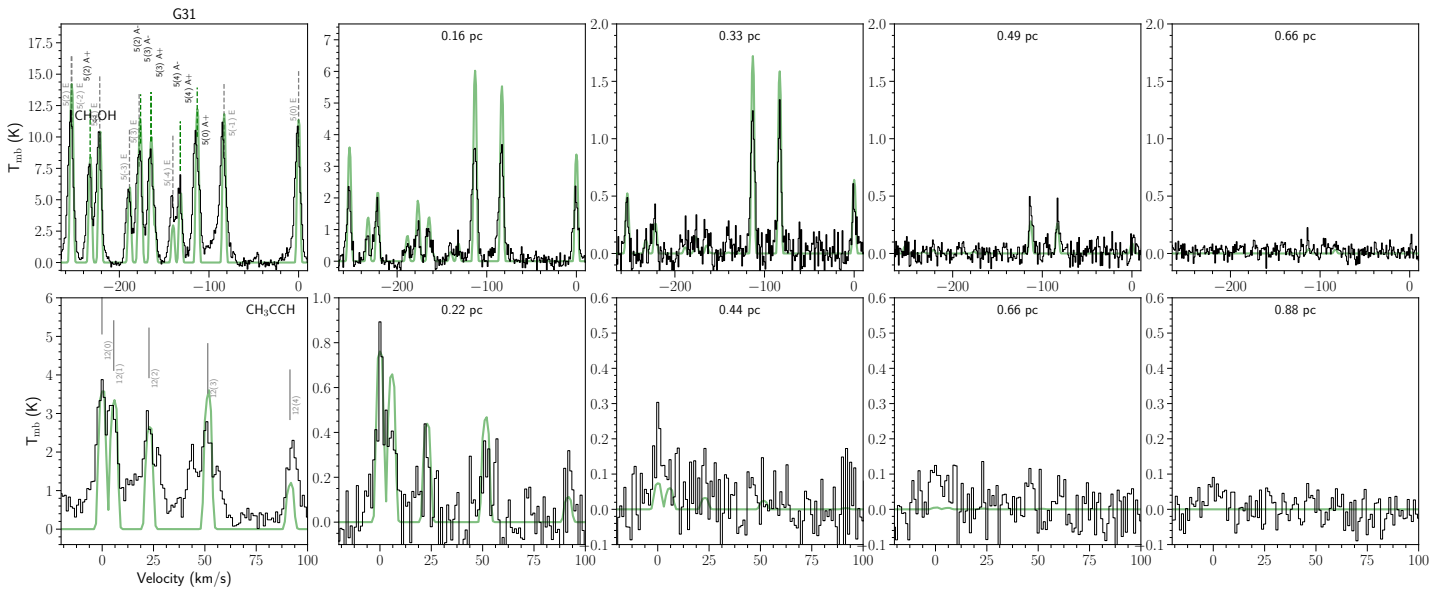
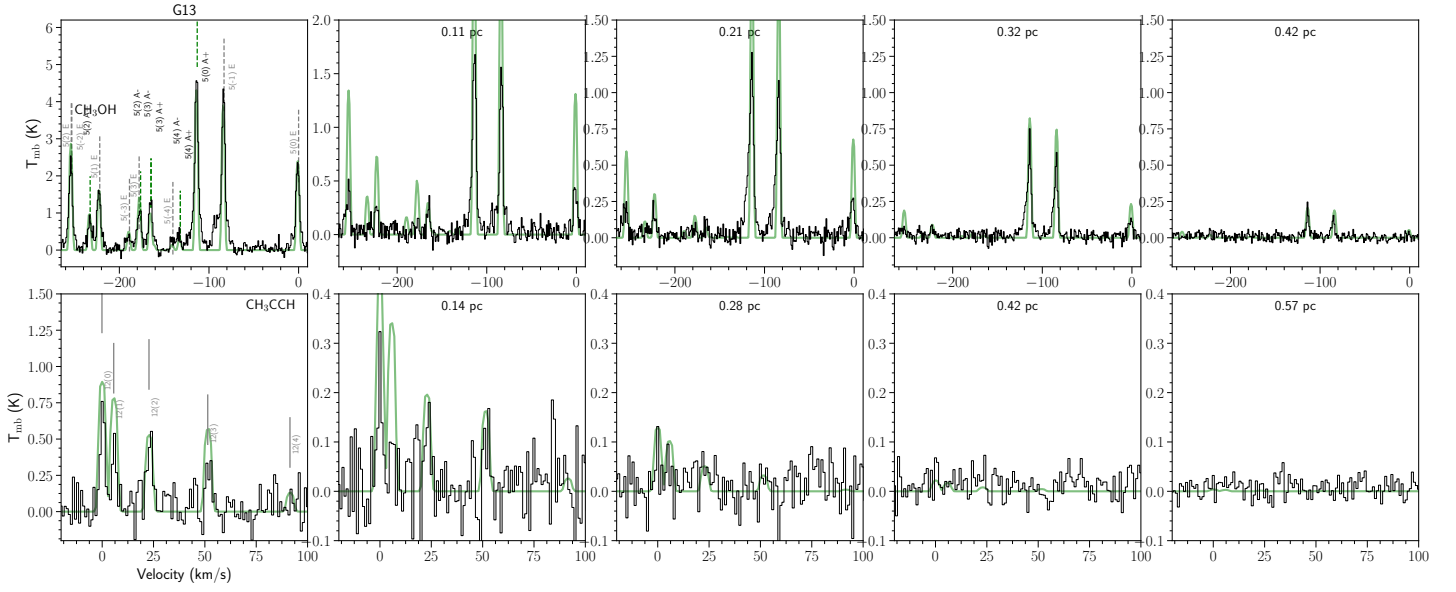


Fig. G.4. Same as Figure 16, for other target sources.

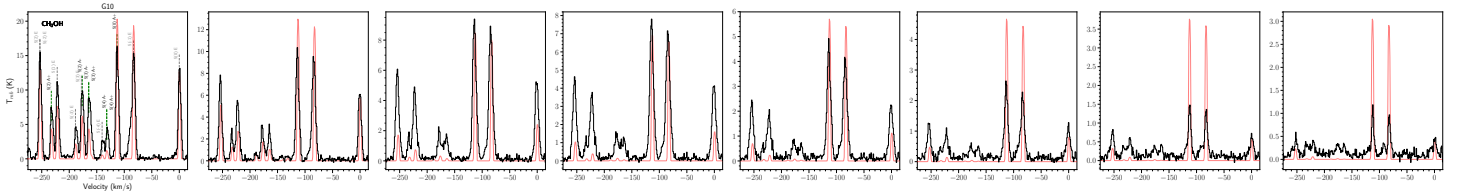


Fig. G.5. Same as Figure 15, for other target sources.

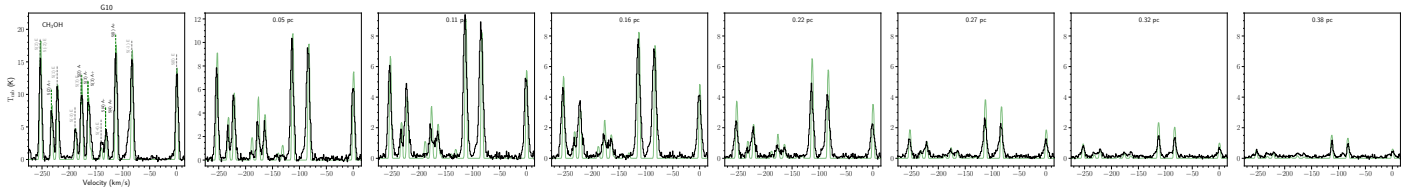


Fig. G.6. Same as Figure 16, for other target sources.

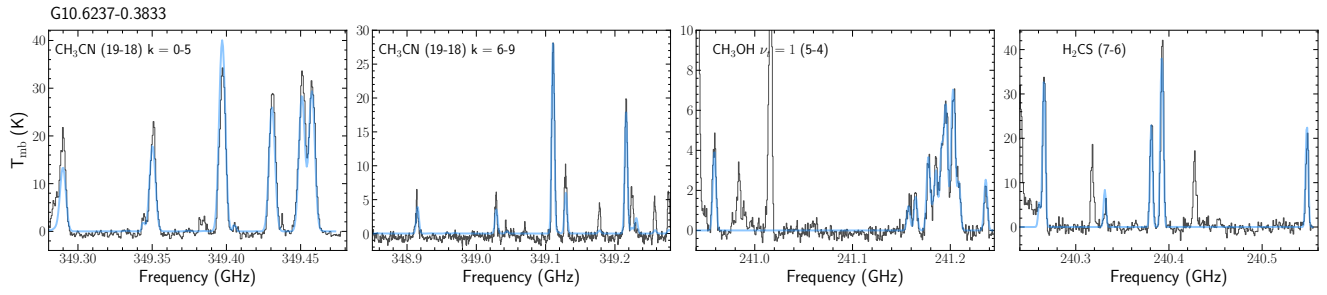


Fig. G.7. Example spectra (archival SMA data, Sect. 2) of thermometer lines and the XCLASS fits of G10.